UNIVERSITY OF CALIFORNIA, SAN DIEGO

Centrifugal Rheometry and Rapid Stimulation of Dinoflagellate Bioluminescence in a Microfluidic Device

A dissertation submitted in partial satisfaction of the requirements for the degree Doctor of Philosophy

in

Physics (Biophysics)

by

Edward E. Ronan

Committee in charge:

Professor Alex Groisman, Chair
Professor Elena Koslover
Professor Jeremie Palacci
Professor David Saintillan
Professor Sameer Shah

2018

The dissertation of Edward E. Ronan is approved, and it is acceptable in quality and form for publication on microfilm and electronically:

Chair

University of California, San Diego

2018

DEDICATION

This dissertation is dedicated to my mother, father, Jim and Breanne. Thank you for your constant love and support.

Cheers!

EPIGRAPH

"An experiment is a question which science poses to Nature,

and a measurement is the recording of Nature's answer."

-Max Planck

TABLE OF CONTENTS

LIST OF FIGURES

ACKNOWLEDGEMENTS

This dissertation is the culmination of years of work that would not have been possible without the help of others who I owe my thanks, and count myself lucky to have known.

First and foremost are my advisor, Alex Groisman, and Edgar Gutierrez. Alex has bestowed in me a deep appreciation for the elegance of experimental science. He is singularly clever and remarkably quick to digest new ideas and turn them to his ends. His critical eye and laser focus are responsible for sharpening and enhancing my work many times over. As for Edgar, I do not know if I owe him more gratitude for his endless patience or the wealth of information he's shared with me. Thank you for sharing your time and your friendship.

I'd also like to acknowledge the students I've shared my tenure in the Groisman lab with, Mike Erickstad, Mark Polinkovsky, Alex Yang, and Chih-Te Zee. I was very lucky to have Mike and Mark to show me the ropes. I would like to thank all of them not only for their help and friendship, but for all the interesting talks we've had over the years.

I am also lucky to have brilliant collaborators in Mike Latz, and Eva-Maria S. Collins. Thank you both for putting up with me and allowing me to share your vision.

Last, I would like to thank my family and my wife Breanne who I owe so much. Without you I would be adrift.

Chapter 2, in full, is in preparation for submission for publication as "Luminescence of Dinoflagellates upon Rapid Exposure to Shear Flow in a Microfluidic Device", Ronan, Edward; Latz, Michael; and Groisman, Alex. The dissertation author is first author and a leading contributor to this paper.

Chapter 3, in full, is in preparation for submission for publication as “A Novel Device for Measuring the Elastic Moduli of Soft Gels”, Ronan, Edward; and Groisman, Alex. The dissertation author is first author and a leading contributor to this paper.

Chapter 4.1, in full, is a reprint of the journal article “Rigidity of Silicone Substrates Controls Cell Spreading and Stem Cell Differentiation”, Scientific Reports, 2016. Vertelov, Grigory; Gutierrez, Edgar; Lee, Sin-Ae; Ronan, Edward; Groisman, Alex; Tkachenko, Eugene. The dissertation author is a co-author and a leading contributor to the substrate aspect of the experiment in this paper.

Chapter 4.2, in full, is a reprint of the supplementary information to the journal article “Rigidity of Silicone Substrates Controls Cell Spreading and Stem Cell Differentiation”, Scientific Reports, 2016. Vertelov, Grigory; Gutierrez, Edgar; Lee, Sin-Ae; Ronan, Edward; Groisman, Alex; Tkachenko, Eugene. The dissertation author is a co-author and a leading contributor to this work.

Chapter 5, in full, is a reprint of the journal article “Mechanics Dictate Where and How Freshwater Planarians Fission”, PNAS, 2017. Malinowski, Paul T.; Cochet-Escartin, Olivier; Kaj. Kelson J.; Ronan, Edward; Groisman, Alexander; Diamond, Patrick H.; Collins, Eva-Maria S. The dissertation author is a co-author and a leading contributor to the substrate aspect of the experiment in this paper.

VITA

2011	Bachelor of Science, Rutgers University
2011 - 2012	Graduate Teaching Assistant, Physics Department, University of California, San Diego
2012	Master of Science in Physics, University of California, San Diego
2012 - 2017	Graduate Research Assistant, Physics Department, University of California, San Diego
2015	Candidate of Philosophy in Physics, University of California, San Diego
2018	Doctor of Philosophy in Physics (Biophysics), University of California, San Diego

PUBLICATIONS

G. Vertelov, E. Gutierrez, S. Lee, E. Ronan, A. Groisman, and E. Tkachenko. "Rigidity of Silicone Substrates Controls Stem Cell Spreading and Stem Cell Differentiation". Scientific Reports, **6**, 33411 (2016).

P.T. Malinowski, O. Cochet-Escartin, K.J. Kaj, E. Ronan, A. Groisman, P.H. Diamond, and E.-M.S. Collins, Proc Natl Acad Sci USA **114**, 10888 (2017).

ABSTRACT OF THE DISSERTATION

Centrifugal Rheometry and Rapid Stimulation of Dinoflagellate Bioluminescence in a Microfluidic Device

by

Edward Ronan

Doctor of Philosophy in Physics (Biophysics)

University of California, San Diego, 2018

Professor Alex Groisman, Chair

The field of microfluidics has continued to grow steadily since its inception and proven indispensable in the exploration of micron scale phenomenon. It is particularly well suited to tasks where only a small volume of fluid is available or where high throughput is desired. Here

we present a simple microfluidic experiment allowing us to observe a large quantity of bioluminescent cells and observe their behavior on an individual basis.

Additionally, we present a novel device for measuring the elastic modulus of silicone gels and other transparent polymers. The device was created with the goal of characterizing the mechanical properties of environments used in biological experiments.

1. Introduction

Microfluidics is the study and manipulation of fluid flows through channels on the micron length scale[1]. At this scale fluids behave differently than the macroscopic length scale we observe every day. Fortunately, at small length scales fluid flow becomes laminar and well-ordered creating greater predictability and allowing us to not only understand and model the system more accurately, but also to manipulate the flow into a specifically chosen configuration. This capability makes microfluidics ideal for many experiments and has enabled a diverse range of projects including single cell studies[2], observation of chemical reactions with volumes of reagents on the nanoliter scale[3], and high throughput cell and particle sorting[4].

The microfluidic devices discussed here are relatively simple, but designed for specific measurements. In chapter 3 we will see a device used to corroborate a physical measurement of a gel, and in chapter 2 we will discuss a chip meant to expose a cell to a specific physical stimulus and allow for observation of its response. Using these devices in combination with various imaging techniques allows us insight into physical systems not otherwise possible.

In this chapter, I will discuss the essential physics necessary for understanding these microfluidic devices, the fabrication of the devices, and finally their operation and characterization. I will also give a brief introduction to the physics necessary for our discussion of the centrifuge rheometer presented in chapter 3.

1.1. Microfluidics

1.1.1. Flow in Microfluidic Channels

This section will loosely follow the derivations found in Henrik Bruus's Theoretical Microfluidics. The reader is referred to this book for additional detail on the equations and concepts presented here[5].

By making a couple assumptions we can greatly simplify our task of characterizing and modeling the flow in microfluidic devices. The first assumption is that the fluid we will be working with is Newtonian, and thus has a constant viscosity. The second assumption is that the fluid is incompressible. Essentially what this means is that the density of the fluid is a constant, and in practice this turns out to be a very good approximation. If we consider a small volume what this implies is that any fluid that leaves the volume is replaced by fluid entering the volume somewhere else. This can be expressed mathematically as

$$\vec{\nabla} \cdot \vec{v} = 0 \tag{1-1}$$

The Navier-Stokes equation for a Newtonian incompressible fluid is

$$\rho\left[\partial_t \vec{v} + \left(\vec{v} \cdot \vec{\nabla}\right)\vec{v}\right] = -\vec{\nabla}p + \eta\nabla^2\vec{v} \tag{1-2}$$

with $\vec{v} = \vec{v}(x, y, z, t)$ the fluid velocity vector field, ρ the fluid density, and η the dynamic viscosity of the fluid. The Navier-Stokes equation is not derived here, but comes from the forces experienced by the fluid and the conservation of momentum.

We can introduce a dimensionless constant known as the Reynolds number defined as

$$Re = \frac{\rho V_0 L_0}{\eta} \qquad 1\text{-}3$$

with V_0 a characteristic flow velocity (often average or maximum velocity) and L_0 a characteristic length scale in the flow (for instance the inner diameter of a pipe). The Reynolds number serves as a quick and simple indicator of the balance of inertial and viscous forces. In instances where $Re \ll 1$ we can say that viscous effects dominate, whereas when $Re \gg 1$ we say that inertial effects are most important. If we transform our coordinates to a dimensionless system(denoted by a tilde) we find that the Navier-Stokes equation becomes

$$Re\left[\tilde{\partial}_t \tilde{\vec{v}} + \left(\tilde{\vec{v}} \cdot \tilde{\vec{\nabla}}\right)\tilde{\vec{v}}\right] = -\tilde{\vec{\nabla}}\tilde{p} + \eta\tilde{\nabla}^2\tilde{\vec{v}} \qquad 1\text{-}4$$

In typical microfluidic experiments the Reynolds number is intentionally kept quite small (Re << 1,). Then the Navier-Stokes equation reduces to a linear differential equation that is much more tractable known as the Stokes equation

$$-\vec{\nabla}p + \eta\nabla^2\vec{v} = 0 \qquad 1\text{-}5$$

If we have a low Reynolds number and a Newtonian, incompressible fluid then we can calculate solutions for velocity fields in many typical microfluidic channels either analytically or by using computational methods.

Flow between infinite parallel plates

Often in microfluidics we will find ourselves using a thin but very wide channel. This is because the pressure driven flow through such a channel is very easy to model and understand when the side walls are far apart enough to be neglected. Indeed in the ideal case the side walls

would not exist at all, and this is the case we will solve next, that of pressure driven flow between infinite parallel plates.

Consider two plates a distance h apart in the z direction(at z=0 and z=h) with a known pressure $p + \Delta p$ at x=0 and p at x=L driving flow in the x direction. Looking at the Navier-Stokes equation(1-2) we can disregard both terms on the left hand side, they are both zero because nothing is changing in time and because the velocity is unidirectional. The gradient of the flow will be perpendicular to the flow itself and thus the dot product will be zero. This yields

$$\frac{\partial P}{\partial x} = \eta \, \partial_z^2 v_x(z) \tag{1-6}$$

The left hand side is the pressure drop per unit length which is simply $\frac{-\Delta p}{L}$. We can then solve what remains by direct integration using our no slip boundary conditions $v_x(0) = v_x(h) = 0$ to find

$$v_x(z) = \frac{\Delta p}{2\eta L}(h - z)z \tag{1-7}$$

This solution is a simple parabola. Knowing that the velocity must be zero at both walls allows us to exploit the symmetry of the situation to recognize that the maximum velocity must be found at $z = \frac{h}{2}$. Simply plugging in yields

$$v_{x,max} = \frac{h^2 \Delta p}{8\eta L} \tag{1-8}$$

We can also use our velocity formula to solve for the shear stress between the plates using the formula $\tau = \eta \frac{\partial v_x(z)}{\partial z}$ to find

$$\tau = \frac{\Delta p}{2L}(h - 2z) \tag{1-9}$$

We note this expression has a zero at $z = \frac{h}{2}$ and maximums at the walls, $z = 0, h$ which will be particularly relevant in chapter 2.

Additionally we can integrate our velocity distribution over a cross section of the channel with width w to find the total flow rate Q through that cross section such that

$$Q = \int_0^w dy \int_0^h dz \frac{\Delta p}{2\eta L}(h - z)z = \frac{h^3 w}{12\eta L}\Delta p \tag{1-10}$$

As Bruus notes[1] this differs from the real flow rate of a finite rectangular channel by 23% for an aspect ratio of one third ($h = \frac{w}{3}$) and by only 7% for an aspect ratio of one tenth ($h = \frac{w}{10}$). Finally we can compute the average flow velocity through the channel by dividing the flow rate by the cross sectional area to yield

$$v_{x,avg} = \frac{h^2}{12\eta L}\Delta p \tag{1-11}$$

It is a useful rule of thumb to keep in mind that for a rectangular channel with an infinite aspect ratio $v_{x,avg} = \frac{2}{3}v_{x,max}$.

1.1.2. Flow in Rectangular and Cylindrical Channels

We can move on from our idealized case to a real physical example by adding two walls in the y direction(let them be at $y = \pm\frac{w}{2}$ with $h < w$) so that our channel now has a finite cross

section. This small addition now complicates things quite a bit due to the new no-slip boundary conditions so that all together we now have

$$v_x(y,z) = 0 \text{ for } y = \pm\frac{w}{2}, z = 0, z = h \tag{1-12}$$

This also adds an additional dimension to consider in the Navier-Stokes equation such that our new task is to solve

$$\left[\partial_y^2 + \partial_z^2\right] v_x(y,z) = -\frac{\Delta p}{\eta L} \tag{1-13}$$

This is a bit tricky to solve but can be done by Fourier expansion in the z coordinate yielding a solution

$$v_x(y,z) = \frac{4h^2\Delta p}{\pi^3 \eta L} \sum_{n,odd}^{\infty} \frac{1}{n^3}\left[1 - \frac{\cosh\left(n\pi\frac{y}{h}\right)}{\cosh\left(n\pi\frac{w}{2h}\right)}\right] \sin\left(n\pi\frac{z}{h}\right) \tag{1-14}$$

Again we can integrate the velocity over the cross section of the channel to find the total flow rate and simplify the result in the limit $\frac{h}{w} \to 0$ to find

$$\mathrm{Q} \approx \frac{h^3 w \Delta p}{12\eta L}\left[1 - 0.630\frac{h}{w}\right] \tag{1-15}$$

This is a fairly good approximation even in the worst case of $h = w$ as Bruus notes[1] it is only off by 13% and when $h = \frac{w}{2}$ the error is already down to 0.2%. In practice microfluidic channels will often have aspect ratios much larger than two so this approximation is often well justified.

We can make an interesting analogy between microfluidic circuits and electrical circuits by noting that the flow rate is directly proportional to the pressure drop and noting that the pressure drop functions as a kind of potential difference. Whereas for electrical circuits we have

Ohm's law stating $V = IR$ for microfluidics we have $P = QR_{hyd}$. The hydrodynamic resistance is in this case

$$\mathrm{R}_{hyd} = \frac{\Delta p}{Q} = \frac{12\eta L}{h^3 w\alpha} \text{ with } \alpha = 1 - 0.630\frac{h}{w} \quad \text{1-16}$$

Using this analogy it is possible to simplify and solve many complex microfluidic problems by using familiar rules from electrical circuits such as the rules for adding resistors, Thevenin's theorem, and Kirchoff's circuit laws. It is also important to note that the hydrodynamic resistance scales as h^{-3} so a simple way to increase hydrodynamic resistance and decrease flow rate is to make the channel thinner. Additionally a less efficient way to increase resistance is simply by increasing the length of the channel, many microfluidic devices exhibit long serpentining channels for precisely this purpose.

1.1.3. Microfluidic Device Design and Fabrication

Microfluidic experiments are typically carried out in chips made of polydimethylsiloxane(PDMS) sealed against a glass cover slip. The experiment itself is carried out in the fluid flowing through the empty channels patterned in the PDMS. By designing the channels appropriately we can manipulate the fluid inside the chip to carry out the objective of the experiment. The channel reliefs are in the bottom of the chip such that the cover glass forms a fourth wall to the channel, and allows for easy observation from below, the ideal case for microscopes.

PDMS is an ideal material for fabricating microfluidic chips due to the fact it is biocompatible, gas permeable, translucent/transparent, fast curing, and minimally

autoflourescent. The optical properties of PDMS make the chips compatible with not only bright field microscopy but also fluorescence microscopy, the ability to use both in a single experiment is very advantageous. The gas permeability of the material also allows us to manipulate the gas content of certain channels by driving gas through adjacent channels.

The design process of a microfluidic device begins with a drawing in a vector graphics program such as AutoCAD, SolidWorks or Macromedia Freehand. Microfluidic chips are limited to features of certain heights(less than 1mm), and due to the fabrication process it is really only possible to have features of up to three different thicknesses. Each thickness constitutes a layer and each layer is cast in a separate process so that each must have its own drawing. Once the device design is finalized the photomasks are ordered from a photo plotting company for each layer of each design. The photomasks are transparent where the features of that layer will be and completely block all light elsewhere.

Fabrication begins by spin coating a silicon wafer with a UV-activated photoresist(we typically use SU8 made by MicroChem). Spin coating the wafer ensures a layer of uniform thickness across the wafer. The coated wafer is then baked on a hot plate and when it reaches the appropriate temperature is placed into contact with the photomask. By shining UV light through the photomask we activate the exposed photoresist causing it to harden creating the features we've designed at the thickness we've chosen. The wafer is then baked again to complete the cross-linking of the photoresist and finally washed in developer. The developer dissolves the unexposed regions of the photoresist leaving only the exposed areas above the wafer. This creates all the features of the first designated thickness and must be done again for features of each different thickness.

The resulting wafer is left with raised features with the heights and widths of the chip design. This constitutes a mold for the production of the actual chips which are cast in PDMS. The size of the wafer is such that typically many chips can fit on a single one and so many different designs may be present on each photomask. This allows for the production of many different types of chips at the same time, so long as the features share common thicknesses, and makes testing different designs relatively simple. Finally the wafer is treated with trichloromethylsilane vapor for five minutes so that the surface will not stick to PDMS.

Once the wafer is created it will serve as a master mold for the chips and the chip production will be relatively straight forward. Chips are created by mixing the two PDMS components, the base and the cross-linker in the desired proportion(typically 10:1 but different ratios can be used for different hardnesses) and pouring it over the wafer. The wafer is then degassed to remove bubbles and baked to allow the PDMS to cure. Once the PDMS solidifies it can be peeled from the wafer leaving a relief of the device design in the bottom of the PDMS.

Once the PDMS is detached it can be cut into separate chips. Holes for the inlets and outlets are then punched, and the chips are sealed against glass cover slips. Baking the device(~80˚C) on the cover slip bonds it strongly enough for typical pressures used in microfluidic experiments. This protocol will still leave the chip detachable from the glass cover slip so that it can be cleaned and reused, but a chip can be permanently bonded to a glass cover slip by plasma treating both surfaces and then baking if desired.

1.1.4. Standard Experimental Setup

Microfluidic chips always have at least one inlet and one outlet and potentially many more depending on the complexity of the experiment. To supply the incoming flow a fluid

reservoir is connected to each inlet port with flexible tubing, and likewise an outlet reservoir is connected to each outlet to collect the waste. The simplest way to generate a pressure gradient in the flow is typically with a hydrostatic pressure, just raising the reservoir supplying the flow above the level of the outlet is enough to drive flow. For ease of use typical reservoirs are attached to sliding tracks so that the height and therefore driving pressure can be easily adjusted. If hydrostatic pressure is not enough the reservoir will be sealed and driven with pressurized air. It is important to also keep the outlet reservoir above the level of the chip to create a positive pressure everywhere in the chip and prevent the formation of air bubbles.

One of the most important parameters in a microfluidic experiment will almost always be the rate that liquid flows through the chip. In order to know and manage the flow rate it is important to know the resistance of the chip and the tubing in use. Ideally the resistance of the tubing will be much smaller than the resistance in the chip so that it can be neglected, otherwise if the tubing needs to be modified it will affect the flow rate or if it needs to be replaced special care will need to be taken to ensure the same length of tubing is used and so the same resistance is created. Keeping the resistance in the experiment constant will allow the experimenter to simply modify the applied pressure to adjust the flow rate instead of having to track both pressure and resistance. To this end larger tubing is often used when possible for inlets and outlets and serpentine channels are sometimes included in the device design to increase the on chip resistance.

Lastly, in order to observe an experiment happening on the micron scale within the chip we use a microscope as part of our standard experimental setup. The use of a microscope allows us to magnify our view of the experiment easily by up to a factor of sixty and record what we observe with cameras. The choice of appropriate optics can have a significant impact on the

results of the experiment perhaps allowing for a wider field of view to collect more data, a sharper image for greater clarity, or a shorter time between recorded images reducing error.

Fluorescence microscopy is a particularly useful technique frequently used in our lab and generally in microfluidics. By labeling an object of interest in the experiment with a particular fluorophore we can create a reporter with a very clear signal. The technique works by exciting the fluorophore with a specific wavelength of light which then emits a higher wavelength of light. The way this works in practice is by using either an LED or a mercury lamp to provide the appropriate excitation wavelength. The light then passes through a filter cube, the first component of which is an excitation filter which blocks all light with wavelengths which are not very close to the excitation wavelength. After that the light hits a dichroic mirror oriented at forty-five degrees to the incoming light which deflects wavelengths less than the emission wavelength up into the objective to shine on the sample. The fluorophores in the sample are then excited by the incoming light, and emit light of the emission wavelength in all directions. The objective collects some of this light which then passes back down to the filter cube, encounters the dichroic mirror and passes through since the wavelength is now longer than what the dichroic reflects. After that the light passes through an emission filter limiting the collected light to a narrow band around the emission wavelength and ensuring our detector(camera or eyepiece) only sees the signal from the fluorophore.

1.2. Shear and Strain in Soft Gels

In addition to microfluidics my time in the Groisman lab has also been spent characterizing soft gels. In order to understand how the rheometer microscope presented in

chapter 3 functions it will be useful to see how soft gels respond to forces. We will begin by considering a rectangular prism of an elastic solid with length, L and cross sectional area A. If we stretch the block in the x direction with a force, F so that it now has length $L + \Delta x$ we can define the strain to be

$$\gamma_{xx} = \frac{\Delta x}{L} \tag{1-17}$$

Where the first subscript denotes the plane normal to the x direction and the second subscript denotes that plane is being displaced in the x direction. We can also define the axial normal stress to be

$$\sigma_{xx} = \frac{F}{A} \tag{1-18}$$

And we can relate the two with elastic modulus, E also known as the Young's modulus with the relation

$$\mathrm{E} = \frac{\sigma_{xx}}{\gamma_{xx}} \tag{1-19}$$

Most materials, and all the ones we will consider here will contract along their cross sections when subjected to a tensile normal strain. This can be quantified using Poisson's ratio,ν, which is 0.5 for rubber and all materials considered here and defined as

$$\nu = -\frac{\gamma_{yy}}{\gamma_{xx}} \tag{1-20}$$

Then assuming $\nu = 0.5$, if we pull the end of the sample enough to increase its length in the x direction by 1% so that $\Delta x = 0.01L$, its width will decrease in both the y and z directions by 0.5%.

1.3. Organization of the Dissertation

This dissertation is made up of the most significant projects I have contributed to as a graduate student. Each chapter is constituted of either previously published work, or work that is currently being prepared for submission for publication. The work is concentrated in two separate topics, using microfluidics to study dinoflagellate bioluminescence(Chapter 2), and the characterization and production of soft gels for use as experimental substrates (Chapters 3-5). In chapter 2 I present an experiment using microfluidics to induce high shear and stimulate the bioluminescent response of dinoflagellates. Chapter 3 will present a novel device for the characterization of soft gels (30Pa-200kPa). And finally, chapters 4 and 5 will illustrate the usefulness of the substrates that the work in chapter 3 enabled the production of.

Chapter 2 presents a microfluidic experiment meant to elucidate the importance of the cell wall in the mechanotransduction pathway of dinoflagellates. By using two treatments to disrupt parts of the cell wall we can infer their relative importance in the process of bioluminescence. To our knowledge this is the first time dinoflagellate bioluminescence has been measured in flow on the single cell level. Additionally, the experiment was designed to be high throughput so that thousands of cells are analyzed and counted using a custom made python program.

Chapter 3 describes a new device for measuring the elastic modulus of soft gels. It is significantly faster and cheaper than comparable methods and samples can be stored and easily re-measured should the need arise. The validity of the measurement technique is proven through comparison with both a microfluidic measurement and a mechanical stretching experiment. The device can also be used for dynamic measurements allowing for the estimation of relaxation times and probing of viscoelastic properties.

Chapter 4 presents work made possible by the centrifuge rheometer. By comparing human mesenchymal stem cells on substrates of various rigidities we were able to show that harder gels were more osteogenic, softer gels more adipogenic, and cell spreading areas correlated positively with the substrate rigidity. The ability to accurately characterize the elastic modulus of the substrates used was essential.

Chapter 5 again presents work enabled by the centrifuge rheometer. The planarian Dugesia japonica was studied to understand how it undergoes binary fission. We show that the process consists of three stages, a local constriction, pulsation, and then transverse rupture. The characterization of the substrate allowed us to measure the forces involved and create a mechanical model demonstrating that fission is a mechanical process and determined by physical constraints.

2. Luminescence of Dinoflagellates upon Rapid Exposure to Shear Flow in a Microfluidic Device

Abstract:

Bioluminescent dinoflagellates are unicellular protozoa that emit light upon mechanical stimulation. This bioluminescence is believed to serve the purpose of scaring away predators that generate mechanical stresses by their feeding currents, swimming, and handling of dinoflagellates. The exposure of dinoflagellates to these stresses usually occurs very rapidly, making it difficult to emulate in tabletop laboratory setups. Here we studied bioluminescence of *Lingulodinium polyedra* dinoflagellates after a rapid exposure to a shear flow in a microfluidic device. The dynamics of mechanical stimuli experienced by cells in the flow was explored using detailed numerical simulations. Experiments were performed in continuous flow, at shear rates comparable to those *Lingulodinium polyedra* experience in the ocean, with single-cell resolution and with large numbers of cells tested in each experiment. A specially built video-microscopy setup made it possible to measure the delay (latency) times between the exposure to shear and beginning of luminescence, to register all cells passing through the device, and to calculate the proportions of cells that luminesce. The proportions of luminescent cells and the latency times were compared between untreated cells and cells which were treated with latrunculin B and oryzalin that disrupted, respectively, the actin and microtubule components of their cytoskeletons.

Introduction:

Luminescent dinoflagellates are alveolate protists, ranging in size from <50 µm to ~1 mm, that emit blue-green light, when stimulated mechanically. This bioluminescence is generally believed to have an anti-predation function[1]. Bioluminescent flashes slow down and disrupt the feeding of the major predators of dinoflagellates[2–5] (e.g., copepods) and, by making the predators visible, can also attract secondary predators that pray on the predators of the dinoflagellates (burglar alarm effect)[6–10]. Mechanical stimuli produced by predators, such as copepods, may originate from their feeding currents, swimming, and the handling of dinoflagellates with feeding appendages[11–13]. Dinoflagellate luminescence is also triggered by large hydrodynamic stresses in flows around swimming mammals[14,15] and in ship wakes[16] and by breaking waves.[15] Luminescence of dinoflagellates produces spectacular displays of light at the shore, can be used to visualize hydrodynamic stresses in flows, and studying bioluminescence can help better understand the physiology of dinoflagellates and mechanosensing and mechanotransduction in cells and unicellular organisms.

The present understanding of the mechanism of bioluminescence of dinoflagellates is that mechanical stress makes the plasma membrane of the cell more fluid[17], activates GTP-binding proteins[18] and causes phospholipase C to activate transient receptor potential ion channels[19]. Ca^{2+} is released from intracellular stores[20], creating an action potential around the vacuole membrane[21], the tonoplast, that triggers a release of protons from the vacuole to the cytoplasm, decreasing cytoplasmic pH[22]. The lowered pH affects scintillons in the cell, which contain both luciferin and luciferase[23], activates the luficerase[24], and also releases luciferin from its binding protein[25]. Released luciferin then reacts with luciferase, producing bioluminescence. Because the cytoskeleton gives the cell its shape and resists deformation, it likely plays an important role in

mechanotransduction. F-actin and microtubules both act as a scaffold structure[26] that could communicate mechanosensitivity, while F-actin is also likely responsible for transporting the scintillons as they move through the cell between day and night phases.[27]

Among major quantitative parameters of the dinoflagellate luminescence are the total energy of flashes (the number of photons emitted) and their durations, the probability of a flash per unit time (or within a certain interval) at given conditions, and the delay time between the application of the stimulus and beginning of the flash (luminescence latency). These parameters are generally species- and strain-dependent and also depend on the type and strength of the stimulus and on the cell background and history, in terms of the culture conditions, time within the circadian cycle, and recent exposures to mechanical stimuli and recent luminescent flashes. Out of these major parameters, the energy and duration of individual flashes can be effectively measured in tabletop flow setups, such as the Couette flow (in the annular gap between two rotating cylinders)[13,28] and flow in a pipe[11,29,30], with the luminescent light registered along the entire track of the flashing cell using a properly calibrated photomultiplier (PMT).

Nevertheless, tabletop setups do not allow controlled rapid changes in the hydrodynamic stresses experienced by dinoflagellates. It is because the characteristic time of transition in a flow (after the rotation velocity of a Couette setups changes or the flow enters a pipe) is set by the viscous diffusion time, $t_{vd} = d^2 / \nu$, where $\nu = 1$ mm^2/s is the kinematic viscosity of water and d is the characteristic size (e.g., the width of the annular gap or diameter of the pipe). This time is 100 sec for $d =$ 10 mm and remains as large as 1 sec for $d =$ 1 mm. Therefore, tabletop flow setups cannot be used to measure the luminescence latency times that are typically <0.1 sec[21,31–33].

The proportions of dinoflagellates flashing within certain time intervals have been measured in tabletop setup for a range of wall shear stresses. Based on the experimental data, the threshold shear stress for triggering luminescence of *L. polyedra* dinoflagellates was estimated as ~0.3 Pa[11,29] for flows in a pipe and as 0.1 Pa for a Couette flow[13]. Nevertheless, those measurements were performed after dinoflagellates were exposed to near-constant shear stresses for extended times and, hence, were expected to become less sensitive to mechanical stimulation and less likely to flash. An obvious reason for desensitization after continued exposure to a mechanical stimulus is that luminescent flashes exhaust and deplete the reservoirs of luciferin. In particular, *L. polyedra* cells, being relatively small in size (35 μm diameter), are only capable to produce 2 – 4 consecutive luminescence flashes[11,33]. The desensitization of *L. polyedra* can also occur without apparent exhaustion. When in a Couette setup, the time of a linear ramp from zero to a final steady shear rate was extended from 1 to 8 sec (rate of the total luminescence was reduced by a factor of ~6 [12], suggesting that *L. polyedra* cells can suppress their luminescent responses by adapting to increasing hydrodynamic stresses within seconds.

The relatively short ramp time of 1 sec in the Couette flow experiments in Ref. [12], which was enabled by reducing d to 0.63 mm and the monitoring of luminescence during the entire transition, also resulted in a reduction of the estimated bioluminescence threshold to as little ~0.05 Pa, down from ~0.1 Pa and ~0.3 Pa reported before[13,29]. Importantly, hydrodynamic stresses in flows generated by common predators of *L. polyedra*, such as copepods and euphausiids, are believed to be low, at a level of 0.1 Pa (shear rate of 100 s^{-1}) or less[12,13]. On the other hand, because of the small size of the predators (~1 mm), these stresses are applied very rapidly, on time scales <0.1 sec (>1000 s^{-2} rate of change of shear rate)[12,13]. Therefore, the proportion of *L. polyedra* cells that luminescence in response to relatively small hydrodynamic

stresses, which are applied within ≤0.1 sec, is a question of direct ecological relevance. In particular, one can expect that the threshold stress required to trigger luminescence may significantly decrease, and for a given stress, the proportion of flashing cells may increase, if the stress is applied within ≤0.1 sec (as compared with 1 sec). Nevertheless, such short transition times are beyond the reach of tabletop flow setups. In addition, because in tabletop flow setups cell velocities tend to be high even at moderate hydrodynamic stresses, and because the imaging needs to be performed from relatively large distances, tabletop setups do not readily allow the tracking of all cells, especially when cells are as small as *L. polyedra* and do not flash.

Luminescence latencies of individual dinoflagellates were first measured by stimulating them electrically[21,31] and by pushing an immobilized dinoflagellate with an atomic force microscope (AFM) tip[32] and were usually found to be ~20 ms. Nevertheless, these types of stimuli are different from what dinoflagellates experience in their native environment in the ocean. Luminescence latency of *L. polyedra* was measured at as short as 12 ms in a microfluidic device, where cells moving with flow in an ~200 μm deep channel were brought to a barrier with a ~15 μm clearance that resulted in a >50-fold increase in the mechanical stimulus within ~2.5 ms. At the barrier, cells were exposed to counteracting forces: the hydrodynamic drag applied to the entire cell surface and the reaction (and friction) forces applied to small areas of contact of the cells with the barrier and the channel bottom. Therefore, the stimulus in these experiments was also different from mechanical stimuli in the ocean. Moreover, the forces applied to cells were in a range of 40 – 400 nN[33]. *L. polyedra* cells would experience forces in this range in flows with shear stresses of 16 – 160 Pa (shear rates of $1.6 \cdot 10^4$ - $1.6 \cdot 10^5$ s^{-1}; see Discussion), which are substantially greater than stresses typically found in oceanic flows and orders of magnitude greater than stresses produced by the common predators of *L. polyedra*[12,13]. It is not

clear, to what extent the findings of these microfluidic experiments on either the luminescence latency and proportions of flashing cells would apply to oceanic flows and anti-predation behavior of *L. polyedra*.

The threshold hydrodynamic stress and the proportion of cells flashing within a short time after a rapid exposure to a given moderate hydrodynamic stress (and the dependence of the proportion on the stress) as well as the luminescence latencies at moderate hydrodynamic stresses are all either unknown or not known precisely for *L. polyedra* (and other dinoflagellates). It is also unknown, how the weakening or disruption of microtubule and F-actin components of cytoskeleton would affect bioluminescence of dinoflagellates.

Here we developed and applied an experimental setup based on a hybrid luminescence-darkfield video-microscopy system and on a microfluidic device operating in a continuous flow regime, in which *L. polyedra* dinoflagellates are exposed to an ~10-fold increase in the hydrodynamic stress within an ~20 ms time interval. We observed the dynamics of luminescence of individual *L. polyedra* cells after the rapid increase in the stress, which was nearly pure shear, with ~5 ms resolution, while being able to account for every cell, whether it was luminescent or not. The continuous operation of the setup lead to a high throughput, making it possible to test three populations of ~1000 individual cell in each experiment. The experiments were supported by detailed numerical simulations that provided data on the dynamics of mechanical stimuli experiences by cells moving along different flow pathlines. We used the setup in a series of experiments on *L. polyedra* dinoflagellates treated with latrunculin B and oryzalin, disrupting, respectively, the F-actin and microtubule components of their cytoskeletons, and on untreated controls. The experimental results provided data on the luminescence latencies and proportions

of cells that flash immediately after a rapid exposure to a moderate hydrodynamic stress for untreated *L. polyedra* cells and for cells with weakened cytoskeleton.

Materials and Methods:

Microfluidic device and flow setup

The microfluidic device is made of an ~6 mm thick monolith PDMS chip sealed against a #1.5 microscope cover glass. The device has a single microfabricated horizontal channel with a depth h = 112 µm, width w = 2 mm, and a length L = 8.5 mm, and a vertical capillary with a diameter $d_1 \approx 1.0$ mm, which is connected to the horizontal channel near the middle and is made by punching a hole in the PDMS chip with gauge 15 sharpened luer stub (Fig. 2-1). The device has a single outlet and two inlets, inlet 1, to feed seawater to the upstream end of the horizontal channel, and inlet 2, to feed a suspension of dinoflagellates in seawater to the top of the vertical capillary. The outlet at the downstream end of the horizontal channel is connected through a 1.6 mm inner diameter (ID), low-resistance tubing line to an open reservoir of seawater, setting a stable outlet pressure, which is nearly independent of the flow rates through the inlets 1 and 2. Because of the large diameter of the outlet reservoir (50 mm) the outlet pressure also remains practically unchanged in the course of an experiment (a change of about ~6 Pa over 1 hr), while the volume of liquid in the outlet reservoir steadily increases.

The flow-driving setup and microfluidic device are designed to meet four main goals: (1) rapidly expose dinoflagellates to a sufficiently high shear stress to trigger their luminescence in an area where the luminescence can be readily observed; (2) ensure that the level of the high shear rate is uniform over the population of dinoflagellates; (3) prevent any premature exposure of dinoflagellates to mechanical stresses that may be strong enough to trigger their luminescence;

(4) keep dinoflagellates generally healthy and luminescence-capable in the course of 2-3 hour long experiments. To meet the first goal, dinoflagellate suspension was fed to the relatively shallow horizontal channel, where the volumetric flow rate was $Q_3 \approx 3.3$ μL/sec and the maximal shear rate (near the ceiling, downstream from the vertical capillary) had a high level of $\gamma = 6Q_3/(h^2 w) \approx 800\ \mathrm{s}^{-1}$, corresponding to a shear stress of 0.8 Pa, given the viscosity of water η = 0.001 Pa. (The value of Q_3 was measured by collecting the seawater coming out of the device outlet for 30 minutes and weighing the collected seawater). This shear rate was well above the luminescence threshold of 50 - 100 s^{-1} reported for *L. polyedra* in experiments in macroscopic flows.[12] To make the exposure to the high shear rate rapid (to be able to observe the latency between the exposure to the high shear and beginning of luminescence), dinoflagellates enter the horizontal channel directly from the wide vertical capillary, where the shear rate is very low (see below). As a result, the transition from the low-shear zone to the high-shear zone occurs over a distance of <100 μm (and over a time of only ~10 ms in the Lagrangian reference from of moving fluid; see below).

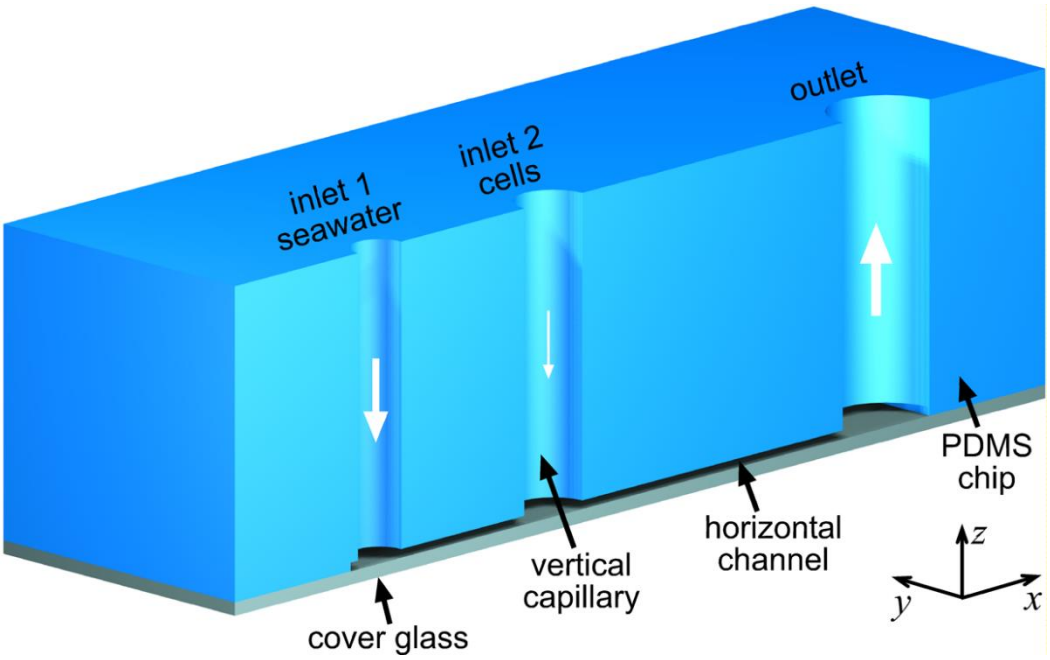

Figure 2-1: Schematic drawing of the microfluidic device.
A cross-section in the vertical (xz) plane of symmetry is shown. White arrows show the direction of flow. Horizontal channel is 112 µm deep and 2 mm wide, and vertical capillary is 1 mm in diameter. Flow in the horizontal channel is along the positive x-direction. Bioluminescence is observed in the horizontal channel to the right of the downstream edge of the vertical capillary.

To meet the second goal, the volumetric flow rate of the dinoflagellate suspension, Q_2, is made small as compared with the total flow rate in the horizontal channel, $Q_2 \approx$ 0.54 µL/s *vs.* $Q_3 \approx 3.3$ µL/sec. As a result, dinoflagellates entering the horizontal channel are hydrodynamically focused to a relatively thin layer near the ceiling, where the shear rate is relatively uniform. (Because of the parabolic profile of the flow, the shear rate decreases from the maximum of 800 s^{-1} at the ceiling to zero at the midplane of the horizontal channel.) The high volumetric flow rate in the horizontal channel was due to seawater fed to inlet 1 at a volumetric rate flow rate $Q_1 \approx$ 2.8 µL/s ($Q_3 = Q_1 + Q_2$). The reservoir with seawater was pressurized at P_1 = 1.5 kPa (using compressed air) and connected to inlet 1 through a 80 cm long tubing line with an internal diameter (ID) of 500 µm that served as a fluidic resistor.

To meet the third goal, the flow setup is built in such a fashion that on their way from the reservoir, where they are held, to the horizontal channel, where they are exposed to the high shear rate, dinoflagellates encounter shear rates that are well below the luminescence threshold. To this end, the reservoir is connected to inlet 2 of the device through a tubing line with a relatively large ID, d_2 = 0.76 mm. The maximal shear rate in this tubing line is $\gamma_2 = 32Q_2/(\pi d_2^3) \approx 13\ \mathrm{s}^{-1}$, well below the luminescence threshold for *L. polyedra*. The maximal shear rate in the vertical capillary is at an even lower level of $\gamma_1 = 32Q/(\pi d_1^3) = 5.5\ \mathrm{s}^{-1}$ because of the larger ID. To keep the setup simple and easy to operate, while avoiding fluctuations of the flow rate, the flow of dinoflagellate suspension was driven by differential pressure (rather than volumetrically using a syringe pump), with the flow rate set with fluidic resistance. However, the necessity to prevent the premature exposure of dinoflagellates to high shear rates made it impractical to place a sufficiently large fluidic resistor between the reservoir and the horizontal channel. Therefore, the fluidic resistor, a 3mm long segment of PEEK capillary with ID = 62.5 μm, was placed upstream of the reservoir with dinoflagellates, which was a watertight cuvette completely filled with the dinoflagellate suspension. The upstream end of the capillary was connected to a reservoir with seawater, which was pressurized at P_2 = 6.5 kPa using compressed air. (The shear rate inside the capillary was ~$2.3 \cdot 10^4$ s^{-1}.) The relatively high driving pressure (6.5 kPa *vs*. 1.5 kPa for seawater fed to inlet 1) facilitated the flow control and, together with the relatively high fluidic resistance of PEEK capillary (as compared with the resistance of the horizontal channel of the microfluidic device), made it possible to adjust the flow rate of the dinoflagellate suspension, Q_2, independently of the flow rate of through inlet 1. (The flow rate Q_2 was measured by collecting the liquid coming out of the cuvette over 30 minutes and weighing it).

Our early experiments indicated that to maintain dinoflagellates healthy and luminescence-capable in the relatively high-concentration suspension fed to the microfluidic device, it was essential to keep the suspension well-aerated, while avoiding its stirring (which would generate hydrodynamic stresses potentially triggering pre-mature luminescence). To this end, the watertight cuvette for dinoflagellate suspensions had air-permeable ceiling and sidewalls and a relatively small square cross-section of 8x8 mm. The cuvette was ~12 cm long and had a volume of 7.7 mL. Its sidewalls were cast of air-permeable silicone elastomer (Sylgard 184) using a specially made plastic mold (laser-cut from acrylic) and bonded to the solid acrylic bottom of the cuvette. The roof of the cuvette was a laser-cut piece of 0.06" thick acrylic with an array of 4x4mm square windows in it and a 0.01" thick sheet of silicone (HT-6240 by Rogers-Bisco, Carol Stream, IL, USA) attached to the bottom side of the acrylic. After the cuvette was filled with a dinoflagellate suspension, the roof was sealed against the flat top of the sidewalls using screws and nuts. The layer of flexible silicone served as a gasket and made the roof highly air-permeable, thus facilitating the aeration of the dinoflagellate suspension in the cuvette. Because the oxygen permeability of silicone is as much as 6 times greater than that of water, for the purposes of oxygen access, covering the roof windows with silicone was nearly equivalent to leaving them open. On the other hand, because of the relatively small diameter of the windows, the roof had relatively low deformability, even given the small thickness and low elastic modulus of the silicone layer. Therefore, a steady flow through the cuvette was rapidly established after the upstream seawater reservoir was pressurized. The total volumetric flow through the cuvette (at 0.56 µL/sec) during an ~ 1 hr experimental run was only ~2 mL. Therefore, the influx of seawater from the upstream end of the cuvette caused very small reduction of concentration of dinoflagellates in the suspension fed to the device from the downstream end of the cuvette.

Optical setup and image processing

The optical setup was designed to register all dinoflagellate cells entering the horizontal channel of the device, whether luminescent or not, efficiently collect the luminescent light, and reliably detect the positions, where individual dinoflagellates start and end luminescing. The goals were to compute the proportion of luminescent cells and also, using the data on flow velocity in the horizontal channel, to evaluate the duration of luminescent flashes and the latency between the first exposure to large hydrodynamic stress and the beginning of luminescence. The microfluidic device was placed on a stage of an inverted microscope (Zeiss Axiovert 135), and the imaging was done with a 4x/0.2 objective, providing a combination of a relatively high light-collecting power (NA = 0.2) and a large field of view (because of the relatively low magnification). The relatively faint luminescent light was collected with a sensitive EMCCD camera (Roper Scientific Cascade:512B) using a 0.42x (reducing) video coupler. The resulting field of view was 4.9x4.9 mm and covered the entire width of the horizontal channel and a 4.9 mm long region just downstream of the junction between the vertical capillary and the horizontal channel. Given the mean velocity of dinoflagellate cells of ~16 mm/sec (see below), this optical setup enabled the detection of luminescence as late as ~300 ms after the first exposure of cells to large hydrodynamic stress.

To register all cells entering the horizontal channel of the device, a region downstream of the junction with the vertical capillary was illuminated by a focused low-intensity beam of a 650 nm solid state laser, which was directed at an oblique angle and did not directly enter the microscope objective. When a dinoflagellate cell (or some other light-scattering object) passed through the region illuminated by the beam, the laser light scattered by the cell was collected by the objective, making the cell appear bright on a relatively dark background. (This setup was an

implementation of dark-field microscopy, but the background was not completely dark because of scattering of light at various interfaces.) Light collected by the objective (from dinoflagellate luminescence and laser light scattering) was split at an 80/20 ratio, with 80% directed towards the EMCCD camera and 20% directed towards a lower-sensitivity CCD camera (a regular digital 2/3" CCD, Basler 102F). This CCD camera was also equipped with a 0.42x reducing video coupler and had a field of view covering the entire width of the horizontal channel and an ~5.3 mm long segment along the channel. The EMCCD camera light path had a laser light rejection filter. Therefore, this camera was only exposed to relatively faint luminescent light emitted by dinoflagellates and only detected cells that flashed, whereas the CCD camera captured much brighter scattered laser light and registered all cells passing through the horizontal channel.

Images were acquired simultaneously with the two cameras using two computers with manual synchronization. Images were recorded in consecutive 37.5 sec long runs, with continuous flow during the entire time of the experiment. The CCD camera took 12.8 frames/sec with 78 ms exposure time and the EMCCD camera was operated at 40 frames/sec with a 25 ms exposure time. The passage of a dinoflagellate cell through the horizontal channel generated an image of a streak line on the CCD camera and, if the cell flashed, also a shorter streak on the EMCCD camera. To identify cell streak lines in images from the CCD camera (scattered laser light), the images were analyzed using a homemade Python script. For each run, a background image with no cells present was selected and subtracted from all images. Images were then thresholded and converted to binary, and an image opening was performed with a 7x7 square kernel. For each 7x7 square of pixels, if any pixel in the square was off (black), the center pixel was turned off, thus removing all stray background. Following that, the image was dilated with the same kernel so that the center pixel was turned on if any pixel in the rectangle was on. This

procedure removed nearly the entire stray background, producing clearly identifiable streak lines. Finally, streak lines were identified using a Hough transform, and images with cell streak lines were marked and saved. The streak lines were counted to obtain the number of cells passing through the channel. The length of the streak lines was measured and divided by the exposure time (78 ms) to obtain velocities of the cells.

Streak lines produced by luminescence flashes and recorded with the EMCCD camera were identified, counted, and analyzed manually, without automated image processing, because of much lower signal to background ratio. Specifically, the position where the luminescence first became clearly detectable was identified, and the distance along the flow direction between this position and the downstream edge of the vertical capillary, Δx, was measured and divided by the mean velocity of cells in the flow , $\bar{v}$, to obtain the delay in luminescence past the passage of the edge, $t_{ed} = \Delta x / \bar{v}$. The capillary edge set a clear fiduciary mark and also was a position, where according to our numerical simulations (see below), the mechanical stimulus experienced by cells in the flow reached a maximum. Because of limitations of the setup, the luminescence was only reliably detectable starting from distances $\Delta x > \Delta x_1 = 120$ μm, corresponding to a time $\Delta t_1 = \Delta x_1 / \bar{v}$ in the frame of a moving cell. In addition, according to our numerical simulations (see below), cells were expected to experience mechanical stimuli of magnitudes potentially capable of triggering luminescence during a time Δt_0 prior to reaching the downstream edge of the vertical capillary. As a result, the setup did not allow to reliably measure latency times shorter than $\Delta t_0 + \Delta t_1$.

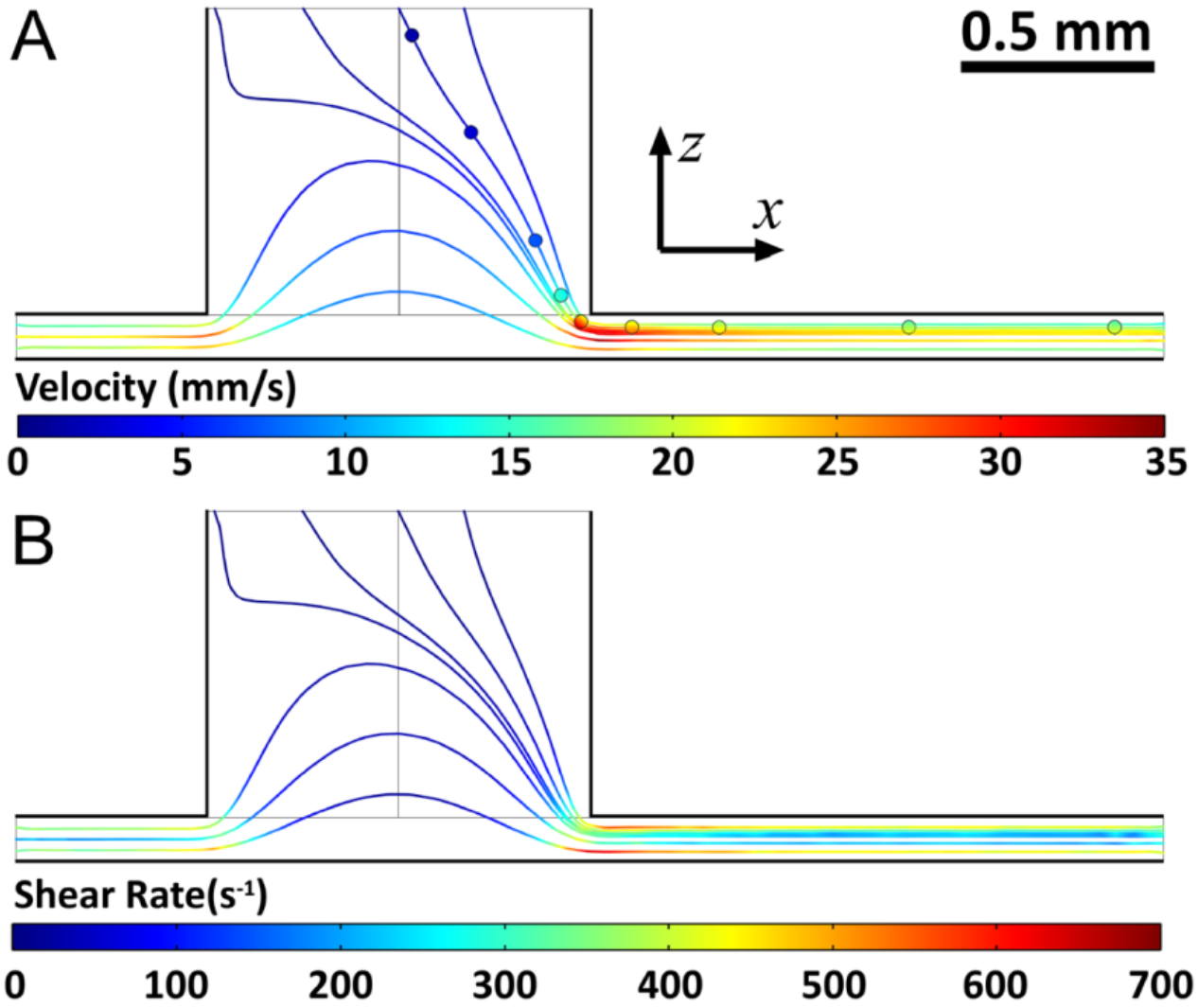

Figure 2-2: Results of numerical simulations of the flow in the microfluidic device with Comsol.
The computational domain is one half of a 3 mm long fragment of the horizontal channel with one half of a 1 mm tall segment of the vertical capillary connected to the channel and had the downstream corner of the vertical channel near the middle. The division into two halves is by the vertical plane of symmetry of the device (xz-plane), which is a vertical boundary of the computational domain. Both panels show flow lines in the plane of symmetry for a simulation with no cells. The flow-lines are color-coded with (A) flow velocity and (B) shear rate. Circles in panel A represent a cell, which is color-coded for its velocity and moves along the flow pathline initiating at the axis of symmetry of the vertical capillary.

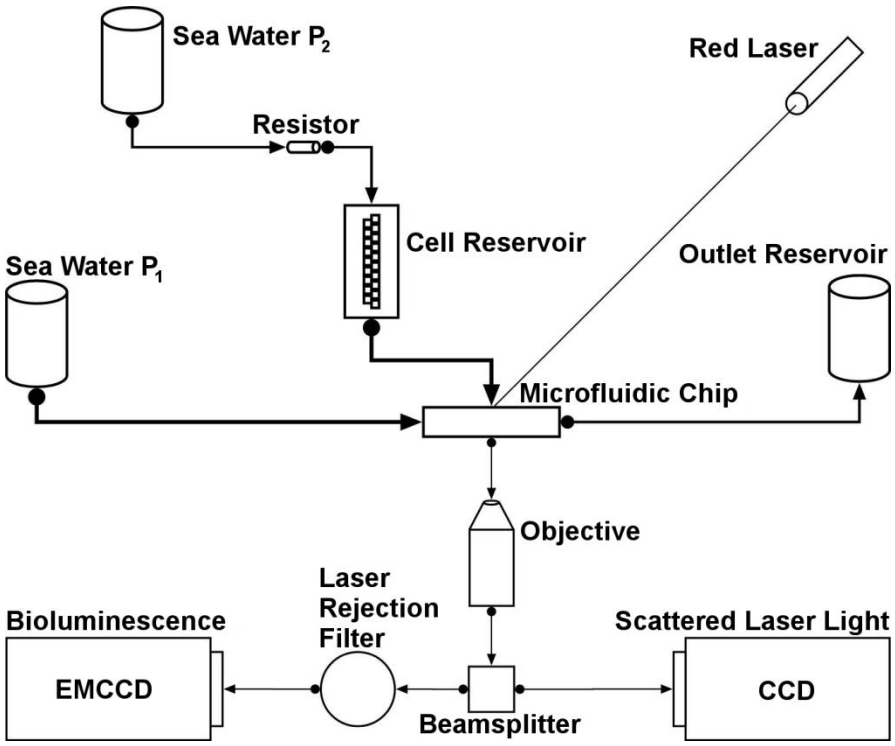

Figure 2-3: Diagram of the experimental setup.
A suspension of dinoflagellates is held in a specially built horizontal cuvette (cell reservoir) and its flow towards the device is driven by pressurizing a seawater reservoir upstream of the cuvette and inserting a fluidic resistor between the two. Cells in the horizontal channel of the device are illuminated with a red laser beam at an oblique angle, and the laser light scattered by dinoflagellates is collected by the objective. The objective also collects the bioluminescent light emitted by cells and creates the image of the horizontal channel with cells. The collected light is split 80/20 between a high-sensitivity EMCCD camera and a regular CCD camera. A red laser light rejection filter in the EMCCD camera channel ensures that this camera only registers the luminescent light, whereas the CCD camera registers the much brighter scattered laser light.

Numerical simulations

We performed numerical simulations in Comsol to better understand the dynamics of stresses and forces experienced by a dinoflagellate cell, as it moves from the vertical capillary to the horizontal channel, entering a region with greatly increased hydrodynamic stresses. To simplify the computations, we took advantage of the symmetry of the device with respect to the vertical plane, which is parallel to the centerline of the channel and divides the device into two mirror-symmetric halves. The computational domain was a fragment of a half of the device and

included a rectangular prism with *xyz*-dimensions L = 3000 μm, w = 1000 μm, and h = 112 μm, respectively, representing a fragment of the channel, and a 800 μm tall, 1 mm diameter half-cylinder, representing a fragment of the vertical capillary (Fig. 2-2). The boundary conditions were symmetry (slip) at the symmetry (*xz*) plane, volumetric flow of 1.76 μL/s to the right from the left (negative *x*) boundary, volumetric flow of 0.27 μL/s to the bottom from the top (*xy*-plane) boundary, an outlet at the right (positive *x*) boundary, and solid walls otherwise. The seawater was modeled by a fluid with dynamic viscosity η = 0.001 Pa·s and density ρ = 1,024 kgm^{-3}. In simulations of a dinoflagellate cell (which was always assumed to move along the plane of symmetry), the cell was represented by a D = 35 μm diameter hemispherical subdomain of liquid with a density[34] of 1.084 g/cm^3 and a viscosity of 10 Pa·s. Because the viscosity of the hemisphere domain was 10^4 greater than that of water, the rate of strain inside the hemisphere was practically zero. Therefore, the motion of the hemisphere was a sum of translation and solid rotation, making it practically indistinguishable from the motion of a solid hemisphere of the same diameter (a half of a hard-walled dinoflagellate). Additionally, this hemisphere was surrounded by an explicitly defined 0.5 μm thick hemispherical shell that resulted in an automatic generation of a higher-density mesh around the D = 35 μm hemisphere, improving the consistency and precision of computation of hydrodynamic stresses at the hemisphere surface. The maximal flow velocity in the horizontal channel was v_{max} = 23.2 mm/s that corresponded to a Reynolds number, $Re = \rho v_{max} h / \eta \approx 3$, suggesting a near-linear flow regime and laminar flow.

Whereas we did not directly simulate the complete dynamics of motion of cells (hemispheres) through the computational domain, we used the numerical simulations to obtain several useful types of data. First, we simulated the flow pattern without cells and obtained continuous streamlines leading from the vertical capillary to the channel. Those streamlines

provided information on the distribution of cells over the *yz*-cross-section of the horizontal channel downstream of the capillary (neglecting inertial effects and perturbations to the flow introduced by the moving solid cells). Second, by placing a hemisphere at a certain position in the plane of symmetry, we obtained its velocity, v, and distribution of mechanical stresses over the surface of the hemisphere at this position. Third, by moving the hemisphere between a sequence of positions along a streamline, calculating the surface stress distribution at each position, and computing the incremental time, Δt, it takes the hemisphere to move between these positions, we obtained the surface stress distribution as a function of time, t, in the Lagrangian reference frame of the hemisphere moving in the flow. The values of Δt were obtained by taking the velocity, *v*, and displacement, *s*, along the streamline from the flow simulation without the hemisphere (cell) and numerically calculating the integral $\int \frac{ds}{v}$. This approximation, neglecting perturbations to the flow introduced by the cell, is expected to be reasonable for streamlines that do not pass very close to solid walls. We initially attempted an approach, where the displacement of the hemisphere from a given position was along its velocity, v, which was obtained from the simulation with the hemisphere, but we found this approach impractical, because it required excessive computational resources. We chose smaller distances between consecutive positions of the hemisphere in regions with greater variations of flow velocity along the streamline.

Mechanical stimulus experienced by a cell moving in a flow can result from forces applied to the cell surface and to the cell body. The former originate from mechanical stresses in fluid around the cell and the latter originate from the gravity and acceleration. To quantify the mechanical stimulus experienced by a cell in a flow and to compare stimuli in different flows, it would be helpful to have a single parameter representing the strength of the stimulus. The problem is, however, that mechanical stress applied to the surface of a cell is usually distributed

over the entire surface, and the stress distributions are different for different types of flow, making the choice of such a parameter somewhat ambiguous. Nevertheless, in many cases, including the native aquatic environment, cells are expected to move with the mean velocity of the flow and the rate of strain in the flow is not expected to substantially vary on the 35 μm scale of the cell diameter. Thus, if a spherical cell is divided into two halves by a plane of symmetry, the forces experienced by the two halves (integrals of stresses over surfaces of the halves) always form a pair (equal in magnitude opposite in direction). The magnitude of those forces reaches a maximum at a certain orientation of the plane of symmetry. We believe this maximal value of the force magnitude is a reasonable choice for the parameter representing the strength of mechanical stimulus for the purpose of comparison between the native aquatic environment, the previously used laboratory setups (Couette flow and flow in a pipe), and our microfluidic setup. (We note, however, that this variable hides some of the differences between different types of flow, such as two-dimensional and three-dimensional flows, and would be problematic for the microfluidic setup we used before, where cells were pushed against a barrier.[33])

Because our simulations were with hemispheres moving in the *xz*-plane of symmetry of the microfluidic device, we looked for the maximum force magnitude by dividing the hemisphere into two halves (corresponding to quarters of an actual spherical cell) with planes of symmetry parallel to the *y*-axis and tilted at different angles with respect to the *x*-axis. For each orientation of the dividing plane, we used the results of the simulation to obtain the *x*- and *z*-components of the surface forces acting upon the first and second halves of the hemisphere, $F_{1,x}$, $F_{1,z}$, $F_{2,x}$, and $F_{2,z}$ and calculated the magnitude of one force in the pair of forces on the two halves as $F_h = \sqrt{\left(\frac{F_{1,x} - F_{2,x}}{2}\right)^2 + \left(\frac{F_{1,y} - F_{2,y}}{2}\right)^2}$. The orientation of the division plane was then

iteratively modified, starting from an angle of -45° with respect to the *x*-axis, to obtain a maximum value of the force magnitude, $F_{h,max}$. The representative magnitude of the tensile force on the whole spherical cell was calculated as $F_t = 2F_{h,\max}$. We tested this approach by calculating $F_{h,max}$ on a 35 µm hemisphere in a plane Couette flow (in the middle of a 150 µm gap between two plates moving at equal speeds in opposite direction). The calculated value of $F_{h,max}$ was within 4% of the theoretical prediction $F = \frac{5}{8}\pi D^2 \eta\gamma$, [35] indicating that our approach worked reasonably well and providing an estimate for the computational error. We note that $F_{net} = \sqrt{\left(F_{1,x} + F_{2,x}\right)^2 + \left(F_{1,y} + F_{2,y}\right)^2}$ is the magnitude of the force acting upon the hemisphere, and even when the net force is expected to be zero, the net force value obtained from numerical simulations is not an exact zero, because of the computational errors.

Cell culture and treatment

Cells were taken from a culture of *L. polyedra* (Stein) Dodge strain CCMP 1932 and were grown on a 12:12 hour light-dark cycle in an environmental chamber at 20.0 ± 1.0˚C in half-strength Guillard's f/2 medium minus silicate. For microfluidic experiments, cells were concentrated to 6,000-12,000 per mL. Cells from the test populations were examined post-assay to verify they were still healthy and motile.

In our experiments we tested *L. polyedrum* cells treated with 10 µM latrunculin B, 1 µM oryzalin , both dissolved in dimethyl sulfoxide (DMSO), and with 0.17% as a control (all obtained from Sigma-Aldrich). Cells treatments were performed treated during the dark cycle, approximately 1 hour before testing. Both oryzalin and latrunculin B are known to target the cytoskeleton, with oryzalin acting on microtubules and latrunculin B acting on F-actin networks.

Specifically, oryzalin depolymerizes tubulin to disrupt microtubules and prevent new ones from growing. Latrunculin B depolymerizes F-actin and inhibits new polymerization of actin, which is responsible for anchoring, binding, and directing the growth of microtubules.

Results:

Numerical simulations

The pattern of streamlines in the plane of symmetry of the device obtained from numerical simulations without a cell (Fig. 2-2) shows that the streamlines originating from the vertical capillary (where cells come from) are focused to a relatively thin layer (small *z*-axis extension) near the ceiling of the horizontal channel. Specifically, streamlines, which stay away from the walls by at least 17.5 μm (cell radius, *D*/2) everywhere and are thus accessible to cells, end up at distances of 24.5 – 43.5 μm from the ceiling. These distances correspond to 7.0 - 25.5 μm clearances between the ceiling and cells moving along these streamlines. Near the corner at the downstream edge of the vertical capillary, where the streamlines cross from the capillary into the channel, the cell-accessible streamlines have large curvatures, and there are sharp increases in the flow velocity and shear rate along the streamlines (from $<6\ s^{-1}$ shear rate in the capillary). Therefore, cells moving along these streamlines are expected to experience large increases in the hydrodynamic stress over short time intervals. The analysis of streamlines that are out of the plane of symmetry of the device indicates that, when cell-accessible streamlines cross the edge of the capillary, the directions of these streamlines are largely along the radius of the capillary and at angles from -30° to 30° from the *x*-axis. Therefore, whereas the diameter of the capillary is 1 mm, the cell streamlines enter the horizontal channel within ~500 μm wide strip near the middle of the channel. (This focusing of the streamlines towards the middle is due to the

relatively large cross-section of the capillary and low flow velocity in it as compared with the flow velocity in the horizontal channel.) Therefore, the *x*-axis coordinates of the edge-crossing locations are all within a range of 70 μm for all cells. Given the characteristic velocity of ~20 mm/s for cell streamlines in that area, this range corresponds to a time difference of ~3.5 ms. Because this time difference was relatively small, in the analysis of our experimental results, we used the same *x*-axis position (the downstream edge of the capillary in the vertical midplane) as the reference position of passage under the capillary edge for all cells.

The dependences of flow velocity on time along cell-accessible streamlines indicate that accelerations experienced by cells are on the order of ~2 m/s^2 (from near zero velocity to ~20 mm/s within ~10 ms), which is only ~20% of the gravitational acceleration, 0.2g. Previous work has shown that *L. polyedra* cells do not luminesce even when exposed to accelerations as high as 20g[36]. Therefore, we concluded that inertial forces caused by the accelerations were unlikely to trigger bioluminescence. Next, we ran a simulation with the hemisphere near the ceiling of the horizontal channel sufficiently far downstream from the vertical capillary, where the flow is pure shear. The tilt of the division plane with respect to the *x*-axis that maximized the value of F_h was close to -45° such that the tensile forces applied to the two halves of the hemisphere, F_1 and F_2, formed a pair along a line at 45° above the *x*-axis, as expected for pure shear flow in the *xz*-plane.

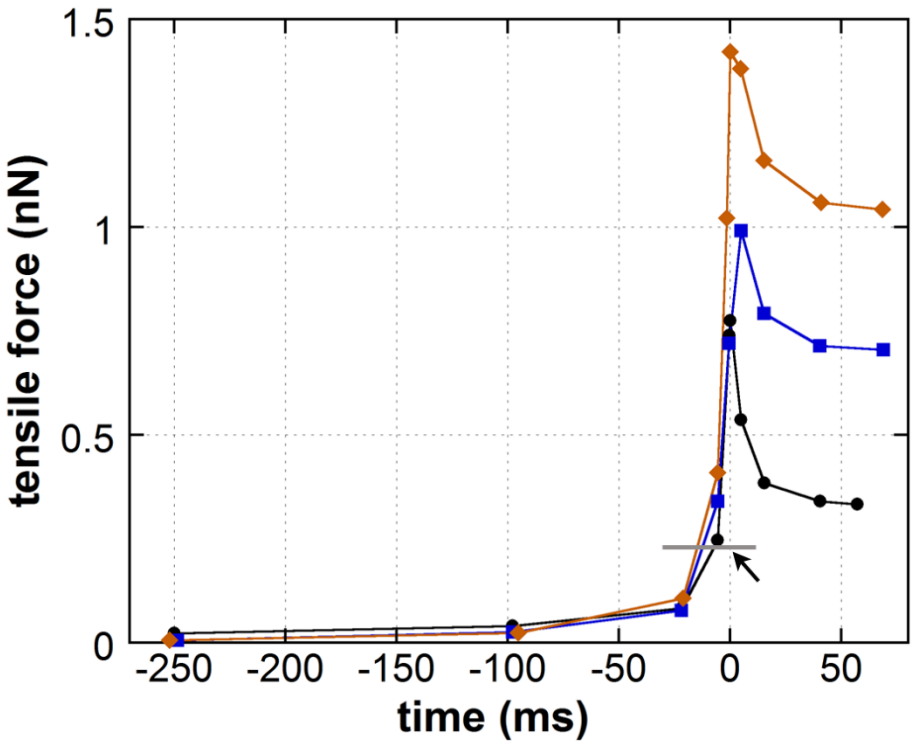

Figure 2-4: Tensile force experienced by a 35 µm sphere, representing a L. polyedra cell, as a function of time in the flow through the microfluidic device (Lagrangian reference frame) from numerical simulations in Comsol.
The sphere was placed at different locations along three selected streamlines (cf. Fig. 2-2), the tensile force experienced by the sphere (the ordinate) was calculated, and the passage time between consecutive locations along the streamline was computed (differences in the abscissa). The streamlines were all in the vertical plane of symmetry of the device, one passing near the center of the vertical capillary (blue squares), one passing near the front (downstream) side of the vertical capillary (red diamonds), and one passing near the back (upstream) side of the vertical capillary (black circles). Lines connecting the symbols are shown to guide the eye. For all three streamlines, time equal zero corresponds to the position of the sphere exactly beneath the downstream edge of the vertical capillary. A grey line highlighted by a black arrow marks a tensile force of 0.24 nN, corresponding to a force on a *L. polyedra* cell at a shear rate of 100 s^{-1}, a putative threshold for luminescence of *L. polyedra*[12].

We placed the cell (hemisphere) at different points along the streamline that is initially (upstream of the horizontal channel) parallel to the axis of symmetry of the vertical capillary, obtained the value of the tensile force on the whole sphere, F_t, at every point and calculated the dependence of F_t on time, *t*, in the Lagrangian reference frame along the streamline. The results

indicated that, after cell enters the horizontal channel, F_t reaches a plateau of 0.7 nN, corresponding to the value of F_t in a macroscopic shear flow with a shear rate of 300 s^{-1}. (It is lower than the rate of 800 s^{-1} at the ceiling, because the center of the cell is moving at 28μm below the ceiling.) On the other hand, F_t is very low (<0.05 nN) while the cell is moving through the capillary. However, starting from ~50 ms ahead of the moment when the cell passes under the downstream edge of the capillary (t = -50 ms in Fig. 2-4), the value of F_t begins to rapidly increase, reaching 10% and 25% of the plateau value at t = -23 and -9 ms, respectively. In addition, as the cell passes under the edge, F_t has a ~20 ms long spike, when it reaches a level 33% above the channel plateau.

The simulations were repeated for cells (hemispheres) on streamlines passing close to back (downstream) and front (upstream) sides of the vertical capillary. The dependencies of F_t on time (Fig. 2-4) were similar, but as expected, the horizontal channel plateau value was higher (>1.0 nN) for the cell coming from the front side of the capillary, which passed closer to the ceiling of the horizontal channel, and lower (~0.35 nN) for the cell from the back side of the vertical capillary, which passed further away from the ceiling. Notably, the ratio between the heights of the spike and of the plateau was greatest (~2.3) for the cell coming from the back side of the capillary. It was most likely because the spike results from the extensional strain at the entrance of the horizontal channel, where the liquid experiences a large acceleration over a short distance, leading to a large rate of extension and to a substantial tensile force in addition to the force originating from the shear flow in the horizontal channel. The trajectory of the cell from the back side of the capillary is farthest away from the ceiling, resulting in the largest velocity in the horizontal channel, a large rate of extension over an extended time and, hence, a tall spike of

the force on the cell and a large area under the spike. On the other hand, the force on the same cell in the horizontal channel is lowest.

We did not perform simulations of the dependence of F_t on time for cells moving not in the plane of symmetry of the system, since those simulations would be substantially more difficult (because the direction of the maximal pair of forces would be much more difficult to find *etc.*). However, taking into account that cells entering the horizontal channel move radially within a relatively narrow range of angles (-30° to 30°) with respect to the *x*-axis and that the time dependencies of F_t are similar for different trajectories that are in the plane of symmetry (Fig. 2-4), we assumed $F_t(t)$ in Fig. 2-4 to be representative of all cell trajectories. Based on the previous experiments on *L. polyedra* in a macroscopic setup[12], where the shear rate threshold for luminescence of *L. polyedra* was estimated at as low as ~100 s^{-1}, corresponding to $F_t \approx 0.24$ nN, we considered that in our microfluidic experiments, luminescence is triggered, once F_t reaches this level (marked by a grey line in Fig. 2-4). For the three simulated flow trajectories, the average interval between F_t passing the level of 0.24 nN and cell reaching the downstream edge of the capillary ($t = 0$) was $\Delta t_0 \approx 12.5$ ms.

Measurements of cell velocities

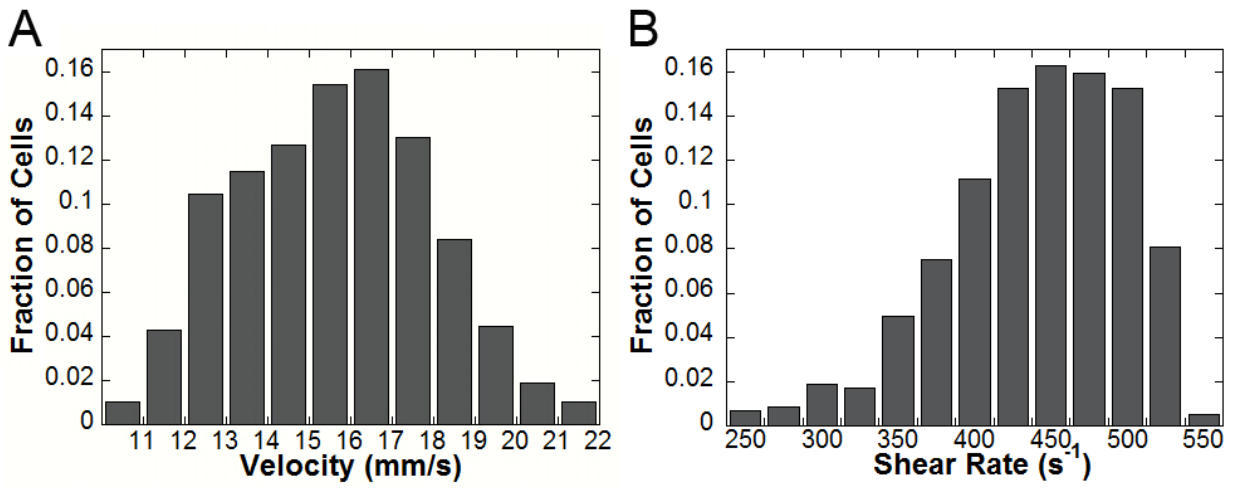

Figure 2-5: Characteristics of cell trajectories of *L. polyedra* in the horizontal channel of the microfluidic device.
(A) Distribution of cell velocities from measurements of streak lines produced by moving cells under the oblique (darkfield) laser light illumination. (B) Distribution of shear rates in the horizontal channel obtained from the results of numerical simulations in Comsol (cf. Fig. 2-2) for the distribution of velocities in panel A, disregarding the perturbation to the flow from moving cells.

The distribution of velocities of cells in the horizontal channel obtained from the analysis of streak lines of 585 cells (Fig. 2-5A) had a mean value $\bar{v}$ = 15.6 mm/s and a coefficient of variance(CV) of 15%. This value of CV was about two times smaller than the value for the case, when cells are evenly spread over the entire depth of the horizontal channel (or over its upper half), suggesting that the hydrodynamic focusing of the dinoflagellates to the ceiling of the horizontal channel substantially reduced the variability of their velocities. We used the value of $\bar{v}$ to calculate the characteristic time it took cells to reach an area, where their luminescence could first be detected after they passed the downstream edge of the vertical capillary, as $\Delta t_1 = \Delta x_1 / \bar{v} = 7.5$ ms (where $\Delta x_1 = 120$ µm). The cumulative latency when luminescence would first be reliably detected was thus $\Delta t = \Delta t_0 + \Delta t_1 \approx 20$ ms.

We used the results of the numerical simulations for the dependencies of flow velocities and local shear rates on the *z*-axis position in the horizontal channel to convert the distribution of flow velocities into a distribution of shear rates (neglecting perturbations to the local flow velocity introduced by a cell). The distribution of shear rates (Fig. 2-5B) had a mean of 428 s^{-1} and a CV of 14%. For cells evenly spread over the depth of the horizontal channel, the value of CV would be 4.5 times greater at ~63%. (The number is so large, because a large portion of cells would move along the streamlines near the channel midplane, where the velocity is highest, while the shear rate is close to zero). Therefore, the hydrodynamic focusing greatly reduced the variability of the shear rate and, hence, of the mechanical stimuli experienced by cells in the horizontal channel and was thus essential for setting proper experimental conditions. Tighter hydrodynamic focusing of cells (to a thinner layer near the ceiling of the horizontal channel) would reduce the variability of velocities and shear stresses even further. Nevertheless, the improvement would be relatively small and would come at a cost of a reduced experimental throughput, because it would require a smaller ratio Q_2/Q_3, resulting in a smaller number of cells per passing through the horizontal channel per unit time.

Measurements of bioluminescence

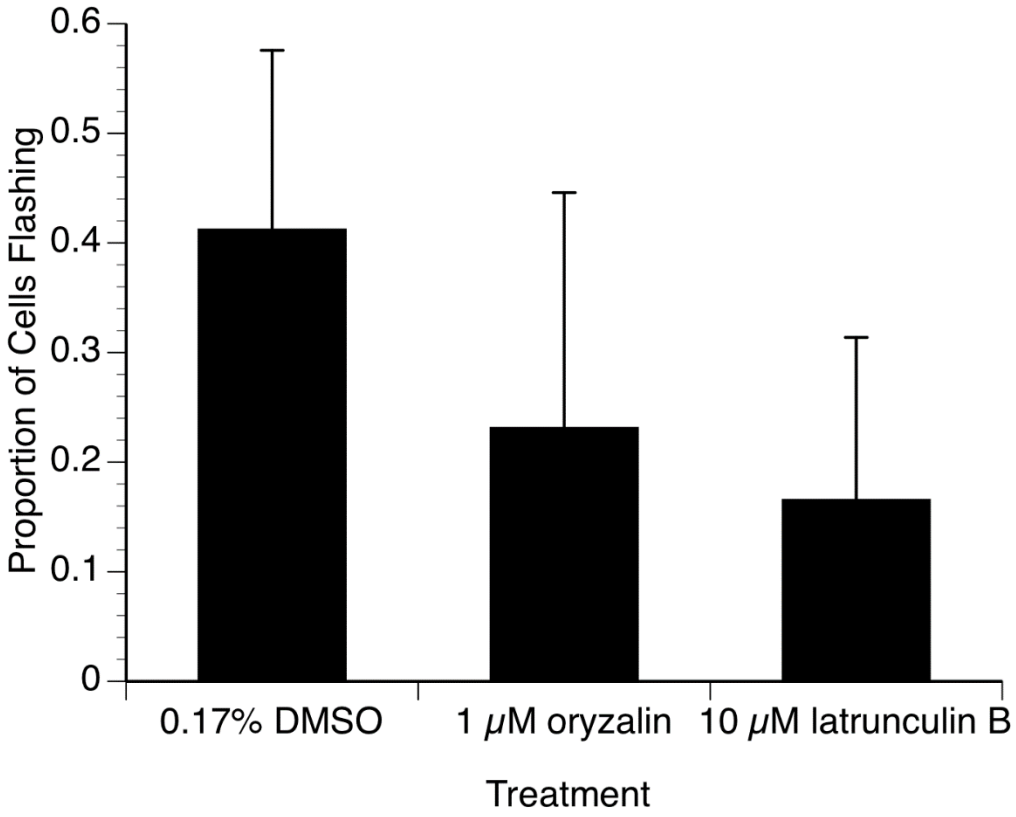

Figure 2-6: Proportions of cells of *L. polyedra* that emitted luminescent light (flashed). Proportions of cells of *L. polyedra* that emitted luminescent light (flashed) in the horizontal channel of the microfluidic device for untreated cells (treatment with 0.17% DMSO 1 hr before the experiments; control) and for cells treated with 1 µM oryzalin and 10 µm latrunculin B, both 1 hr before the microfluidic experiments. The numbers of cells are N = 9,600, 7,700, and 5,800, respectively. Error bars are SD.

We tested the luminescence of *L. polyedra* cells in the microfluidic device in a total of nine series of experiments performed on nine different days. In each series, we separately tested the luminescence of *L. polyedra* cells treated with latrunculin B, oryzalin, and DMSO (control), analyzing the totals of, respectively, ~5800, 7700, and 9600 individual cells for the three types of treatments. The proportion of luminescent cells, which we called flash fraction, for the control cell group varied between different experiments from 12 to 59%, with an overall average of 40.5%. This flash fraction is comparable with the one observed for untreated *L. polyedra* cells at

in the microfluidic device in the previous work at the lowest flow velocity tested (40 nM force on the cells)[33]. The flash fractions in cell populations treated with oryzalin and latrunculin B were markedly smaller, at 23.4% and 13.4%, respectively, corresponding to the respective reductions by ~4/10 and ~2/3 as compared with the control. The flash fraction reduction for cells treated with latrunculin B vs. cells treated with DMSO was statistically significant ($p = 0.018$). On the other hand, for cells treated with oryzalin, there was no significant difference in the flash fraction as compared with the DMSO control ($p = 0.11$), because the flash fraction changed a lot between individual experiments, varying from 5% to 63%, with the latter number being greater than the flash fraction measured in the same series of experiments (on the same day) for the DMSO control (54%).

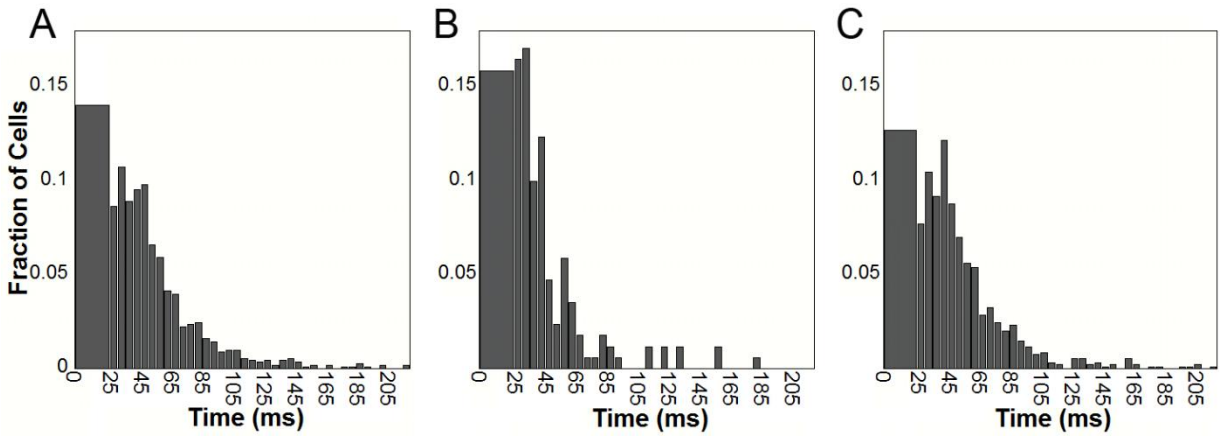

Figure 2-7: Distributions of the latency in the luminescence of *L. polyedra* in response to mechanical stimulation by hydrodynamic stresses in the microfluidic device.
The latency is calculated based on the position (*x*-axis coordinate) in the horizontal channel where luminescence first became detectable and on the average velocity of cells in the channel (cf. Fig. 2-5A). Histograms of the response latencies are shown for (A) untreated cells (0.17% DMSO control), (B) cells treated with 10 μm latrunculin B, and (C) cells treated with 1 μm oryzalin. The histograms only account for cells that were flashing in the ~4.9 mm long field of view in the horizontal channel. Based on the results of the numerical simulations, the initial exposure to a stimulus large enough to trigger luminescence was considered to occur ~20 ms before cells reached the region where luminescence was reliably detectable (>120 μm downstream of the edge of the vertical capillary). Therefore, the first bins are 25 ms wide and include all cells that were luminescent during the first 5 ms in the zone of detectability.

The luminescence response latencies were analyzed for a series of experiments, in which we observed 170 flashes of cells treated with latrunculin B, 946 flashes of cells treated with oryzalin, and 1110 flashes of cells in the control group (Fig. 2-7). Because, the cumulative latency at the most upstream point where luminescence was reliably detectable was estimated as $\Delta t \approx 20$ ms, the first bins of the distributions, accounting for cells flashing during the first 5 ms in the zone of detectability, are 25 ms wide. The optical setup, with $L_{opt} =$ 4.9 mm long field of view along the horizontal channel, enabled the detection of luminescence for latency times, $L_{opt} / \bar{v}$, up to ~300 ms. Nevertheless, there were practically no flashes initiating past the first 200 ms after the initial exposure to hydrodynamic stress for any of the three populations of cells, with ≥90% of flashes having latencies of 100 ms or less. Moreover, in each case, 10 - 15% of cells had latencies of 25 ms or less. We note that all flashes that started in the zone of detectability (latencies of ≥25 ms) had durations of 40 ms or more (usually, 40 – 70 ms; data not shown), suggesting that flashes with latencies of ≤20 ms were all detected and accounted for. The distributions of the latency times for cells treated with DMSO and oryzalin were visually similar and statistically indistinguishable. On the other hand, the latency times for cells treated with latrunculin B were on average 23% shorter with about one half of all flashes having latencies of 35 ms or less. To compare the distributions we performed two sample t-tests and found that the DMSO and oryzalin populations had an indistinguishable mean latency time ($p=0.91$) and that DMSO and latrunculin B had a significantly different mean latency time ($p=0.0026$).

Discussion and Conclusions:

Previous studies

Previous laboratory experiments on luminescence of dinoflagellates in response to mechanical stimulation in flows were mostly performed in traditional tabletop setups, with flows in pipes[11,29] or between rotating concentric cylinders (Couette flow)[12,13,28,37,38]. These setups made it possible to study bioluminescence in laminar and turbulent flows with a broad range of hydrodynamic stresses and to register a large number of flashes in each experiment. Nevertheless, the tabletop setups are not well suited for testing two key parameters of bioluminescence, the proportion of cells flashing at a given level of hydrodynamic stress and the delay between the inception of stress and beginning of a flash (luminescence latency). The characteristic length scale, *d*, in a tabletop setup (the diameter of the pipe or the width of the gap between the cylinders in a Couette system) is typically ~1 cm, resulting in a characteristic viscous diffusion time, $t_{vd} = d^2 / \nu$, of ~100 sec, where ν = 1 mm^2/s is the kinematic viscosity of water. In a Couette system, the value of t_{vd} sets the scale for the time of transition to a fully developed laminar flow, after one of the cylinders starts rotating (or changes its velocity). In a continuous laminar flow through a pipe, t_{vd} sets the time scale for an element of fluid entering the pipe (from a pipe with a different cross-section) to reach the region with a fully developed parabolic velocity profile.

In the beginning of the transition in a Couette system and at the entrance into a pipe, the profiles of flow velocities and hydrodynamic stresses tend to be substantially different from those in the eventual fully developed laminar flow. In a Couette flow setup, there is a large shear rate near the cylinder that started rotating (much larger than the average shear rate in the fully developed laminar flow), and very little shear rate elsewhere. As a result, bright bioluminescence

is observed immediately after one of the cylinders starts rotating[12,13,28,38] (or even when both cylinders start rotating[39], such that the shear rate becomes zero, when the flow is fully developed), and this luminescence rapidly decays with time. In a pipe, the initial flow profile is trapezoidal rather than parabolic, with very little shear outside of a thin layer near the walls. Because for d = 1 cm the transition time, t_{vd}, is much greater than the time of luminescent response of dinoflagellates to mechanical stimuli (~100 s vs <0.1 sec), the latency in the response is practically impossible to measure. Moreover, because t_{vd} is so much longer than the luminescence response time, the first flashes of bioluminescence in tabletop systems are generally expected to occur in response to some transient flow conditions.

A dinoflagellate cell (such as *L. polyedra*) can flash with a finite probability in response to a range of hydrodynamic stresses and is less likely to flash, if it flashed a short time before. One of the mechanisms of this desensitization is the depletion and exhaustion of the reservoirs of luciferin, which are always limited and are particularly small for smaller dinoflagellates, such as *L. polyedra* that can only produce 2 – 4 consecutive flashes (while much larger *Pyrocystis fusiformis* can flash as many as 50 times)[11,33]. For example, after rapid large increases in bioluminescence of *Pyrocystis noctiluca* in a Couette flow that were caused by abrupt transitions to turbulence[28,38], luminescence decayed on a scale of a few seconds, while the flow remained turbulent. When an *L. polyedra* suspension was mechanically agitated with a mesh, eliciting luminescence flashes, the apparent luminescence threshold (the shear stress, at which luminescence became detectable) in a subsequent test in a pipe flow was as much as 2-times greater as compared with tests on suspensions that were not pre-agitated[29]. Notably, significant desensitization can occur within a few seconds of exposure of dinoflagellates to hydrodynamic stress even without luminescence (and hence, without the luciferin depletion)[12]. When in a

developing flow, a cell has a history of exposure to various hydrodynamic stresses. Therefore, the large value of t_{vd} and the continued variation of hydrodynamic stresses during the transition time make tabletop flow systems also poorly suited for finding the bioluminescence threshold and for quantitative assessments of the dependence of the proportion of flashing cells on hydrodynamic stress.

One of the approaches used in the tabletop experiments was to start measuring luminescence only after the laminar flow was fully established. In a Couette flow, it required waiting for 20 sec after the cylinder rotation velocity changed[13]. In a pipe flow, the measurements were taken at a large distance from the pipe entrance (67 cm for a 0.67 diameter pipe), after cells spent in the shear flow times ranging from 0.4 sec (high shear stresses) to 20 sec (near the putative threshold)[29]. The initial series of luminescent flashes (Fig. 2-7) that in our microfluidic experiments at the characteristic shear rate of 400 s^{-1} (Fig. 2-5b) lasted for only ~0.2 sec, with ~40% of cells flashing (Fig. 2-6), would be impossible to detect with this tabletop experimental approach.

The tabletop experiments relied on sensitive photodetectors and the luminescence of as low as 10x above the background was considered to correspond to above-the-threshold levels of the mechanical stimulus (shear stress). Nevertheless, given the data in Fig. 2-7 in Ref. [12], it is reasonable to assume that the probability of a cell to flash per unit time (flashing rate) would be greatly reduced after 20 sec of continuous exposure to a constant shear stress. The Couette flow experiments indicated that the decay in the flashing rate past 20 sec in the flow was relatively slow[13], but it was, most likely, a different and much slower mode of decay than during the first 0.2 sec (Fig. 2-7) or even the first 10 sec[12]. (Also, as noted above, the decay in luminescence of *Pyrocystis noctiluca,* after it spiked in response to stepwise increases in hydrodynamic stresses,

occurred on a scale of several seconds[28,38], while these dinoflagellates are likely to be able to produce a larger number of flashes, because of their >10 greater volume as compared with *L. polyedra*). Therefore, the threshold shear stress for *L. polyedra* luminescence found in the tabletop experiments, 0.1 Pa in the Couette flow[13] and 0.2 – 0.4 Pa in the pipe flow[11,29], may be substantially higher than the shear stress threshold for the first luminescent flash after a rapid increase in the shear stress. The assessment of the proportion of flashing cells at a given shear stress by the measurements of luminescence in the developed tabletop Couette and pipe flows was even more problematic, because it was impossible to account for cells that flashed, before the measurements started (when the detector was activated in the Couette flow setup or cells passed by the detector in the pipe flow setup; also see below).

A greatly reduced value of t_{vd} was achieved in a small Couette setup with a narrow gap, d = 0.64 mm, making it possible to produce linear ramps of shear rate as short as 1 sec with largely uniform distributions of shear rate over the annular gap[12]. The experiments on *L. polyedra* in this setup led to an estimate of the luminescence threshold at shear rates of 50 – 100 s^{-1} for different strains. The experiments also revealed that when the time of the ramp to the final shear rate of 400 s^{-1} is extended from 1 to 8 sec, the cumulative luminescence (integrated over 20 sec) drops as much as 6-fold. This desensitization occurred without the depletion of luciferin and was likely because of adaptation of *L. polyedra* cells to the growing stimulus.

This type of adaptation can be rationalized in the framework of bioluminescence as an anti-predation behavior. Common predator of *L. polyedra*, such as copepods, produce feeding currents with stresses estimated at only ~0.01 Pa[12], not much higher than typical hydrodynamic stresses in the oceanic flows. The stresses are substantially higher in the euphausiid feeding currents (0.06 – 0.10 Pa) and during copepods burst swims (~0.1 Pa) and may also be higher,

when *L. polyedra* cells are handled by copepod feeding appendages (that is estimated to last for ~100 ms)[12,13]. Nevertheless, these stresses are all near the putative threshold of luminescence of *L. polyedra* in Couette setups. A common feature of the flows generated by the predators is that the hydrodynamic stresses increase very rapidly. For example, when a copepod, which is ~1 mm in diameter, performs a burst swim at 50 mm/s, at a point with a rate of strain of 50 s^{-1} (0.6 mm from the animal) the rate of strain increases at 1,200 s^{-1}, corresponding to a characteristic time of <20 ms. Therefore, to optimize their luminescent flashing for anti-predation, *L. polyedra* would be most sensitive to mechanical stimuli applied within 100 ms or less (and progressively lose their sensitivity for longer application times; an implementation of a high-pass filter). Hence, it is reasonable to assume that there would be more cells flashing at shear rates 50 – 500 s^{-1}, if these shear rates are applied within ≤100 ms, which is 10 times less than in the Couette flow with a small gap in Ref.[12] and which would generally be difficult to implement in a controlled way in a tabletop setup.

In addition, tabletop flow setups tend to have relatively thick walls that, together with large *d*, makes them less accessible to high numerical aperture (high-NA) lenses, which normally have short working distances. The use of relatively low-NA optics limits the resolution of imaging and efficiency of collection of bioluminescent light that are achievable with tabletop systems. In addition, because of the relatively large values of *d*, cell velocities tend to be high even at moderate shear rates, making it difficult to track individual cells, especially when cells are as small as *L. polyedra* and do not flash.

The situation changes, when *d* is reduced to ~0.1 mm (or less), corresponding to a microfluidic setup and resulting in t_{vd} of ≤10 ms. In the only previous study of dinoflagellate bioluminescence in a setup with such small value of *d* [33], *L. polyedra* cells were exposed to a

sharp increase in mechanical stimulus, when they arrived at a barrier with a 15 μm clearance, while moving through a 200 μm deep channel. Numerical simulations were used to show that a cell experienced a 50-fold increase in the strength of the mechanical stimulus within <2.5 ms before its arrival at the barrier. The very short time of inception of the stimulus and the stationary positions of cells at the barrier (greatly facilitating the collection of luminescent light) made it possible to measure the response latency of bioluminescent flashes with a high resolution of 4 ms (frame rate of the camera). The mean and minimal response latencies (for cells that flashed) were 31 and 16 ms, respectively, at the lowest level of stimulus and decreased to 15 and 12 ms, respectively, at the highest level of stimulus.

That microfluidic setup had several significant drawbacks, however. All cells arriving at the barrier (whether or not they flashed) had to be removed from it. To this end, every time after several cells arrived at the barrier and their luminescence response was recorded, the experiment had to be interrupted by changing the configuration of flow in the device and directing the cells at the barrier to a special (waste) outlet. The necessity of regular operator-initiated interruptions led to relatively low numbers of cells being analyzed (low throughput). Moreover, to analyze even a moderate number of bioluminescent flashes, the device was operated in a regime with relatively high flow velocities. As a result, the estimated hydrodynamic forces applied to cells at the barrier (triggering the flashes) were in the range of 40 - 400 nN. The entire range was way above the putative luminescence threshold of 0.24 nN, as estimated from previous experiments in Couette flow setups[12,13] (shear rate of 100 s^{-1}). Last but not least, nearly the entire surface of a cell at the barrier experienced hydrodynamic drag in the downstream direction, while the opposing force was applied at two points (likely, two very small areas) of contact between the cell and the barrier wall and the cell and the bottom of the microfluidic channel. This type of

distribution of forces over the surface of the cell is clearly different from the distribution experienced by cells in tabletop flow setup or in the ocean, and in fact, the mechanical stimulus applied to cells in that previous microfluidic setup was somewhat similar to pushing cells with a object (contact force)[32].

Proposed experimental setup

The microfluidic setup in the present study is based on a continuous flow that has made it possible to analyze ~1000 cells in a single 30-min long experimental run. The experimental setup enabled the observation of bioluminescence as early as 20 ms after *L. polyedra* cells were first exposed to a mechanical stimulus (hydrodynamic stress) at a level potentially capable of triggering their luminescence (a force of 0.24 nN). The observation window stretched to as late as 300 ms after the first exposure (4.9 mm field of view at 16 mm/s flow velocity). Given that the shortest luminescent flashes were ~40 ms and there were practically no flashes observed after ~200 ms (Fig. 2-7), the experimental setup thus guaranteed that all flashes were properly detected and recorded (just as in the previous microfluidic setup). Importantly, unlike in the previous microfluidic setup, in the present setup, luminescence is triggered by exposing cells to a flow that results in smooth distributions of stresses over the cell surface, making it similar to flows in the ocean and in tabletop laboratory setups. In addition, the characteristic force applied to a cell in our experiments was ~1 nN and the characteristic shear rate (Fig. 2-5b) was 400 s^{-1}, on the same order as the shear rates that *L. polyedra* are likely to be exposed in the ocean and that were previously tested in the laboratory experiments on bioluminescence[11–13,28,29,37,38]. Therefore, our results directly connect to a considerable body of literature on bioluminescence of dinoflagellates in laboratory flow setups and in the ocean.

Our experiments were enabled by two additional major custom-built elements of the experimental setup. The video microscopy setup had an oblique angle (darkfield-type) laser illumination, two simultaneously operating cameras, and a laser-blocking filter, making it possible to separately register every cell passing through the field of view (by recording the scattered laser light with a regular CCD camera) and every flashing event in the field of view (by recording the faint luminescence light with a sensitive EMCCD camera). This arrangement enabled accurate evaluation of the proportion of flashing cells (flash fraction). *L. polyedra* suspensions were fed to the microfluidic device from a specially designed cuvette, which was water tight, but had oxygen-permeable walls, making it possible to keep the suspension aerated, without mechanically stirring it. (The stirring could have caused uncontrolled pre-mature luminescence.) In early experiments, when *L. polyedra* suspension was held in a syringe without oxygen impermeable walls, the proportion of flashing cells was much lower, suggesting that proper aeration was essential to maintain cells healthy and luminescence-capable.

Another novel aspect of the present work is detailed numerical simulations of the dynamics of mechanical stimuli experienced by cells, as they move through the microfluidic device. It is worth noting that we performed the simulations with a basic package of the popular Comsol software, which is relatively inexpensive and easy to use even for those without much training in numerical simulations. This package does not allow modeling solid objects, such as a *L. polyedra* cell, moving in a flow. Nevertheless, we were able to bypass this limitation by modeling a cell as a spherical domain with a diameter $D = 35$ μm and with a high viscosity. This approach was validated in a simple shear flow, where the sphere was found to be rotating at an angular velocity, ω, equal to 1/2 of the shear rate, γ, and its two hemispheres (with the dividing plane at 45° to the flow velocity) were found to experience opposing forces of $\frac{5}{8}\pi D^2 \eta\gamma$, with

both results in agreement with theoretical predictions[35]. The numerical simulations used date from experimental measurements of velocities of cells in the horizontal channel and provided information on the time courses of exposure of cells to hydrodynamic stresses along different flow pathlines. The results of the numerical simulations were valuable in multiple respects: (1) provided the first detailed data on the time courses of forces experienced by dinoflagellate cells in a flow in a laboratory setup (Fig. 2-4); (2) they made it possible to obtain the shear rates around cells in the horizontal channel based on the experimentally measured velocities (Fig. 2-5A and B); (3) they provided data on the variability of forces experienced by cells following different trajectories (Fig. 2-4); (4) they made it possible to estimate at what point in space and at what time the forces reached a putative threshold for triggering luminescence (Fig. 4); (5) they showed that when entering the horizontal channel, cells experienced short (~20 ms) spikes in the hydrodynamic force (Fig. 2-4).

We note that, because of the parabolic flow profile, shear rate in the horizontal channel varies from zero at the midplane to ~550 s^{-1} at 17.5 μm from the ceiling and to 800 s^{-1} at the wall. Because the flow velocities are largest near the midplane, where the shear rate is close to zero, if the centers of cells were uniformly distributed over the depth, *z*, of the horizontal channel (apart from $D/2 = 17.5$ μm thick layers near the ceiling and floor; Fig. 2-2), the coefficient of variation, CV, of shear stresses along cell trajectories would be as large as 63%. (This value is calculated, taking into account that, in an experiment, the numbers of streaklines by cells from a given layer of the horizontal channel, Δz, is proportional to the flow velocity in this layer.) For experimentally recorded cell trajectories in the horizontal channel, CV of the shear rate was estimated at only ~14%, indicating that the hydrodynamic focusing of cells towards the ceiling reduced the variation of the shear stress 4.5-fold and was thus essential for setting suitable

experimental conditions. Further reduction of the shear rate variability can be achieved by tighter hydrodynamic focusing, through a reduction of the ratio of the flow rate of the cell suspension to the total flow rate, Q_2 / Q_3. Nevertheless, we consider the present experimental arrangement with $Q_2 / Q_3 = 0.16$ to be a reasonable compromise between minimizing the variability of mechanical stimuli between cell trajectories ($Q_2 / Q_3 \to 0$) and maximizing the number of interrogated cells at given flow rate ($Q_2 / Q_3 \to 1$).

The spike in the force experienced by cells at the entrance to the horizontal channel that is predicted by the numerical simulations (Fig. 2-4) is certainly an unwanted effect. The spike most likely results from a large increase in the flow velocity over a short distance in this region, leading to a large rate of extension and to a substantial tensile force in addition to the force originating from the shear flow in the horizontal channel. (The characteristic shear rate in the horizontal channel is set by the mean flow velocity and channel depth and, hence, is largely independent on the position along the channel.) The large increase of the flow velocity over a short distance is essential for a short transition time (in the Lagrangian reference frame of a moving cell) from a region with a slow flow and a weak mechanical stimulus (below luminescence threshold) to a region with a fast flow and an above the threshold mechanical stimulus. The spike would be suppressed in a device with a tapered horizontal channel[40], whose width is gradually decreasing from the inlet towards a downstream rectilinear segment with a constant shear rate, thus reducing the rate of extension to a minimum. Nevertheless, in such a device, the time of transition from low to high mechanical stimulus would be inevitably extended, and it is not clear, what microchannel profile would eliminate the spike in the force (Fig. 2-4), while maintaining the short time of transition.

A short duration of the transition (rapid onset of the stimulus) is necessary for high-resolution measurements of latency times of bioluminescence. In addition, as argued above, a rapid (<100 ms) exposure to a relatively large hydrodynamic stress may better emulate the conditions causing luminescence of *L. polyedra* near a predator in the ocean and may reduce the luminescence threshold (as compared to slower exposure to hydrodynamic stresses.) We note that for the central flow pathline in Fig. 2-4, the force on a cell remains <20% of the force in the horizontal channel (plateau) until $t \approx$ -20 ms. The characteristic shear rate in the horizontal channel can be reduced to 100 or 50 s^{-1}, if the flow velocity is reduced by a factor of 4 or 8, respectively, (while keeping Q_2 / Q_3 unchanged). The time of transition to the high shear rate will proportionally increase, but will remain relatively short, at 80 or 160 ms, respectively. Therefore, the proposed setup can be used to measure the flash fractions at shear rates near the putative threshold of luminescence of *L. polyedra*[12] with short transition times and single cell resolution.

The numerical simulations also highlighted the problem of assigning a value to the strength of mechanical stimulus experienced by a cell and of comparing the strengths of mechanical stimuli of different types. Mechanical stimulus can be applied to a small area, e.g., using an AFM tip,[32] or smoothly distributed over the surface of the cell, as in the case of a cell in a flow. It is currently unknown, whether luminescence of a dinoflagellate is triggered when the force applied to a certain small area of the cell surface exceeds some threshold or whether the triggering of luminescence is a cumulative effect of forces (stresses) applied to the entire cell surface. The situation is confounded by the fact that in any type of flow, including pure shear, the distribution of stresses (which are the source of the local forces) over the cell surface is uneven. Moreover, the character of distribution of stresses over the surface of the cell depends on the structure of the tensor of rate of strain, which is different in different flows. Specifically,

turbulent flows and flows in the ocean usually have truly three-dimensional tensors of the rate of strain, with extension and compression along one or two directions each. Simple shear flows, including laminar flows in pipes and Couette systems and flow in the horizontal channel of the microfluidic device away from the entrance, are two-dimensional, with equal rates of extension and compression along two perpendicular axes (both at 45° to the direction of flow) and with rotation at $\omega = 0.5\dot{\gamma}$ around an axis perpendicular to the plane of the velocity gradient.

For the purpose of the present work, we quantified the mechanical stimulus using numerical simulations, by dividing the surface of a 35 μm diameter sphere representing a cell into two hemispheres, calculating the integral forces exerted upon the hemispheres by hydrodynamic stresses, and rotating the plane of the division till the magnitudes of the forces are maximized. This procedure tacitly assumes that the triggering of luminescence is a cumulative effect of hydrodynamic stresses applied to the entire surface of the cell. We note, however, that the distributions of stresses over the surface of a spherical cell are identical in all shear flows. Therefore, the adopted procedure provides a fair comparison between all shear flows, in which the shear rate is spatially uniform (and, by and large, all flows with spatially uniform rate of strain), regardless of whether the triggering of luminescence is local or cumulative. On the other hand, there is no reason to believe that for triggering bioluminescence, a given force would have the same effect, when applied to an entire hemisphere in a shear flow and when applied to a small area (such as with an AFM tip or in the previous microfluidic device).

Experimental findings

In our experiments, the proportion of untreated (0.17% DMSO control) *L. polyedra* cells flashing within 200 ms after a rapid (~20 ms) exposure response to a characteristic

hydrodynamic force of ~1 nN, corresponding to a shear rate of 400 s^{-1} in a macroscopic flow, was ~40% (Fig. 2-6,7). This flash fraction may appear large, considering that in the previous tabletop experiments in a pipe flow, a shear stress of 0.3 Pa was reported as a practical threshold for triggering bioluminescence[11,29], and the proportions of flashing were reported at only 0.02% at the threshold and at ~10% at shear stresses 1.0 – 1.5 Pa (cell forces of 2.3 - 3.5 nN). [11,29] However, in these tabletop experiments, the assessments were made by calculating the proportion of cells that flashed while passing through a 5 cm long segment of a pipe (field of view of the detector) located 67 cm downstream from the pipe inlet. For wall shear stresses of 0.3 – 1.5 Pa, the luminescence from a given cell was only detectable during an average interval of 0.2 – 0.04 sec, after the cell was exposed to the same shear stress for 2.8 – 0.6 sec. As argued above, the prolonged pre-exposure to hydrodynamic stress leads to significant desensitization, and the short observation intervals likely had a confounding effect, further reducing the probability of the detection of luminescence flashes.

The flash fraction of 40% (Fig. 2-6,7) is more in line with the results of experiments in the narrow gap Couette setup, where *L. polyedra* cells were exposed to high shear rates with a 1 sec transition time. In these experiments, the luminescence threshold was measured at 50 – 100 s^{-1} shear rates. Whereas no assessment of the flash fractions was made, the cumulative energy of luminescence increased by more than an order of magnitude between the threshold and a shear rate of 400 s^{-1} [12]. Furthermore, as argued above, we expect the reduction of the time of transition to high shear rate from 1 sec (Ref. [12]) to ~20 ms (our experiments) to result in a substantial increase of the flash fraction and cumulative luminescence. Whereas the shear rate of 400 s^{-1} is large compared with the estimated shear rates produced by the common predators of *L. polyedra*, the relatively large flash fraction of 40% at this shear rate (as compared with <1% in the previous

studies) still provides some quantitative backup for the perceived role of the luminescence as anti-predation behavior.

Interestingly, in the previously reported microfluidic experiments (with cells pushed by flow against a barrier)[33], the proportion of flashing cells was only 50% at a much greater force of ~40 nN (*vs.* ~1 nN in our present experiments). A possible reason for this relatively small increase in the flash fraction as compared to our present tests is that, in the previous microfluidic experiments, *L. polyedra* suspensions were not aerated and their feeding into the microfluidic device was different, possibly resulting in premature mechanical stimulations and luminescence. It is worth noting again that the direct measurements of the proportion dinoflagellate cells flashing immediately after a rapid exposure to a moderate hydrodynamic stimulus (Fig. 2-6, 7) are the first of their kind, making their results somewhat difficult to compare with previous findings.

We have also performed the first direct measurements of the effect of weakening of the cytoskeleton on the flash fraction of dinoflagellates (Fig. 2-6). The proportion of *L. polyedra* cells that flashed in response to a hydrodynamic force of ~ 1 nN decreased from an average of 40% (DMSO control) to substantially lower levels of 23% and 13% for cells treated with oryzalin and latrunculin B, respectively. These results suggest that, when *L. polyedra* cytoskeleton is weakened, it makes them less capable of bioluminescence. Nevertheless, because of the large variability of the proportions of flashing cells between different runs, the decrease was only statistically significant for the treatment with latrunculin B ($p = 0.018$), but not oryzalin ($p = 0.11$). The main reason why the differences between treated and untreated cells, while being substantial, had a relatively small statistical significance is that in our experiments on untreated *L. polyedra* (DMSO control), the proportion of flashing cells differed a lot between separate

experimental runs, varying from 12 to 59%. The exact causes of this large variability are unknown to us, and as argued above, we cannot directly compare our microfluidic experiments with the previous tabletop experiments that measured the flash fractions after extended exposures to constant shear stresses.

A still another parameter that was measured for the first time is the latency of bioluminescence of dinoflagellates after an exposure to a force of ~1 nN at moderate hydrodynamic stress of 0.4 Pa (which is mostly shear). Measurements of the latency were previously performed for a larger non-motile dinoflagellate, *Pyrocystis lunula* (100 – 150 μm long), stimulated by a contact force from an AFM tip, and for *L. polyedra* cells pushed against a barrier by flow with forces of 40 – 400 nN. Somewhat surprisingly, the results (Fig. 2-7) indicated that the luminescence latency at the moderate force of ~1 nN is as short as 20 ms, which is largely the same as found for *L. polyedra* at thegreater forces of 40 – 400 nN and for other dinoflagellates stimulated electrically[21] and with an AFM tip (forces in ~1 μN range).[32] Also, somewhat surprisingly, the distributions of latency times were nearly indistinguishable for untreated cells (0.17% DMSO control) and for cells treated with oryzalin ($p=0.91$). On the other hand, *L. polyedra* cells treated with latrunculin B, which were significantly less likely to flash in the first place, had markedly shorter latency times (23% on average) and a significantly different mean latency time ($p=0.0026$).

Conclusion:

To summarize, we built and used a microfluidic device, in which *L. polyedra* dinoflagellates rapidly transit from a flow with a low shear to a flow with a high shear, becoming exposed to a narrow range of hydrodynamic stresses, which are above the bioluminescence

excitation threshold, but on the order of stresses they are likely to encounter in the oceanic flows. The device was used with an optical setup that enabled reliable detection of every cell, whether luminescent or not, and accurate measurements of cell velocities and luminescent latency times, while analyzing large numbers of cells per unit time (high throughput) with single cell resolution. Detailed numerical simulations of the flow in the device with and without cells provided information on the dynamics of mechanical stimuli (forces) experienced by cells, as they pass through the device, and on the distribution of the forces on cells in the actual microfluidic experiments. Our experiments on *L. polyedra* dinoflagellates provided the first data on (1) the proportions of *L. polyedra* cells that flash within a short time after a rapid exposure to a moderate hydrodynamic stress (flash fraction), (2) the latency of the bioluminescence under a moderate hydrodynamic stress, and (3) the effects of targeted pharmacological weakening of the actin and microtubule components of the cytoskeleton on the flash fraction and latency. Somewhat unexpected results of our study are a relatively high flash fraction (~40%) and short response latency (20 ms) of *L. polyedra* cells at a relatively low shear stress (0.4 Pa). If operated at reduced flow velocities, the proposed experimental setup can be used to measure the flash fractions at lower hydrodynamic stresses, which are produced by the major predators of *L. polyedra*, and to find the threshold of luminescence for rapidly applied stresses.

Chapter 2, in full, is in preparation for submission for publication as “Luminescence of Dinoflagellates upon Rapid Exposure to Shear Flow in a Microfluidic Device”, Ronan, Edward; Latz, Michael; and Groisman, Alex. The dissertation author is first author and a leading contributor to this paper.

3. A Novel Device for Measuring the Elastic Moduli of Soft Gels

Abstract:

Soft gels are used for a myriad of applications where there is a significant desire to know the elastic modulus of the gel. Gels are often made from polyacrylamide or PDMS such as Sylgard 184 and measured using an atomic force microscope, rheometer, or mechanical stretch test. Here we present a novel device capable of quickly and accurately measuring the elastic moduli of samples of gel ranging from 30Pa to 100kPa. The device operates using a rotating arm to produce a shear stress within the gel and the resulting displacement of the top layer is measured by imaging beads attached to the surface. The measurements have high precision with minimal error and are consistent with mechanical and microfluidic tests. Additionally the relaxation times and dependence of elastic moduli on thickness and bake time are shown for Sylgard 184. This device can make elastic moduli measurements simpler, faster, and more practical for regular use.

Introduction:

When investigating cellular biology it is natural to want to reproduce the cellular in vivo environment as closely as possible, particularly in regard to stiffness. Animal tissues range in rigidity over multiple orders of magnitude with elastic moduli softer than 1kPa in the brain to bone exceeding 10gPa[1]. Substrate stiffness has been shown to be influential in many studies such as cell spreading[2], development[3,4,5], migration[6,7], and tumorigenesis[8,9]. On soft substrates we can use traction force microscopy(TFM) to measure displacements of the gel due to the pulling of

cells[10]. This is done through a time lapse imaging of tracer particles deposited on the substrate surface and yields measurements of the actual forces cells are exerting on their environments.

For adherent cells traction forces are an important piece of the puzzle in understanding cell spreading, migration, and polarization, as well as being correlated with cytoskeletal tensions[1]. So far polyacrylamide(PAA) gels have been the favored substrate for TFM and cell rigidity sensing studies[11] despite having numerous drawbacks not shared by PDMS. PDMS gels have a long and varied history of applications[12,13,14,15,16] and can be stored dry, do not swell significantly in aqueous solutions, and their chemical bonds do not undergo hydrolysis. Silicone gels on the other hand offer numerous advantages since they can be micropatterned[14,16], they have higher refractive indices than PAA gels[17], and are easy to prepare.

For any experiment involving TFM or cell rigidity sensing it's desirable to acquire the most accurate measurement of the substrate elastic modulus possible. There are many ways to measure the bulk elastic modulus of a gel including mechanical stretching, with simple weights[11, 18] or with a specialized device[16,19], rheometers[20], and indentations produced by beads[21] or specialized microindenters[22,23]. All of these techniques have caveats however. It can be difficult with stretch tests to ensure uniformity and achieve accurate cross sectional measurements, as well as dealing with softer formulations of PDMS which can be sticky and difficult to maintain a good grip on without ripping. Rheometer measurements can have difficulty maintaining a uniform contact area and preventing slippage. Lastly, indentation measurements can be difficult to calibrate and require some mathematical modeling that may not be intuitive.

Techniques for measuring the elastic modulus of thin gel layers include microfluidics[24] and pipette aspiration[25,26], but the most common technique has been using atomic force microscopy(AFM)[19,27,28,29]. While reliable and accurate, measurements with AFM are

impractical to do routinely due to their high cost and maintenance requirements, and the preparation necessary for a quality measurement. Good AFM measurements of elastic modulus require many considerations for accurate results such as accurate knowledge of the size of special spherical tips (possibly measured by SEM)[19,30,31], careful calibration of optics, trigger force, and spring constants, the depth of indentation in the gel, minimization of thermal drift[31], and determination of contact points and any adhesion of the probe to the gel[32]. Then the data must be fit using a Hertz or Sneddon model to obtain a result for the elastic modulus of the gel[19].

It's well known that different PAA gels with the same formulation can have fairly significant batch to batch variability in terms of their elastic moduli. These differences can be the result of reaction conditions, hydrolysis, or reagent variability. For this reason it would be ideal to have a fast and simple method of measurement rather than rely on the many previously published tables of elastic moduli values[11,23 ,29 ,33, 34, 35]. Silicone gels have been used somewhat less often possibly due to the lack of literature and the general difficulty of measuring an elastic modulus no matter what material is used.

Here we present a novel device for measuring bulk elastic modulus that is both simple and accurate. Samples are prepared in cuvettes that are fixed to the end of an arm that is rotated by a stepper motor resulting in a known body force applied radially outward. The shear stress results in a strain that is measured by the tracking of gold particles on the gel's surface. We apply the technique to samples of different hardness and different thickness made from Sylgard 184 and track their evolution over time. Additionally we show that the device can be used for dynamic measurements by imaging the shear strain of the gel evolving in real time. To validate the measurements we compare results with a conventional stretch test and also a microfluidic shear test.

Methods:

Theory of operation and practical considerations

The basic idea of the proposed rheometry technique is to place a flat-parallel layer of gel on a horizontal rotating platform and to monitor the deformation of the gel under the centrifugal force with a microscope, by measuring radial displacements of tracer particles on the free top surface of the gel (Fig. 3-1). When both the lateral dimensions gel layer and the distance from the axis of rotation are much larger than the thickness of the layer, the deformation is expected to be pure shear and, hence, inversely proportional to the shear modulus of the gel, G. The local shear, γ, is expected to be proportional to the local centrifugal force per unit volume, $f = \rho\omega^2 r$, where ρ is the density of the gel, ω is the angular velocity of rotation, and r is the distance from the point of interest to the axis of rotation.

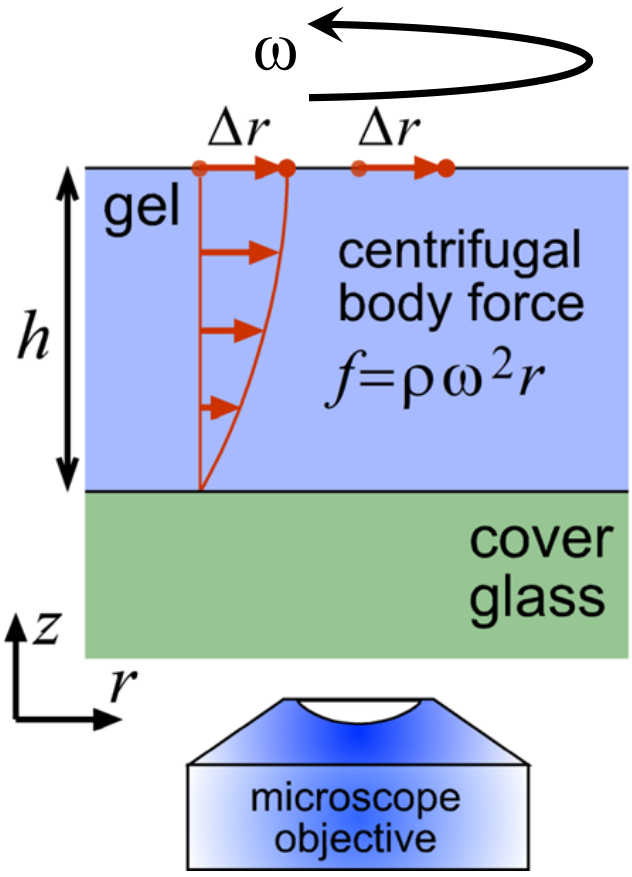

Figure 3-1: Schematic of the centrifuge rheometer.
A slab of transparent gel with thickness *h* on a cover glass is placed on a platform rotating at an angular velocity ω, resulting in a centrifugal force per unit volume of $f = \rho\omega^2 r$, where ρ is the density of the gel. Because the bottom surface of the gel is attached to a rigid substrate (cover glass), while the top surface is free, the displacement of the gel, u, under centrifugal force is a parabolic function of the vertical (z-axis) position. The displacement of tracer particles on the top surface of the gel, u_0, is measured at radius *r* under microscope as a function of ω and used to calculate the mean shear $\bar{\gamma} = u_0 / h$. The mean shear stress is calculated as $\bar{\tau} = \rho h^2 \omega^2 r / 2$ and used to compute the shear modulus of the gel $G = \bar{\tau} / \bar{\gamma}$.

If we adopt a cylindrical reference frame, with the vertical axis of rotation along the z-axis, only consider gel displacements, u, along the radial direction and assume that u only varies along the z-axis (which is the direction across the layer, thus neglecting the slower variation of u along the radius) shear stress in the gel can be calculated as

$$\tau_{rz} = G\gamma_{rz} = G\frac{\partial u}{\partial z} \tag{3-1}$$

The condition for mechanical equilibrium with the centrifugal force, f, is then

$$f + \frac{\partial \tau_{rz}}{\partial z} = 0 \tag{3-2}$$

Substituting leads to

$$\rho\omega^2 r + G\frac{\partial^2 u}{\partial z^2} = 0 \tag{3-3}$$

And finally the differential equation for the displacement, u, is

$$\frac{\partial^2 u}{\partial z^2} = -\frac{\rho\omega^2 r}{G} \tag{3-4}$$

For a gel layer with a thickness h, the bottom surface at $z = 0$ and the top surface at $z = h$, zero displacement at the bottom (no-slip boundary), and zero stress at the top (free top surface), we zero we have boundary conditions $u = 0$ at $z = 0$ and $\tau_{rz} = 0$ at $z = h$, translating into $\frac{\partial u}{\partial z} = 0$ at $z = h$. The solution of eq. 3-4 that satisfies these boundary conditions is

$$u = \frac{\rho h^2 \omega^2 r}{2G}[1 - (z/h)^2] \tag{3-5}$$

The radial displacement at the top surface, which is measured with tracer particles, is then given by

$$u_0 = \frac{\rho h^2 \omega^2 r}{2G} \tag{3-6}$$

We further note that the shear stress τ_{rz} varies across the thickness of the layer from 0 at the top to $\rho h\omega^2 r$ at the bottom and has a mean value

$$\bar{\tau} = \rho h\omega^2 r/2 \qquad 3\text{-}7$$

which is one half of the maximum. The shear, γ_{rz}, varies across the layer from 0 at the top to $2u_0 / h$ at the bottom and has a mean value of

$$\bar{\gamma} = u_0/h \qquad 3\text{-}8$$

(which is also one half of the maximum shear). Hence, shear modulus can be simply expressed in terms of the mean stress and mean shear as

$$G = \frac{\bar{\tau}}{\bar{\gamma}} \qquad 3\text{-}9$$

For soft silicone gels, the Poisson ratio, ν, is close to 0.5, such that the equation connecting the shear modulus and elastic modulus, $E = 2G(1+\nu)$, becomes$E \approx 3G$, resulting in

$$E \approx \frac{3\bar{\tau}}{\bar{\gamma}} = \frac{3\rho h^2\omega^2 r}{2u_0} \qquad 3\text{-}10$$

One can generally expect eq. 3-5 to work well for $r \gg h$ and for internal regions of a gel layer, with a distance to the nearest edge also much greater than h. In practice, lateral dimensions of the gel sample are always limited, large r leads to a large moment of inertia for the rotating platform, making it difficult to both accelerate and accurately balance it, whereas small h leads to small displacements of the tracer particles (eq. 3-5), making it difficult to measure them accurately. The intended use of the rheometer was to measure the elastic moduli of silicone gels with rigidity in a physiological range of soft tissues, $E < 100$ kPa ($G < 33$ kPa).

Because of practical considerations (keeping the size of the setup and the magnitude of the angular momentum of the rotating platform reasonably small), we chose $r = 50$ mm and wanted to operate the setup at <10 rotations per second (rps), corresponding to $\omega < \omega_{max} = 62.8$ s^{-1}. For a gel layer with ρ = 1040 kg/m^3 (typical density of silicone gels), $E = 100$ kPa ($G = 33.3$ kPa), and $h = 2.0$ mm, the maximal displacement is then $u_{0,max} = \frac{\rho h^2 \omega_{max}^2 r}{2G} =$ 12.5 μm. Such displacement of a tracer particle is readily measurable even under a moderate-resolution microscope (0.5 μm precision in the center-to-center distance, corresponding to an ~4% fractional error), assuming that the rotation of the platform does not introduce a substantial error.

To check, whether eq. 5 provides sufficiently good approximation for gel samples to be experimentally tested (given the simplifying assumptions used in the derivation of eq. 3-5), we used Comsol to perform numerical simulations of flat-parallel slabs of gel with different lateral dimensions and boundary conditions on the side. The simulations indicated that for a rectangular slab with $h = 2.0$ mm, $x \times y$ dimensions of 30×20 mm, and the center at $x =$ 50 mm and $y =$ 0, the displacement, u_0, in the middle of the slab is within 1% of u_0 predicted by eq. 5 regardless of the boundary conditions on the sides of the slab (Fig. 3-2). Specifically, for ρ = 1040 kg/m^3, $E = 10$ kPa, and $\omega = 10$ s^{-1}, eq. 3-5 predicts $u_0 = 3.00$ μm, whereas the simulation indicates u_0 = 2.97 μm for zero displacement on the vertical faces of the slab (edges) and $u_0 = 3.00$ μm for free vertical faces. Hence, one can expect that non-uniformity of gel thickness near the edges (due to menisci, etc.) would have minimal effect upon u_0 at the center. In addition, the simulation (Fig. 3-2B) indicated that u_0 remains 1% of its value at the center for *x*-axis position (radial coordinate) varying by ±0.5 mm and *y*-axis position varying by ±4 mm. In other words, the simulation indicated that $\bar{\gamma}$ at the center of the slab (the intended point of measurement) can be

evaluated with a small error from measurements of u_0 in a relatively large area around the center. Numerical simulations (not shown) also indicated that the agreement between eq. 3-5 and numerical results is further improved, if the $x \times y$ dimensions of the slab are increased or if the layer thickness is reduced. On the other hand, the difference between eq. 3-5 and numerical results becomes greater if the thickness of the slab is increased or its lateral dimensions are reduced. For example, when the size of the slab is reduced 15×10 mm, the simulations show a reduction of u_0 in the middle by as much as ~16% as compared with eq. 5. Therefore, for our experiments, we chose to prepare flat-parallel gel slabs in 30×20 mm cuvettes with $h \leq 2.0$ mm (and place the cuvettes on the rotating platform in such a way that the center of the slab is at $x =$ 50 mm and $y = 0$).

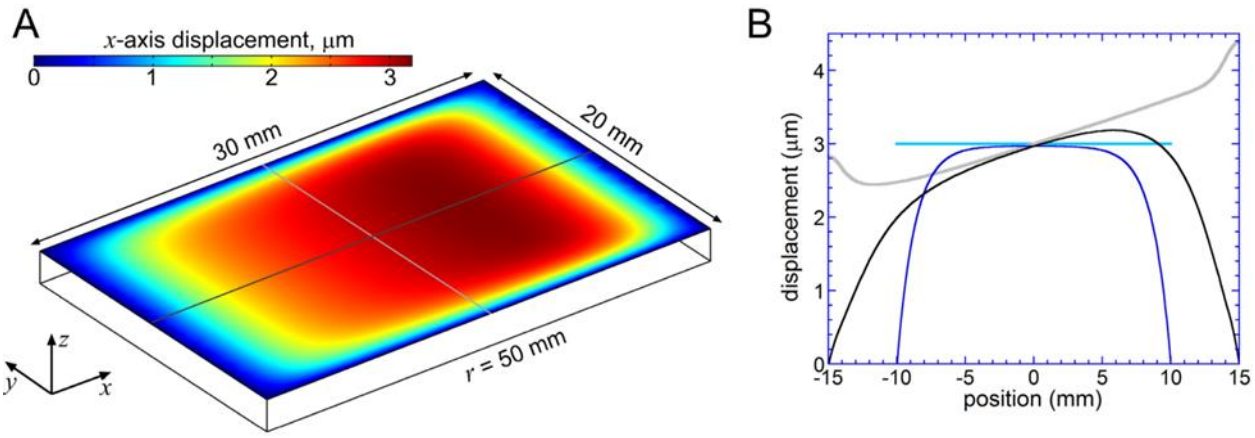

Figure 3-2: Numerical simulations of deformations of a horizontal slab of gel on a rotating platform.
The slab is 2 mm thick, 30x20 mm ($x \times y$ dimensions), with the center at $x =$ 50 mm and $y =$ 0. The elastic modulus of the gel is E = 10 kPa, the Poisson ratio is ν = 0.499, and density is ρ = 1000 kg/m^3. The rotation is around the vertical z-axis at ω = 10 s^{-1} (~1.6 rps), resulting in f = 5000 N/m^3 body force per unit volume in the middle of the slab. The bottom surface of the slab is completely constrained, whereas the top surface is free. (A) Drawing of the slab with a color-coded map of radial displacement of its top surface, u_0, when all vertical faces (edges) are completely constrained. (B) Displacement of the top surface, u_0, along different lines in panel A at different conditions. *Black curve*: displacement along the dark grey line parallel to the *x*-axis; *dark blue curve*: displacement along the light grey line parallel to the *y*-axis; *grey curve*: displacement along the dark grey line parallel to the *x*-axis in the case when all vertical faces of the slab are free rather than constrained (simulation not shown); *light blue curve*: displacement along the light grey line parallel to the *y*-axis in the case when all vertical faces are free rather than constrained (simulation not shown). For all four curves, the abscissa of 0 corresponds to $x =$ 50 mm and $y =$ 0. The theoretically predicted displacement (eq. 3-5) at $x =$ 50 mm and $y =$ 0 is $u_0 = 3.00$ μm.

Experiment setup and procedure

Flat-parallel gel slabs are prepared by pouring silicone gel pre-polymers into 30x20 mm, 2 mm deep cuvettes and letting gels cross-link. A cuvette is formed by gluing a 40x24 mm #1.5 cover glass to the bottom of a 50x25 mm plastic slide, with a 30x20 mm window that is laser-cut from 2 mm (0.08") thick acrylic sheet. The slide also has two 3 mm holes to fasten it to the rotating platform. Tracer particles are 1.6 μm gold beads (Seashell Technologies, San Diego), providing efficient scattering of light at relatively small diameter. A droplet of bead suspension

is deposited on the cover glass near the center of the cuvette and allowed to dry before the gel pre-polymer is poured. Another droplet of the bead suspension is deposited at the top of the gel after the gel solidifies. This way, both the bottom and top surfaces of the gel have tracer particles to monitor their displacement, u, under the centrifugal force.

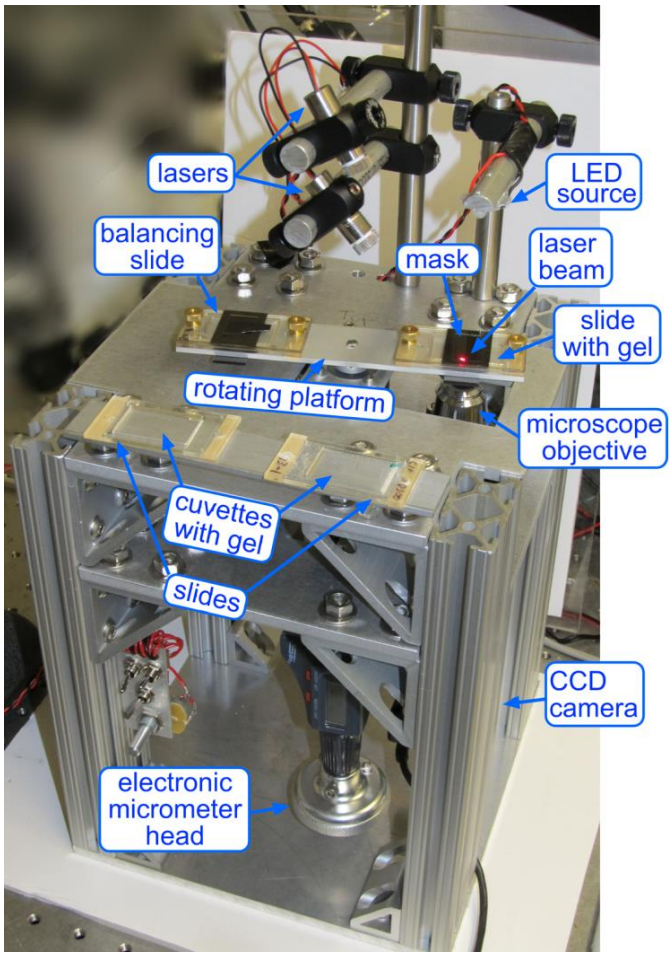

Figure 3-3: The centrifuge rheometer.
Image of the centrifuge rheometer with all parts labeled. The rotating platform spins forcing gel in cuvettes outward. Gold beads on the top and bottom surface of the gel scatter light down into the objective. Masks with narrow slits are used to cover the samples to reduce background scatter significantly. The elastic modulus of the gel is determined by measuring the displacement of the gel in conjunction with the known values for the rotation rate of the platform, and the thickness of the gel sample which is measured by using the micrometer mounted objective to focus on the gold beads at the top and bottom of the sample.

The rotating platform is machined of aluminum, is an axisymmetric 150×30 mm in size, 2.5 mm thick rectangle with two Ø8 mm openings at r = 50 mm from the center to enable the imaging of the tracer particles and two symmetric pairs of screws to fasten two slides with gel using thumb nuts. One slide has the gel sample to be tested, and the other slide is attached to balance the rotating platform (minimizing the bending and wobbling of the motor axle during high-speed rotation). Both slides are covered with opaque masks. The mask on top of the test slide has an ~100 μm wide transparent slit, which is aligned radially, along the axis of symmetry of the cuvette in the slide (Fig. 3-3). The platform is directly attached to the axel of a low-inductance NEMA 17 stepper motor (4018m-05, Lin Engineering, CA) to enable fast rotation with precise control of the speed. The motor is powered by a microstepping driver (Panther LE2 by IMS technologies), which is controlled with a home-made MatLab program. The motor is mounted on a custom-built darkfield microscope. The microscope is 10" tall, has a footprint of 8×8", and its frame is made out of waterjet-cut aluminum plates and 80/20 extrusions and corner gussets.

The imaging is performed from below with a 10x/0.25, 160 mm, long-working-distance (~9 mm; LWD) Nikon microscope objective. The objective is directly coupled through a hollow blackened aluminum tube to a digital USB camera (monochrome Chameleon by PointGrey) with a 1296×964 pixels CCD sensor, forming a video-microscope with an ~0.44x0.33 mm field of view, 0.34 μm pixelate resolution, and ~1.3 μm optical resolution for a wavelength of 650 nm. The tube is fastened to a vertical linear stage (Newport 423) equipped with a manual electronic micrometer head (Fowler 54-220-777-1), making it possible to adjust and measure the vertical (z-axis) position of the objective with an ~2 μm precision. The center of the field of view of the

video-microscope is at the distance r = 50.0 mm from the axle of the motor (under the centers of the Ø8 mm openings in the platform).

To measure the thickness of the gel in the cuvette, h, the rotating platform is brought to a position where the transparent slit in the mask is aligned with the field of view of the video microscope. The slit is then illuminated from above with an 650 nm (red) light emitting diode (LED) source (Fig. 3-3) and the micrometer head is adjusted, first, to focus the video microscope on 1.6 μm beads on the surface of the cover glass, and then on 1.6 μm beads on the surface of the gel. The difference between the readings of the micrometer at the two z-axis positions is the stroke of the vertical stage between the bottom and the top of the gel, Δz, which is multiplied by a correction factor, α, to calculate the thickness of the gel layer, $h = \alpha \Delta z$. The correction factor is estimated based on the refractive index of a common formulation of silicone (Sylgard 184 by Dow Corning) at 650 nm, $n \approx 1.42$, and the average angle of light collection for the 10x/0.25 objective in air, $\theta_{air} =$ 10.2°. The corresponding angle in the silicone is then found from Snell's law as $\theta_{sil} = \sin^{-1}[\sin(\theta_{air})/n] \approx$ 7.15°, and the correction factor is calculated as the ratio of tangents of the two angles, $\alpha = \tan(\theta_{air})/\tan(\theta_{sil}) \approx 1.43$.

When the platform rotates, the tracking of radial positions of gold beads is performed by taking long-exposure micrographs under darkfield illumination. The illumination is provided by a 10 mW, 650 nm semiconductor laser, with the laser beam directed at an angle of 30 - 45° to the vertical. The laser beam crosses the optical axis of the video-microscope at the plane of one of the surfaces of the gel and is loosely focused at this plane (Fig. 3-3). Because the angle of incidence the laser beam is always substantially larger than the ~15° angular aperture of the objective, no direct laser light is incident upon the front lens of the objective. Therefore, the images taken by the microscope remain completely dark as long as there is no scattering of light

along the laser beam and there is no ambient light in the room. On the other hand, a moving light-scattering gold bead, which is in the field of view and in the image plane of the microscope and which is illuminated by the laser beam, produces a sharp bright streakline in the image taken by the microscope. The high-intensity illumination with the laser beam is essential, because the circumference of the circle, along which the gold particles are moving (r = 50.0 mm), is 314 mm, which is ~2×10^5 times greater than the diameter of the gold beads. Hence, the brightness of the streaklines is equivalent to the brightness of still images of the beads taken with ~2×10^5 shorter exposure time (5 μs for 1 sec).

When the laser beam is incident upon the rotating platform, it is completely blocked by either the platform itself or the opaque masks on top of the cuvettes at all times other than the short interval when the ~100 μm wide transparent slit on the mask above the gel passes through the beam. It is during this short interval, when the laser beam illuminates beads on the gel surface that are directly under the slit and when streaklines are registered by the CCD camera (Fig. 3-4A). To make sure that bead streaklines are properly captured, the exposure time is set to be equal to at least one period of rotation of the platform. (The exposure time is usually set to be equal to a whole number of the periods of rotation.) Scattered light from a bead is registered by the camera, as long as the bead remains within the field of view and the slit remains exposed to the laser beam. The length of the streaklines is thus limited by both the width of the slit and the width of the laser beam along the azimuthal direction (typically ~200 μm at the gel surface). The width of the slit also defines the width of the region of the gel surface that is exposed to the laser beam. Hence, at a given bead density on the gel surface, the number of streaklines is proportional to the width of the slit. The number of streaklines is also proportional to the density of beads on the gel surface and the radial extension of the field of view of the video microscope (~0.48 mm).

The setup has a second laser (Fig. 3-3), with the beam loosely focused at the plane of the top surface of the cover glass (bottom surface of the gel) and crossing that plane in middle of the field of view of the video-microscope, when it passes through a layer of gel in the cuvette. This laser makes it possible to capture streak lines produced by 1.6 μm gold beads on the surface of the cover glass. Ideally, the pattern of these streaklines should remain unchanged as the angular velocity of the rotation of the platform, ω, is varied. In practice, however one may expect some changes with ω, including some displacement of the pattern in the radial direction, u'. The displacement u' can be real, resulting from some imbalance of the platform or residual deformability of the plastic slide. This type of displacement is expected to be proportional to the centrifugal force and, hence, to ω^2 and can be considered a systematic error and corrected for by subtracting the values of u' from the displacements of the top of the gel, u_0. Alternatively, u' can be a measurement artifact, resulting from blurring of the streaklines at high rotation rates or the movement of the top surface of the glass along the z-axis and the necessity to refocus the microscope. The values of u' that are due to measurement errors can be used to estimate the uncertainty of measurements of u_0.

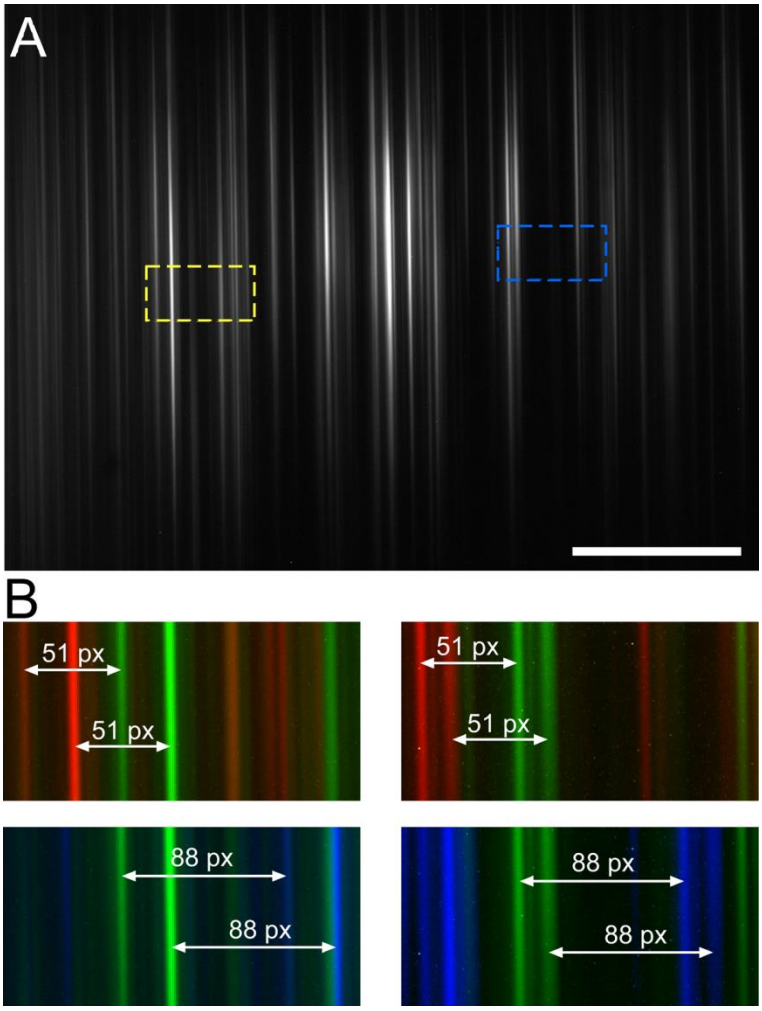

Figure 3-4: Displacements of the top surface of silicone gel caused by centrifugal force visualized with streaklines of the tracer beads under darkfield illumination.
(A) Micrograph of the gel surface taken at $\omega_1 = 6.28\ s^{-1}$. The field of view is ~4.4x3.3 mm along the radial (horizontal) and azimuthal (vertical) directions, respectively. Scale bar 100 µm. (B) Superimposed images of the region in the dashed yellow box (images on the left) and blue box (images on the right) in panel A taken at different angular velocities with the streaklines false-colored in red, green, and blue for $\omega_1 = 6.28\ s^{-1}$, $\omega_2 = 12.56\ s^{-1}$, and $\omega_3 = 18.85\ s^{-1}$, respectively. The upper row shows superposition of streaklines at $\omega_1 = 6.28\ s^{-1}$ and $\omega_2 = 12.56\ s^{-1}$. One observes that the entire pattern of streaklines is shifted to the right (radially outwards) by 51 pixels (17.2 µm) between the two angular velocities. The lower row shows superposition of streaklines at $\omega_2 = 12.56\ s^{-1}$ and $\omega_3 = 18.85\ s^{-1}$. The entire pattern of streaklines is shifted by 88 pixels (29.7 µm) between the two angular velocities.

Tests of feasibility and functionality

To test the functionality of the proposed centrifuge microscope, we performed measurements on several samples of silicone gels that were prepared by mixing different proportions of the Base and Curing agent (B and C) components of Sylgard 184 (Dow Corning) silicone. Whereas Sylgard 184 is normally used to make silicone elastomers (with $E \approx 2$ MPa after curing) by mixing B and C at 10:1, it has been shown to form solid silicone gels with E as low 0.5 kPa when B and C are mixed at higher ratios up to 78:1. Importantly, Sylgard 184-derived silicone gels were used as soft substrates for live cell cultures in multiple biological studies, and the dependence of E on the B/C ratio for these gels has been characterized by several groups using different techniques.

First, we tested, whether the streakline patterns produced by gold beads are sufficiently bright and sharp for the technique to work as intended. A test of a gel with B/C = 70 (that was cured overnight in an 80 °C oven) at rotation rates up to 5 rps showed bright and sharp streaklines (Fig. 3-4A). All rotation rates were whole numbers of rps, and the exposure time was always set at 1 sec. Therefore, in an image taken at N rps, a single streakline is, in fact, a superposition of N streaklines produced by N consecutive passages of a single bead through the laser beam. Importantly, whereas the widths of streaklines are as large as 6 pixels (~2.0 μm; FWHH), the positions of their centers along the radial (r) direction can be readily found with a precision of a single pixel (~0.34 μm), even at high rotation rates. In addition to certainly being a positive outcome, this stability of the radial positions of the beads is somewhat surprising, because the rotating platform is directly attached to the axle of an inexpensive commercial stepping motor, and the beads are at a large distance from the axis of rotation.

Second, we tested, whether gel thickness can be reliably measured by focusing the microscope at beads at the top and bottom of the gel layer. According to the reading of the digital micrometer in repeated tests, the position of the sharpest focus was found with a precision of ±3 μm, suggesting an measurement uncertainty for the thickness of the gel $\delta h \approx$~6 μm (taking into account the correction factor $\alpha = 1.43$ in $h = \alpha \Delta z$). The thickness was $h \approx 1.94$ mm, corresponding to a relative error $\delta h / h \approx 0.3\%$. It is worth noting, however, that unlike u_0, h appears in eq. 3-10 in square. Therefore, the contribution of the uncertainly in h in the uncertainly of the calculated value of E becomes comparable to the contribution of a 3% uncertainly in u_0, if h is reduced to ~0.4 mm.

Third, we tested whether the dependence of u_0, as measured by the displacements of beads, on ω sample follows eq. 3-6, $u_0 \propto \omega^2$, and whether the value of E found for this gel by plugging this dependence into eq. 3-10 is consistent with what was previously reported for Sylgard 184-based gels. Because the radial positions of beads are measured by capturing their streaklines when the platform is rotating it is very difficult to obtain their positions at $\omega = 0$. Therefore, we took photographs of streaklines at rotation rates of 1, 2, and 3 rps, corresponding to $\omega_1 = 6.28\,\mathrm{s}^{-1}$, $\omega_2 = 12.56\,\mathrm{s}^{-1}$, and $\omega_3 = 18.65\,\mathrm{s}^{-1}$ and measured the differences in the radial positions of streaklines produced by individual beads between the 2nd and 1st and between the 3rd and 2nd image (Fig. 3-4B). The streaklines were selected for being bright and easily identifiable in all photographs (e.g. by being a part of a readily distinguishable pattern of streaklines). We found that the distances between radial positions in the 2nd and 1st image to be consistently at 51 pixels, corresponding to a displacement $u_{0,12} = 17.2$ μm (Fig. 3-4B), and the distances between radial positions in the 3rd and 2nd image to be consistently at 88 pixels, corresponding to $u_{0,23}$ =

29.7 μm (Fig. 3-4). The experimentally found ratio is $\frac{u_{0,12}}{u_{0,23}} = \frac{51}{88} = 0.58$ is within 3.5% of the ratio predicted by Eq. 3-6, $\frac{u_{0,23}}{u_{0,12}} = \frac{\omega_2^2 - \omega_1^2}{\omega_3^2 - \omega_2^2} = \frac{2^2 - 1^2}{3^2 - 2^2} = \frac{3}{5} = 0.60$.

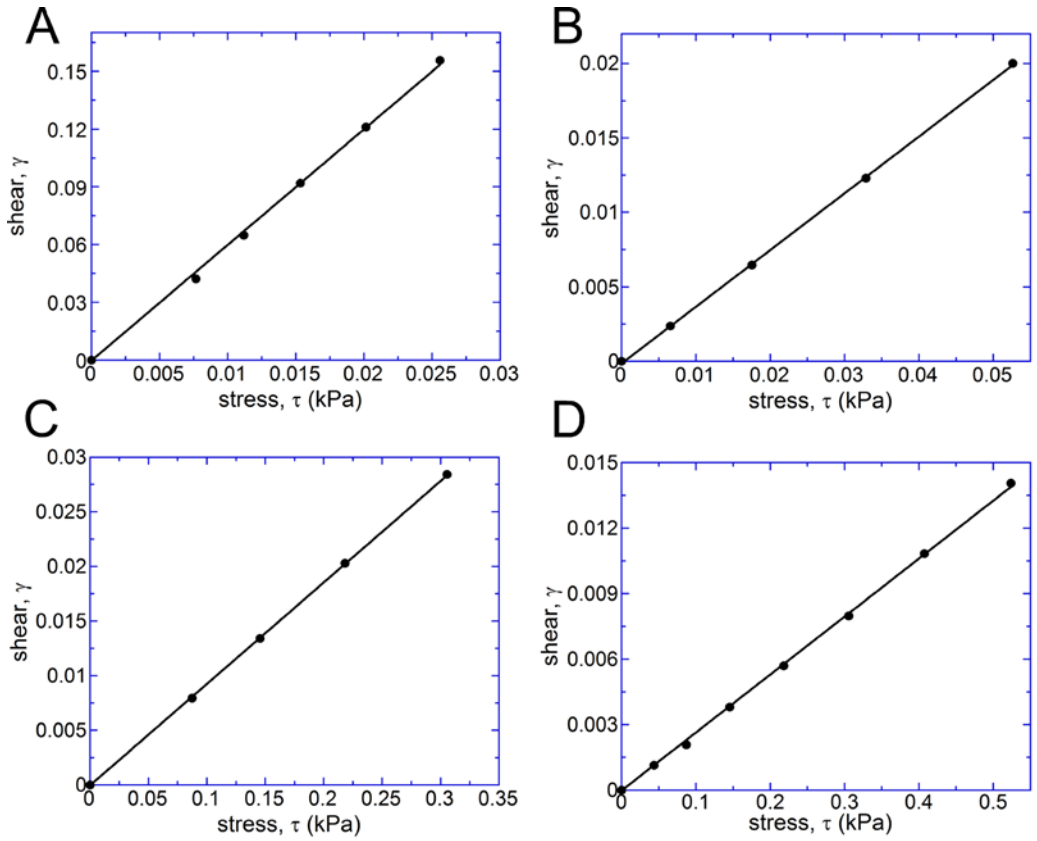

Figure 3-5: Mechanical tests of Sylgard 184 gels with various B/C ratios using the centrifuge rheometer.
Thickness of gel layer, h, in the cuvette was measured. The angular velocity of the platform, ω, was varied and values of displacement at the top surface of the gel, u_0, were calculated by measuring the radial displacements of the streakline patterns as compared with a reference streakline pattern at a low angular velocity, ω_{ref}(cf. Fig. 3-4). Shear, $\gamma = u_0/h$, is plotted against shear stress, which is calculated as $\tau = hr\rho\left(\omega^2 - \omega_{ref}^2\right)/2$. Data are fitted by straight lines passing through the origins (black lines). The B/C ratios, gel thicknesses, h, and elastic moduli, E (which are calculated from the slopes of the best fits as $E = 3\tau/\gamma$), are respectively: (A) 75:1, 0.31 mm, and 0.48 kPa; (B) 60:1, 2.14 mm, and 7.9 kPa; (C) 45:1, 1.91 mm, and 32 kPa; (D) 33:1, 1.77 mm, and 111 kPa.

It is worth noting that the 3.5% discrepancy between the two differential displacements would be expected for random errors of as small as 1.5 pixels (~0.5 μm) in the measurements of each of $u_{0,12}$ and $u_{0,23}$. It is also worth noting that the apparent precision of 3.5% is achieved at very small deformations of the gel, with the maximal shear estimated as $\bar{\gamma} = \frac{u_{0,3}}{h} = \frac{0.0535\,\text{mm}}{1.94\,\text{mm}} = 0.028$. Finally, the elastic modulus of the gel is calculated as $E = \frac{3\rho h^2(\omega_3^2 - \omega_1^2)r}{2(u_{0,12} + u_{0,13})} \approx 2.0$ kPa, which is in line with elastic moduli reported before for Sylgard 184-based gels with similar mixing ratios, B/C (see also Fig. 3-6 below).

As the final test of functionality, we the rheometer to measure the elastic moduli of a number of gel samples with B/C from 75:1 to 33:1, which were expected to have a broad range of E (Fig. 3-5). For each gel, we first took a reference photograph of streaklines at some low rotation rate, typically 0.25 – 1.0 rps, corresponding to ω_{ref} = 1.57 – 6.28 s^{-1}, which was expected to result in a minimal deformation of the gel. (The values of ω_{ref} were chosen smaller for more easily deformable gel samples.) The angular velocity, ω, was then varied, and displacement, u_0, was measured at each ω with respect to that reference photograph (rather than with respect to non-deformed gel, because it would be difficult to obtain positions of tracer particles, when the platform is motionless). The values of $\gamma = u_0 / h$ were plotted against mean stress at the same conditions with a correction for the shear stress at ω_{ref}, $\tau = \rho h(\omega^2 - \omega_{ref}^2)r/2$. (For the sake of convenience, from this point on, we drop the average value bars from above of both τ and γ.) The elastic modulus of the gel was calculated from the slope of the linear fit to the dependence of γ on τ, as $E = \frac{3\tau}{\gamma}$ (eq. 3-10).

The values of r and ρ remained unchanged and were precisely known for all gels, and the angular velocities were always set with a high precision using the stepper motor driver. Except for the softest gel with B/C = 75:1, all samples had gel layers with h ~ 2 mm, resulting in very small contributions of the uncertainty of h, $\delta h / h$, into the uncertainty of E. (The thickness of the gel sample with B/C = 75:1 was $h = 0.31$ mm to make the sample deform less at small rotation rates, resulting in ~4% contribution from $\delta h / h$ into the uncertainty of E). Hence, the main source of random error in E was the uncertainty in the measurement of u_0 that resulted from mechanical imperfections, vibrations, and limited robustness of the rotating platform and to a lesser extent from relatively large widths of the streaklines (Fig. 3-4B). A manifestation of these mechanical imperfections were some changes in the z-axis position of the surface of the gel at different ω that likely resulted from vibrations and residual vertical motion of the motor axel and that necessitated some refocusing of the microscope, as ω was modified. To obtain an estimate for the uncertainly of u_0, we took photographs of streaklines by beads at the gel-cover glass interface and measured their radial displacements, u', at various ω (again, with respect to the reference radial position of the streaklines at ω_{ref}). The dependence of u' on $\omega^2 - \omega_{ref}^2$ was always weak as compared to the dependence of u_0 on $\omega^2 - \omega_{ref}^2$, corresponding to relatively small systematic errors in u_0. On the other hand, there were random variations in u' on the order of 1-2 pixels, and one could expect random variations in u_0 on the same order or greater (because the layer of soft gel may be susceptible to additional uncontrolled mechanical effects). To reduce the effect of absolute uncertainties in u_0 upon the uncertainty in E, we always attempted achieving sufficiently large absolute values of u_0 by using higher maximal ω for harder gels. For, example, for the gel with B/C=65:1, which was measured to have E = 7.9 kPa,

$u_0 = 43$ μm (127 pixels) was achieved at 5 rps, whereas for the gel with B/C = 33, which was measured to have E = 111 kPa, the maximal rotation rate was set 17 rps, that resulted in $u_0 = 24$ μm (72 pixels).

For all gel samples tested, the experimental data on γ vs. τ were well fitted with straight lines passing through the origin (Fig. 3-5). The values of E calculated from the slopes of the lines ranged from ~0.5 kPa for the gel with B/C = 75 (Fig. 3-5A) to >100 kPa for the gel with B/C = 33 (Fig. 3-5D), covering nearly the entire physiological range of rigidity of soft tissues (0.1 – 100 kPa). Therefore, the results of these tests provided further validation of the proposed rheometry technique and setup for characterization of silicone gels that can be used as soft substrates for cell cultures. Because the measurement errors were believed to be largely random (rather than systematic; and because the contribution from $\delta h / h$ was usually small), we considered the uncertainty of the slope of the fitting line as a reasonable estimate of the experimental uncertainty of E. Based on the uncertainty of the slope, experimental uncertainties of E were always below 5%.

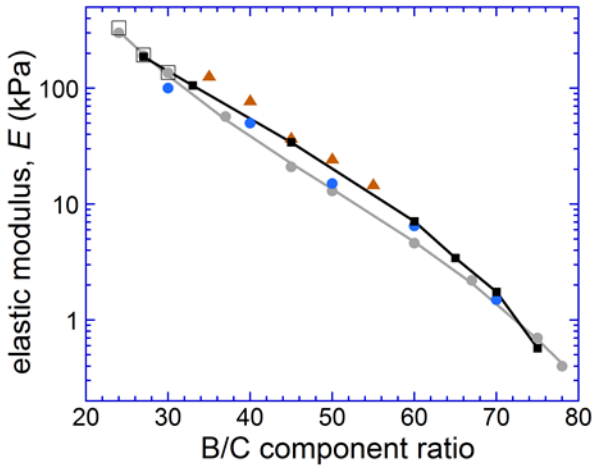

Figure 3-6: Elastic moduli, *E*, of Sylgard 184-based silicone gels with different ratios of B and C components, as measured by several groups using different techniques.
Orange triangles (and black line): measurements of axial stress of cylindrical samples as a function of the applied axial extension, from Cesa et al.[16] Blue circles: measurements of axial stress of cylindrical samples as a function of the applied axial extension, from Schellenberg et al.[36] Open squares: measurements of extension as a function of longitudinal stress applied to a slab, from Gutierrez et al.[24] Grey circles (and grey line): measurements of shear strain of ~ 70 µm layer of gel as a function of hydrodynamic shear stress in a microfluidic setup, from Gutierrez et al.[24] Black squares (and connecting black line): measurements with the proposed rheometer.

We measured *E* for Sylgard-184 based gels with several other mixing ratios, B/C, (including a gel with B/C = 27:1, that had *E* = 187 kPa) and compared the dependence of *E* on B/C measured with the proposed technique with results reported by other groups that used different measurement techniques and with previous measurements by our own group using shear flow in a microfluidic device and uniaxial extension under load (Fig. 3-6). Given the expected batch-to-batch variability of Sylgard 184 (and the fact that Sylgard 184 is designed to produce elastomers rather than gels) and substantial discrepancies between the previously reported values of *E*, our results appeared to be largely consistent with these previous data.

Validation and Results:

To validate measurements we prepared samples in cuvettes for the centrifuge rheometer and also for a mechanical stretch test. The samples were baked for three weeks to make sure all samples were fully polymerized due to differences in thickness. Samples for the stretch test were baked on wafers with a 12μm grating. They were then suspended vertically and a laser was used to create a measurable diffraction pattern. The distance between maxima was recorded with and without a load of mass, *m* attached as ζ_f and ζ_i respectively. The load produced a tensile stress, $\sigma = \frac{mg}{A}$ with *A* the cross sectional area of the sample. With the strain, $\frac{\Delta y}{y}$ written as $\frac{\Delta y}{y} = \frac{\zeta_f - \zeta_i}{\zeta_i}$ we compute $E = \frac{\sigma}{\Delta y/_y} = \frac{mg\,\zeta_i}{A\,(\zeta_f - \zeta_i)}$.

Additionally, we compared measurements using the centrifuge scope to those made using a variation of our previous microfluidic device with just a single channel. The device is designed to produce maximal shear stress, τ, on a substrate in a small 2 x 2mm region from a given pressure difference, ΔP. By marking the substrate with red fluorescent 40nm beads we can measure the displacement, Δx, of the substrate produced by a given pressure input. The shear strain is $\gamma = \frac{\Delta x}{\xi}$, with ξ the thickness of the substrate. For silicone and PAA gels we can use the formula $E = 2(1 + \nu)G$ with $\nu = 0.5$ and the shear modulus, $G = \frac{\tau}{\gamma}$. Thus $E = 3\tau\frac{\xi}{\Delta x}$ with ξ and Δx easily obtained from the microscope. To find the shear stress we study the flow in the microfluidic channel and can obtain a simple linear relation with the pressure difference provided the flow remains laminar throughout the device and the dimensions do not change. We define the proportionality constant, k, as $k = \frac{\tau}{\Delta P}$. We are able to determine the shear stress and proportionality constant by analyzing streaklines in the device and finding the maximum flow

velocity. The flow in the test chamber is parabolic and goes as $v = v_{max}[1 - \frac{4\left(z-\frac{d}{2}\right)^2}{d^2}]$ implying the shear stress at the substrate is $\tau = \frac{4\eta v_{max}}{d}$. This allows us to compute E from readily evaluated variables as $E = 3k\Delta P \frac{\xi}{\Delta x}$.

PDMS layers of different thicknesses can have different elastic moduli and the centrifuge scope and microfluidic device are intended for different regimes of thickness. For these reasons we measured the evolution of elastic moduli for samples of different thicknesses over time with the centrifuge microscope to see them converge, and to ultimately compare with the measurements of the microfluidic device when they were fully cured. Two cuvettes each were prepared of four different thicknesses and baked in an 80 degree oven along with cover glasses spun coat from the same batch of 184 for three different ratios of pre-polymer.

To validate the measurements of the centrifuge rheometer we compared measurements of the elastic moduli of samples of Sylgard 184 at three different B/C component ratios, and thus three different elastic moduli, using three different techniques. First we compared centrifuge rheometer measurements with mechanical stretch testing measurements by making three cuvettes at each ratio, and baking the same premixture on a silicon wafer with a 12um grating. We then used a laser to illuminate the grating relief on the sample and create a diffraction pattern. By measuring the difference in distance between maxima with and without a load attached to the sample we were able to determine the strain the gel was under. Knowing the weight of the attached load allowed us to compute the stress and the elastic modulus of the gel. We compared three different formulations of Sylgard 184 and found good agreement (within 2%) with the centrifuge scope measurements. Specifically, we measured ratios of 47:1, 43:1, and 40:1 and measured elastic moduli of 35.5/36.2, 62.6/62.5, and 84.8/86.5 respectively, where the first

number is the average of three cuvettes measured and the second is the result of the mechanical stretch test. This suggests the technique is both effective and accurate.

Additionally, we compared the elastic moduli of samples using the centrifuge scope and our previously published microfluidic technique. We found gels take longer to reach their maximum elastic moduli the thicker the samples are. Plotted in Figure 3-7 are the elastic moduli of three different batches of Sylgard 184 at three different ratios: 75-1, 70-1, and 65-1. We found that the elastic moduli converged after significant bake time and agreed reasonably well with our microfluidic tests again reaffirming the effectiveness of the technique.

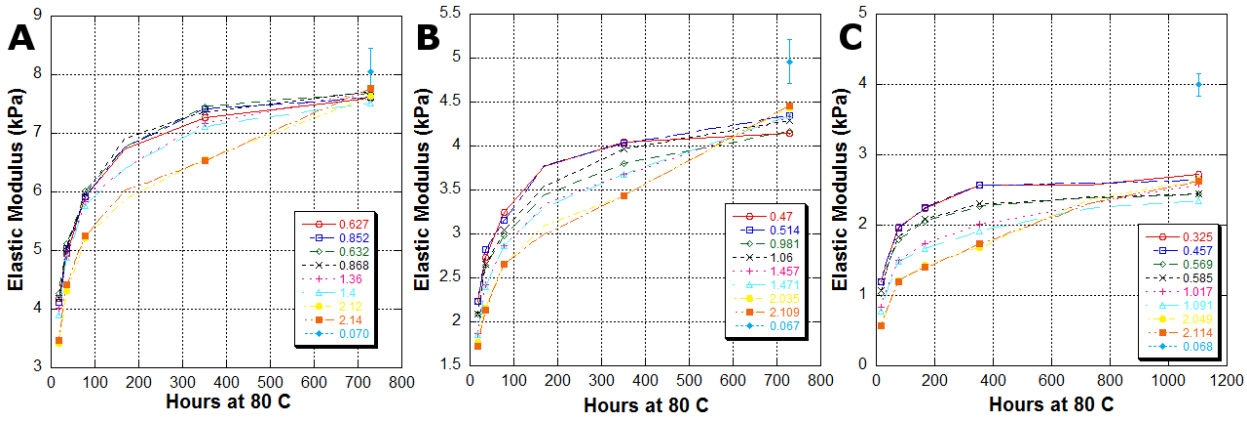

Figure 3-7: Comparison of centrifuge rheometer and microfluidic elastic modulus measurements.
Eight cuvette samples and one microfluidic sample were made for each pre-polymer ratio, left to right they are 65:1, 70:1, and 75:1. Legend lists thicknesses of samples in mm, with the microfluidic sample, the thinnest, shown in light blue. Each plot demonstrates the difference in elastic modulus for samples of different thickness, and shows that they ultimately converge after hundreds of hours of bake time. Harder samples show better agreement with the microfluidic test.

In addition to static measurements of displacement at a given shear stress the centrifuge microscope can also be used for dynamic measurements. By accelerating or decelerating the rotation speed and capturing images while the gel is moving we can estimate the relaxation time

of the gel. We estimate the characteristic time for the gel to displace as the time it takes the gel to reach 63% ($1 - e^{-1}$) of its maximum displacement for an applied shear.

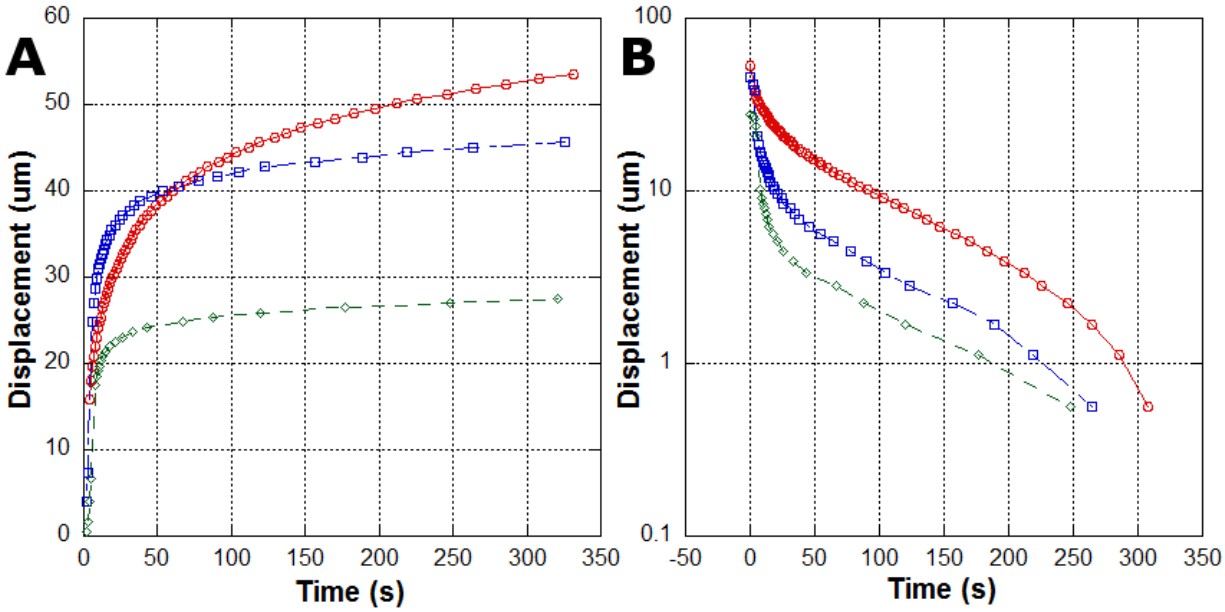

Figure 3-8: Dynamic plots of gel displacement.
A) The displacement as a function of time for an applied shear for three different cuvettes of the same Sylgard 184 sample measured after periods of baking resulting in the polymerizing of the gel. Here the red circles represent the sample when it has E=250Pa, blue squares for E=1.1kPa, and green diamonds for E=1.76kPa. As you would expect harder samples displace less and reach a larger fraction of their ultimate displacement more rapidly. B) The same process for the same samples in reverse, where we can see the gel relaxing from its full displacement back to its original position.

We note elastic moduli of silicone gels are usually measured at room temperature (RT). On the other hand, when gels are used as soft substrates for mammalian cell culture applications, they are normally maintained at ~37 °C. Therefore, it is the elastic moduli of gels at ~37 °C rather than RT that are most relevant for cell culture applications. To test temperature dependence of elastic moduli of silicone gels, we prepared five Sylgard 184-based gel samples with B/C from 30:1 to 67:1 (all ~2 mm thick) that had E from 118 to 1.37 kPa, as measured at RT (~22 °C). We then placed the entire rheometer in a specially built environmental enclosure

with forced convection of temperature-controlled air, and repeated the measurements of E at 37 °C. The ratios between values of E measured at the two temperatures, E_{37}/E_{RT}, varied between 0.95 and 1.07 for the gel samples we tested, with an average of 1.02 and SD of 5% (which is consistent with the estimated measurement error).

Discussion:

Our novel device has many advantages over other techniques of measuring elastic modulus such as AFM, stretch testing, or microfluidic testing. The microscope is relatively easy to build, and also quite cheap compared to its alternatives. This is in contrast to a device such as an AFM which is prohibitively expensive. For a lab looking to measure the elastic moduli of their own gels, this device proves the simplest, fastest and most suitable method.

AFMs are not only significantly more expensive but also have other caveats such as a difficult calibration process, and a potential to deform the gel beyond its linearly elastic regime. AFMs also rely on a non-linear function of gel thickness, elastic modulus, and radius of curvature of the probe tip to determine the expected depth of indentation for the probe. What's more these AFMs require specialized tips since the usual AFM configuration includes a sharp tip poorly suited to the task of indenting a very soft gel. There are also additional sources of error including difficulty in finding the exact point of contact for the probe and also variable loading conditions that could affect the measurement.

Unlike AFM measurements we are able to evaluate the elastic modulus of a gel using a very simple formula derived from basic mechanics $E = (2\pi)^2 f^2 \frac{3\rho r h^2}{2\Delta x}$. This simpler formula allows for a more intuitive understanding of how different parameters affect the measurement and allows for quick and easy estimates. Additionally measurements can be made with relatively

little error. For gels thicker than 300um and deformations larger than 20um we can determine E to within less than 5%. For gels as thick as 2mm and larger deformations our error can be reduced to below 1%.

Using the device we were able to measure a broad range of elastic moduli from 0.3-250kPa. The nature of the device allows us to reach almost arbitrarily low speeds to measure incredibly soft gels and probe the limit of what is a solid viscoelastic material. Although the current device has an upper limit in the 200-300kPa range, the technique can simply be scaled up to accommodate harder gels. The simplest improvements would be increasing the length of the rotating arm for a linear increase in the maximum measurable E, or a faster stepper motor for a quadratic increase.

An option to measure polyacrylamide gels was also explored. By polymerizing the gels in the cuvettes and then adding beads and water before sealing them, we could ensure the gels would stay hydrated by keeping them in a high humidity environment. Our limited testing produced widely varying results within a single batch (two orders of magnitude), possibly due to our own inexperience with these gels.

Silicon gels are a valuable alternative to hydrogels since they do not dry out and are relatively inert making them ideal for cell rigidity sensing studies and TFM studies. The gel surface can also be easily treated with ECM molecules for animal cells and has been shown to be effective by many groups. Beads can also be easily added to the surface of these gels to allow for easy tracking of the gel displacement without the worry that the beads are not in the correct plane because they have been added to the bulk of the gel as with many PAA experiments. Additionally these beads and coatings can be micropatterned, creating very specific configurations for ideal experimental conditions. Another advantage of silicone gels over PAA is

their high refractive index which allows them to be utilized in total internal reflection fluorescence(TIRF) microscopy. Their refractive indices ranging from 1.41 for Sylgard 184 to 1.49 for other silicone gels allow one to pinpoint where the cells are adhering to the substrate in addition to seeing the substrates displacement so that they can be correlated.

As far as temperature is concerned, the average difference of 2% between the elastic moduli of Sylgard 184-based silicone gels at RT and 37 °C is clearly too small to be of practical significance. Hence, our results indicate that the values of E measured at RT can be directly used for cell culture applications. The small increase in E with temperature may be a real effect related to the entropic elasticity of the network of cross-linked polymers in the gels, for which the elastic modulus is expected to be proportional to the absolute temperature, increasing by ~5% between 22 and 37 °C.

This study has shown that our centrifuge microscope is a simple, effective, and efficient method for evaluating the elastic modulus of gel samples. The device makes it possible to measure many samples very quickly and do large scale studies of the properties of silicone gels. Additionally samples can be stored and measured multiple times for an indefinite period of time. This would allow one to produce a large batch of substrates for cell experiments all at once, and be able to use them and measure their elastic moduli at any time and be confident of the result.

In summary we've developed a novel device that uses rotation to induce a shear stress for measuring the elastic moduli of soft gels that is fast, simple, and accurate. Our device is simple and cheap to build, can measure elastic moduli over the majority of the physiological range, and is capable of making measurements with minimal error. We have shown the device is consistent with other methods of measuring elastic moduli. We also used the device to track Sylgard 184 samples over a period of time and show that while they begin with large differences, they

eventually converge. Additionally we demonstrated the device can be used for dynamic measurements by showing the evolution of a particular sample's relaxation time as it polymerized. We believe this device can be instrumental in understanding the properties of soft gels and can be particularly useful for those labs doing rigidity sensing and cell traction force microscopy studies.

Chapter 3, in full, is in preparation for submission for publication as “A Novel Device for Measuring the Elastic Moduli of Soft Gels”, Ronan, Edward; and Groisman, Alex. The dissertation author is first author and a leading contributor to this paper.

4. Biological Impact of Substrate Rigidity

4.1. Rigidity of Silicone Substrates Controls Cell Spreading and Stem Cell Differentiation

Abstract:

The dependences of spreading and differentiation of stem cells plated on hydrogel and silicone gel substrates on the rigidity and porosity of the substrates have recently been a subject of some controversy. In experiments on human mesenchymal stem cells plated on soft, medium rigidity, and hard silicone gels we show that harder gels are more osteogenic, softer gels are more adipogenic, and cell spreading areas increase with the silicone gel substrate rigidity. The results of our study indicate that substrate rigidity induces some universal cellular responses independently of the porosity or topography of the substrate.

Introduction:

Multiple functions of cells cultured on flat substrates have been shown to depend on the elastic modulus of the substrate, E, with the dependence being strongest in a physiological range of soft tissues, corresponding to E from 0.1 to 100 kPa. Among those functions are stem cell differentiation, cell spreading, and cell signaling[1]. In the context of differentiation of mesenchymal stem cells (MSCs), substrates with E in the ranges of < 4 kPa, 8–17 kPa, and > 25 kPa, have been classified as soft (adipogenic)[2,3], medium rigidity (myogenic)[1], and hard (osteogenic)[1], respectively. In most studies, the soft substrates are hydrogels, and variations in their elastic moduli are usually accompanied by variations in the dry mass and porosity. The paradigm of the effect of substrate rigidity on the cellular functions was challenged by

Trappmann et al.[4], who claimed that cell spreading and differentiation on polyacrylamide (PAAm) hydrogel substrates depend not on the elastic moduli of the substrates, but rather on their porosity. The size of the pores in the PAAm substrates changed from 1 μm for soft gels to 0.1 μm for hard gels, affecting the density of adhesion points between the substrate surface and the extracellular matrix (ECM) coating on it[4]. This claim was rebutted by *Wen at al.*[3], who used hydrogel substrates with different porosities but identical elastic moduli to show that it is the elastic modulus rather than the porosity that is key to the effect of the substrate on cell spreading and differentiation. Both publications agreed, however, that there was no appreciable effect of the substrate rigidity on either cell spreading or differentiation, if the substrate was made of a silicone gel. (Silicone materials normally do not have pores readily detectable under scanning electron microscopy and are structurally uniform down to a scale of at least 100 nm[5].) This conclusion appears to contradict the findings of several other groups, who reported that when cells are plated on an array of flexible silicone microposts, their spreading and differentiation depend on the rigidity of the substrate[6,7], and that when cell are plated on silicone gels, their differentiation depends on the gel rigidity[8]. To resolve this contradiction, we used commercially available soft, medium, and hard silicone gel substrates with nominal elastic moduli of 0.5, 16, and 64 kPa, respectively, to perform experiments similar to those reported in refs 3 and 4, testing the dependence of differentiation and spreading of MSCs and of spreading of fibroblasts and keratinocytes on the substrate rigidity.

Results and Discussion:

Elastic moduli, E, of the silicone gels were measured by assessing the deformation of thin layers of gels under known shear stresses using a previously reported microfluidic technique[9]

(Fig. 4-4A–C) and a newly developed gel rheometer (Fig. 4-4D–F). For all three gels and with both measurement techniques, shear strain, γ, was a linear function of the shear stress, τ, up to the highest tested levels of γ (~0.02, ~0.03 and ~0.3 for the 64, 16, and 0.5 kPa gel, respectively). The actual values of E obtained from the measurements were consistent with the nominal values of E (0.4 and 0.61 kPa for the 0.5 kPa gel, 17 and 20 kPa for the 16 kPa gel, and 62 and 65 kPa for the 64 kPa gel; see Supplementary Information for further details). Furthermore, the dependencies of γ vs. τ for gel layers with thicknesses of 18, 6.1 and 2.4 μm (measured for a gel with a nominal E = 2 kPa with a modified version of the microfluidic technique) were nearly indistinguishable from each other and also linear up to the highest tested γ of ~0.5 (Fig. 4-4G). The value of E calculated from the measurements (~1.7 kPa) was consistent with the value obtained from measurements on a 1 mm layer of the gel, suggesting that the elastic moduli of the silicone gels are uniform down to a subcellular scale of 2.4 μm. From measurements of shear strain as a function of time after abrupt changes in the shear stress, the relaxation times of the gels were estimated as ~4 s for the 0.5 kPa gel and <1 s for both 16 and 64 kPa gels (Fig. 4-4H–J). These measurements also indicated that all three gels are true solids that undergo finite deformations in response to shear stress.

In experiments on MSCs, the silicone gel substrates (as well as a plastic substrate used as a control) were coated with collagen I. To study MSCs differentiation, cells were cultured in an adipogenic or an osteogenic medium for 14 days. In an adipogenic medium (Fig. 4-1A,B), when MSCs were plated on the 64 kPa substrate, their differentiation to adipocytes somewhat increased as compared to a plastic substrate control, and when the MSCs were plated on the 16 kPa and 0.5 kPa substrates, their differentiation to adipocytes increased > 3-fold. In an osteogenic medium (Fig. 4-1A,B), the differentiation of MSCs to osteoblasts was reduced to

~80% on the 64 kPa substrate as compared with a plastic control and was further reduced to ~36% on the 16 kPa substrate and to ~27% on the 0.5 kPa substrate, with the differences between the three substrates and the control being all significant.

In experiments on the spreading of MSCs keratinocytes and fibroblasts, a regular cell culture medium was used and cell spreading areas were assessed 45 minutes after cells were plated. The average spreading areas of MSCs were significantly smaller on the 0.5 kPa silicone gel than on the 16 and 64 kPa gels (Fig. 4-2A,B). The average areas of primary mouse keratinocytes and mouse embryonic fibroblasts (MEFs) cultured on the silicone gel substrates monotonically increased with the substrate elastic moduli, with differences in the cell areas between the three substrate rigidities being all significant for both cell types (Fig. 4-5A,B). In agreement with the previous report[10], we found the phosphorylation level of focal adhesion kinase (FAK) to monotonically increase with the substrate rigidity for both keratinocytes and MEFs (Fig. 4-5C). Finally, deformations of the silicone gel substrates by traction forces of adherent MEFs were inverse functions of the substrate rigidity and had magnitudes comparable to those reported on hydrogels of similar elastic moduli[3,11] (Fig. 4-3). Therefore, in all four types of assays, the dependence of the cellular functions on the substrate rigidity was qualitatively the same as for cells cultured on hydrogels and micropost arrays, suggesting that the effects of substrate rigidity on functions of plated cells are similar for all types of deformable substrates. These results demonstrate that substrate rigidity induces some universal cellular responses that are independent of porosity or topography of the substrate.

To explain the discrepancies between our findings and the conclusions of refs 3 and 4 we note that, whereas we plated cells on substrates from all three ranges of rigidity, none of the silicone gel substrates used in refs 3 and 4 was clearly shown to be either soft or of medium

rigidity (Fig. 4-6; Supplementary Discussion). In addition, the surfaces of silicone gel substrates used in our study have amino-reactive groups (Fig. 4-7), providing covalent binding of ECM proteins similar to the binding of ECM to the surfaces of hydrogels in refs 3 and 4. It is not completely clear, whether the ECM binding to the silicone gel surfaces used in refs 3 and 4 was covalent or passive, and as argued in both papers, cellular responses to the substrate rigidity are expected to depend on the details of binding of ECM to the substrate (see Supplementary Discussion).

Materials and Methods:

Silicone gel substrates for cell culture

6-well plates with silicone gels on the well bottoms (SoftSubstrates™) were obtained from MuWells (softsubstrates.com, San Diego, CA).

Measurements of elastic moduli of silicone gels substrates

Elastic moduli of the silicone gels were measured by assessing the deformation of thin layers of gels under known shear stresses (Fig. 4-7) using a previously reported microfluidic technique[9] (See Supplementary Methods).

Assaying density of amine-binding sites on silicone gel substrates

To assess the density of amine-binding sites on the silicone gel substrates Fig. 4-7), we used fluorescent beads functionalized with amine groups (See Supplementary Methods).

Stem cell differentiation

Human mesenchymal stem cells (hMSCs) of early passages (P0) were obtained from Stemedica (San Diego, CA). Silicone gels substrates were coated with 1.6 μg/ml solution of collagen I (Advanced Biomatrix, San Diego, CA) in pH 7.4 PBS for 30 min at 37 °C. hMSCs were seeded into the 6-well plates at 600 cells/cm^2 in 2 mL of 7.5% BGS (EquaFETAL® , AtlasBIOLOGICALS) hMSC growth media (Stemedica) and grown in humidified oxygen-controlled 37 °C incubator with 5% O_2 and 5% CO_2. Cells were allowed to reach ~75% confluence before a differentiation medium (ThermoFisher) was applied to induce either adipogenesis or osteogenesis. After 7 days, the differentiation medium was refreshed, and after 14 days cell were examined to assess their differentiation. Adiposeness was assessed using AdipoRed (ThermoFisher), according to a protocol recommended by the manufacturer with the following modifications: prior to the addition of AdipoRed, all cells from the wells of a 6-well plate were harvested by trypsinization, washed once in pH 7.4 PBS, resuspended in 1.2 ml of PBS and transferred into a 96-well plate (200 uL of cell suspension per well); AdipoRed was added to each well of the 96-well plate, incubated for 20 min at RT, and the intensity of staining was measured using a fluorimeter (FLX800, Biotech Instruments Inc). Osteoblasts were stained with Alizarin Red and imaged using Evos FL cell imaging system (Advanced Microscopy Group, Mill Creek, WA), with the level of osteogenesis assessed as previously described[12]. Alternately, osteogenesis was assayed as described in refs 4. Briefly, hMSCs were seeded at a density 2,000 cells/cm^2, cultured for 1 hour, and the differentiation medium was applied. Cells were assayed for ALP activity after 7 days.

Figure 4-1: Differentiation of stem cells on substrates of different rigidities.
(A) Chemically induced adipogenesis (left column) and osteogenesis (right columns) of hMSCs cultured on silicone gel substrates with different elastic moduli. The brightness in the left column shows fluorescent staining of adipocytes after 14 days of differentiation. Red color in the right column corresponds to calcium staining after 14 days of differentiation. (B) Chemically induced osteogenesis (black) and adipogenesis (grey) of human mesenchymal stem cells (hMSCs). Left and right ordinates indicate the levels of differentiation to osteoblasts and adipocytes, respectively, (n = 3 wells; representative results from 3 independent experiments) normalized to the levels of differentiation of hMSCs plated on plastic surfaces. ***$p < 0.01$.

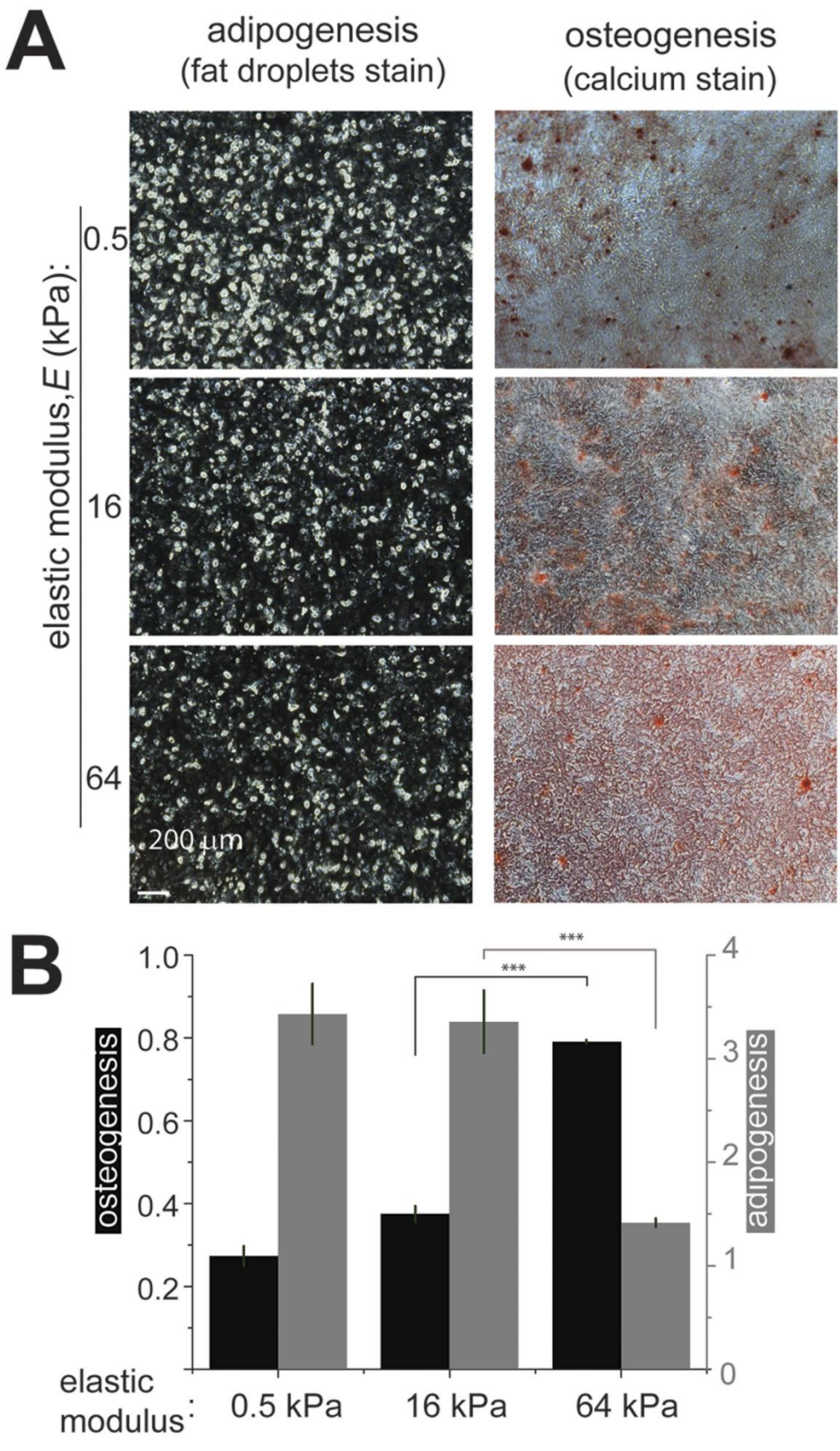
A
adipogenesis
(fat droplets stain)
osteogenesis
(calcium stain)
elastic modulus,E (kPa):
0.5
16
64
200 μm
B
osteogenesis
adipogenesis
1.0
0.8
0.6
0.4
0.2
4
3
2
1
0
***
***
elastic modulus:
0.5 kPa
16 kPa
64 kPa

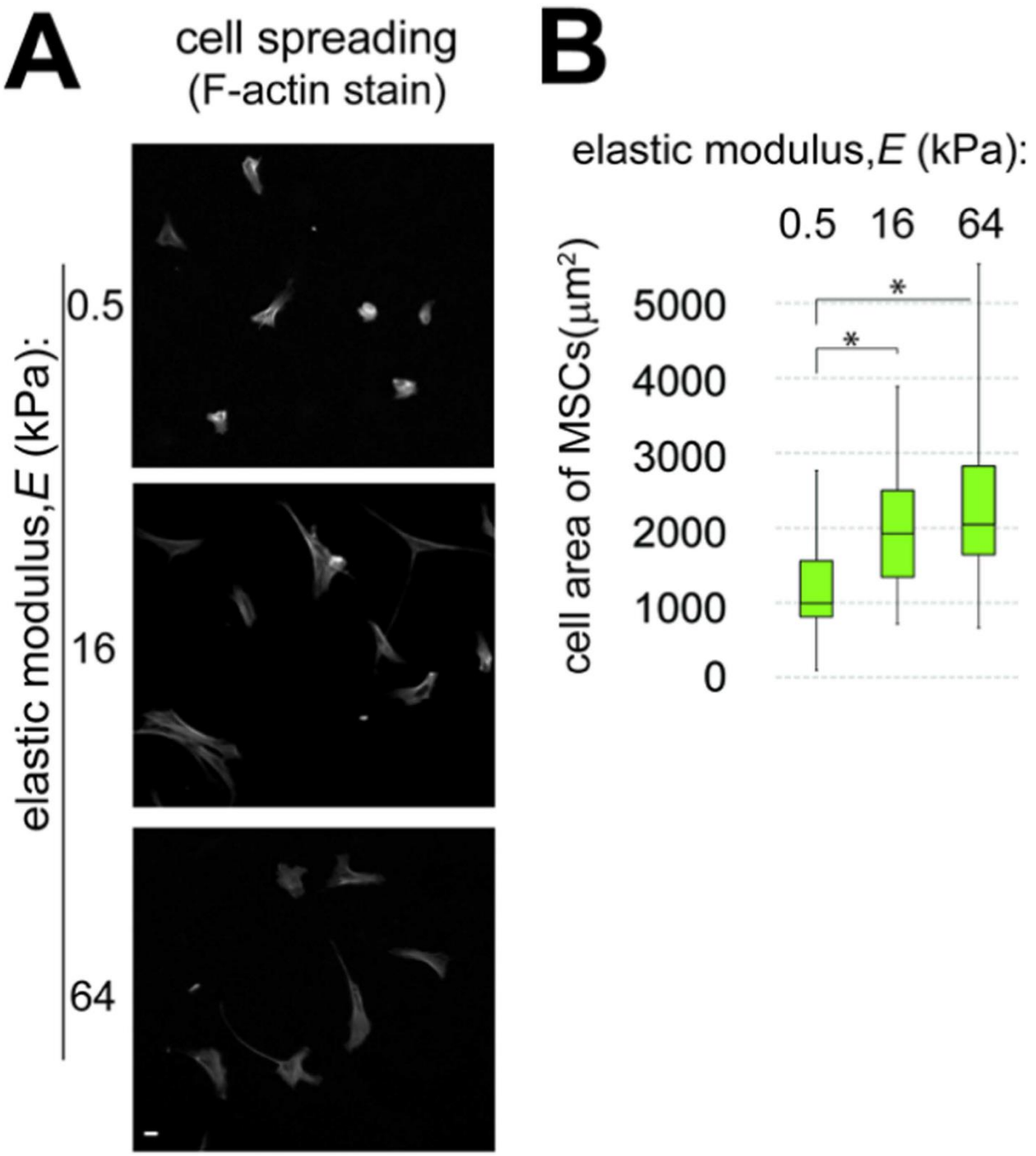

Figure 4-2: Spreading of stem cells on substrates of different rigidities.
(A) Representative fluorescence images of hMSCs on silicone substrates with elastic moduli of 0.5, 16, and 64 kPa. The substrates were coated with collagen I and cells were stained with phalloidin to fluorescently label F-actin. (B) Spreading areas of hMSCs on silicone substrates with different elastic moduli obtained from the analysis of the fluorescence images. Box corresponds to interquartile range of cell spreading areas; black line indicates median value; whiskers show minimal and maximal values. N = 40 cells for each type of substrates. *statistical significance with $p < 0.01$.

Cell spreading assay

To measure hMSC spreading areas, hMSCs were plated onto silicone gel substrates in 6-well plates and cultured for 24 hours in 2 mL of 7.5% BGS (EquaFETAL®, AtlasBIOLOGICALS) hMSC growth media (Stemedica) and grown in humidified oxygen-controlled 37 °C incubator with 5% O_2 and 5% CO_2. Cells were then fixed with 3.7% formaldehyde in PBS, permeabilized with 0.5% Triton X-100 in PBS at RT for 10 min, and washed three times with PBS. The fixed cells were incubated with phalloidin-conjugated rhodamine (Molecular Probes) for 45 min at RT and washed three times with PBS. Next, cells were photographed under a fluorescence microscope. Mouse primary keratinocytes and mouse embryonic fibroblasts (MEFs) were plated on ~30 μm layers of the 0.5, 16, and 64 kPa silicone gels on #1.5 microscope cover glasses (special order from MuWells), making it possible to measure their spreading areas under fluorescence microscope with improved resolution. Silicone gel surfaces were coated with fibronectin (ThermoFisher) by incubation under a 20 μg/ml solution of fibronectin in pH 7.4 PBS for 30 min at RT. Keratinocytes and MEFs were plated on fibronectin-coated silicone gels and incubated in DMEM supplemented with 1% (v/v) BSA for 45 min at 37 °C, 5% CO2. Cells were fixed and stained with phalloidin as described above. Next, the cover glasses were mounted on microscope slides with a mounting solution (ProLong® Gold antifade reagent; Invitrogen) and cells were photographed under a fluorescence microscope. The micrographs were digitally processed and cell spreading areas were quantified using a code in MATLAB (MathWorks, Natick, MA). For each substrate elastic modulus and each cell type, the spreading areas were measured for 75 cells in randomly selected areas of the substrate (Fig. 4-1D; Fig. 4-5B).

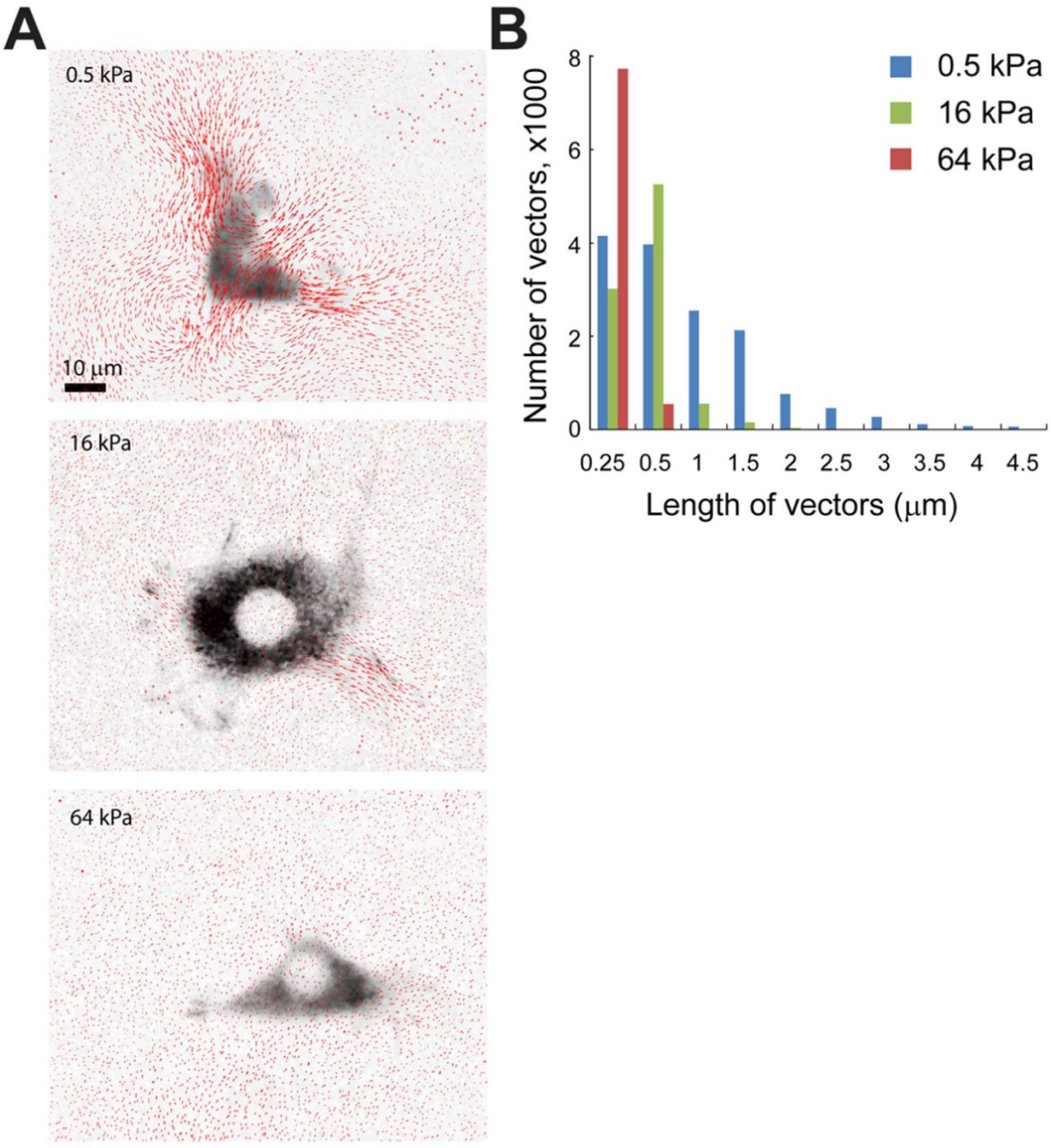

Figure 4-3: Cell-induced deformations of substrates of different rigidities.
(A) Inverted greyscale fluorescence images of fibroblasts plated on substrates with E = 0.5, 16, and 64 kPa superimposed with vector maps of the surface displacement (red arrows). Fibroblasts are expressing paxillin-mCherry. Vector maps are obtained by tracking the displacements of 40 nm red fluorescent beads attached to the substrate surface[3,9]. (B) Histograms of the lengths of surface displacement vectors for substrates of different rigidities.

Preparation of cell lysates and Western blotting

Keratinocytes and MEFs were plated on fibronectin-coated silicone gel substrates in the 6-well plates and incubated for 45 min at 37 °C, 5% CO_2. Whole cell lysates were prepared using modified radioimmune precipitation assay buffer (50 mM Tris, pH 7.5, 150 mM NaCl, 50 mM NaF, 1 mM sodium pyrophosphate, 0.1% sodium deoxycholate, 1% Nonidet P-40, protease inhibitors cocktail and 1% CHAPS). Lysate protein was quantified using the bicinchoninic acid (BCA) method (ThermoFisher Scientific), normalized, and used in Western blots analysis. The primary antibodies for Western blots were against Y576FAK (ThermoFisher), FAK (Cell Signaling), and α -tubulin (Sigma) (Fig. 4-5C).

4.2. Supplementary Material

Measurements of elastic moduli of silicone gel substrates

Elastic moduli of the silicone gels were measured by assessing the deformation of thin layers of gels under known shear stresses using a previously reported microfluidic technique[1] (Fig. 4-4A-C), a newly developed gel rheometer[2] (Fig. 4-4D-F), and a modified version of the microfluidic technique (Fig. 4-4G-I). In the first microfluidic technique, thin uniform layers of the silicone gels (30 – 65 μm thickness) used in the 0.5, 16, and 64 kPa 6-well plates were prepared on 50x35 mm #1.5 microscope cover glasses with 100 nm fluorescent beads deposited on the cover glass surfaces (special order from MuWells). The gel surfaces were coated with 40 nm red fluorescent beads (see below) and the thicknesses of the gel layers, ξ, were measured under a fluorescence microscope by focusing first on the beads on the surface of the coverglass and next on the beads on the surface of the gel. A specially designed microfluidic device was bonded to the surface of each gel substrate. The device was perfused with a 80:20 mixture of

glycerol and water (by weight) by applying controlled differential pressures, ΔP, between the inlet and outlet of the device. The displacements of the beads on the gel surface, Δx, near the middle of the bottom of a 2 mm long, 2 mm wide and $h = 165$ μm deep channel of the device were measured under a fluorescence microscope at different hydrodynamic shear stresses, τ. The values of τ were calculated from ΔP using a prior calibration of the device. (The calibration was performed by perfusing the device with a 80:20 glycerol:water mixture with viscosity $\eta = 0.060$ Pa·s, which was seeded with 4.6 μm green fluorescent beads. The flow velocity at the mid-plane of the channel, v, was assessed at different ΔP by visualizing the bead streak lines, and the shear stress was calculated as $\tau = 6\eta v/h$.) The displacement of beads on the gels surface, Δx, was used to calculate the substrate shear strain, $\gamma = \Delta x/\xi$. The dependences of γ on τ were measured for all three gel types (Fig. 4-4A-C). There was no detectable hysteresis or creep (slow growth of strain under constant stress) in any of the tests and all three dependencies of γ on τ were well fitted by straight lines passing through the origin, such that all three types of gels behaved as proper solids. The slopes of the straight line fits were used to calculate the shear moduli of the gels, $G = \tau/\gamma$. The elastic moduli (Young's moduli) of the gels were calculated as $E = G/3 = \tau/3\gamma$ (assuming a Poisson ratio of 0.5)[1]. The values of E were found at 0.61, 20, and 62 kPa for the 0.5, 16, and 64 kPa gels respectively.

With the newly developed gel rheometer, the deformations of 20x30 mm rectangular gel layers with thickness from 1.35 to 1.54 mm were tested under centrifugal force[2], and the dependences of the average shear strain, γ, on the average shear stress, τ, were measured (Fig. 4-4D-F). The dependencies were fitted again by straight line passing through the origin, and their slopes were used to calculate the shear moduli, $G = \tau/\gamma$, and the elastic moduli $E = G/3 = \tau/3\gamma$ of the gels (assuming again a Poisson ratio of 0.5)[1]. The values of E were found at 0.40, 17,

and 65 kPa for the 0.5, 16, and 64 kPa gels respectively (Fig. 4-4D-F). The values of the elastic moduli measured by the two techniques for the gels with the nominal elastic moduli of 16 and 64 kPa are in good agreement with each other and with the nominal values (20 and 17 kPa vs. 16 kPa; 62 and 65 kPa vs. 64 kPa). The discrepancy between the values of E measured with the two techniques (0.61 and 0.40 kPa) and the stated value of E for the 0.5 kPa gel is greater and is likely due to batch-to-batch variability (all gels samples were from different batches). Nevertheless, the uncertainties in the elastic moduli of the 0.5, 16, and 64 kPa gels, as estimated from our mechanical measurements, do not affect the major conclusions from any of our experiments on cells plated on these gels (cf. Fig. 4-1,2; Fig. 4-5).

To check for possible variation of the effective elastic moduli of the silicone gels on scales <30 μm, we used a modified version of the microfluidic technique to test 18, 6.3, and 2.4 μm thick layers of the SoftSubstrates gel with nominal $E = 2.0$ kPa (special order from MuWells). As before, there was a low concentration of fluorescent beads (40nm, red fluorescent) on the coverglass-gel interface and a higher concentration of the same beads covalently bonded to the gel surface. The thicknesses of the gels were assessed by taking stacks of fluorescence images on a confocal microscope with a precise z-axis encoder and finding the z-axis positions at which the beads on the interface and the gel surface were maximally in-focus. The modifications of the microfluidic technique were two-fold. First, the dimensions of the test chamber were reduced ~3-fold (as appropriate for the relatively thing gel layers tested), to ~600x600x60 μm. Second, instead of the 80:20 glycerol:water mixture, the working fluid was Helium, thus enabling faster measurements without the risk of spill. (The correspondence between τ at the gel surface at the bottom of the test chamber and ΔP between the inlet and outlet of the device was calibrated by perfusing the device with a suspension of fluorescent beads in water and measuring

the streak lines of the beads at various ΔP; the correspondence was theoretically predicted to be the same for Helium as for water.) For all three gel thicknesses, the dependences of the shear strain, $\gamma = \Delta x/\xi$ on τ were well-fitted by zero-crossing straight lines (Fig. 4-4G). The values of E calculated from the dependencies, 1.70, 1.78, and 1.65 kPa, respectively, for the 18, 6.3, and 2.4 μm thick gels, were consistent with each other, with the value of 1.9 kPa from our measurement on a 1.05 mm thick sample using the shear rheometer, and with the nominal value of 2 kPa. The results of this test indicated that the effective elastic modulus of the gels used in our study is uniform down to a subcellular scale of 2.4 μm.

Finally, we used the rheometer to measure changes in shear strains of gel layers, $\gamma = \Delta x/\xi$, upon step-wise changes in the shear stress in order to estimate relaxation times of the gels (Fig. 4-4H-J). The relaxation time of a gel corresponds to a temporal scale at which the effective viscosity of the gel is as important as its elasticity. Processes with time scales shorter than the relaxation time are expected to be viscosity-dominated, whereas processes with time scales longer than the relaxation time are elasticity-dominated. Based on results of these tests, the relaxation times of the 0.5, 16, and 64 kPa gels (actual values of E measured at 0.44, 18, and 64.5 kPa, respectively) were estimated at <4, <1, and <1 sec, respectively. A relaxation time of 4 sec would certainly be a major factor for some rapid cellular processes sensitive to the mechanics of the substrate, such as changes in contractility of cardiomyocytes. On the other hand, changes in cellular adhesions and contractility during the spreading of cells and differentiation of stem cells occur on substantially longer time scales (tens of second)[3], rendering the relaxation time of 4 sec too short to make the viscous properties of the 0.5 kPa gel relevant for these cellular processes. (The relaxation times of the 16 and 64 kPa gels are even shorter, making their viscosities even less relevant.)

Assaying density of amine-binding sites on silicone gel substrates

To assess the density of amine-binding sites on the silicone gel substrates, we used 40 nm red fluorescent beads functionalized with amine groups. The beads were prepared by incubating 40 nm carboxylated fluorescent beads (580nm excitation/605nm emission; F-8793 by Life Technologies) with silane-PEG-amine (from Laysan-Bio, Arab AL). The bead suspensions were used at two dilutions, 1:20,000 (high concentration) and 1:160,000 (low concentration), in 20 mM HEPES buffer (pH 8). To assay the binding of beads to the silicone gel substrates, bead suspensions were incubated in wells of the silicone gel-bottom 6-well plates for 30 min at room temperature (RT). After the incubation, the wells were thoroughly rinsed with water and the fluorescent beads attached to silicone gel surfaces at the well bottoms were photographed under a fluorescence microscope. The assay was performed in 6-well plates with gels of all three elastic moduli and with both low-concentration and high-concentration bead suspensions (Fig. 4-7). The bead density on the gel substrates was found to be consistent between substrates of all three elastic moduli for both high-concentration and low-concentration bead suspensions.

To test for the specificity of the binding of beads to the gel substrates, a 64 kPa gel on a well bottom was incubated for 30 min under a pH 8.5 HEPES buffer and then for 30 min under the high-concentration bead suspension. The pre-incubation under pH 8.5 HEPES was expected to result in hydrolysis of the amino-reactive groups on the gel surface. The density of fluorescent beads on the gel surface was found to be greatly reduced as compared with the bead density obtained with the same high-concentration suspension without the pH 8.5 HEPES pre-incubation and was also markedly lower than the density obtained with the low-concentration bead suspension without the pH 8.5 HEPES pre-incubation.

Taken together, these results indicate that the surfaces of the silicone gels of all three elastic moduli used in our study are indeed functionalized with amino-reactive groups and the effective site density of these groups is similar for gels of all three rigidities. Therefore, a 6-well plate used in the study is filled with a solution of ECM proteins, the protein molecules are expected to covalently bind to the gels surfaces through their amino groups, with the covalent binding being equally efficient for gels of all three elastic moduli.

Stem cell differentiation

Human mesenchymal stem cells (hMSCs) of early passages (P0) were obtained from Stemedica (San Diego, CA). Silicone gels substrates were coated with 1.6 μg/ml solution of collagen I (Advanced Biomatrix, San Diego, CA) in pH 7.4 PBS for 30 min at 37 °C. hMSCs were seeded into the 6-well plates at 600 cells/ cm2 in 2 mL of 7.5% BGS (EquaFETAL®, AtlasBIOLOGICALS) hMSC growth media (Stemedica) and grown in humidified oxygen-controlled 37 °C incubator with 5% O2 and 5% CO2. Cells were allowed to reach ~75% confluence before a differentiation medium (ThermoFisher) was applied to induce either adipogenesis or osteogenesis. After 7 days, the differentiation medium was refreshed, and after 14 days cell were examined to assess their differentiation. Adiposeness was assessed using AdipoRed (ThermoFisher), according to a protocol recommended by the manufacturer with the following modifications: prior to the addition of AdipoRed, all cells from the wells of a 6-well plate were harvested by trypsinization, washed once in pH7.4 PBS, resuspended in 1.2 ml of PBS and transferred into a 96-well plate (200 uL of cell suspension per well); AdipoRed was added to each well of the 96-well plate, incubated for 20 min at RT, and the intensity of staining was measured using a fluorimeter (FLX800, Biotech Instruments Inc). Osteoblasts were stained

with Alizarin Red and imaged using Evos FL cell imaging system (Advanced Microscopy Group, Mill Creek, WA), with the level of osteogenesis assessed as previously described[4]. Alternately, osteogenesis was assayed as described in Ref. 5. Briefly, hMSCs were seeded at a density 2,000 cells/cm2, cultured for 1 hour, and the differentiation medium was applied. Cells were assayed for ALP activity after 7 days.

Supplementary Discussion

In their experiments, both Trappmann et al.[5] and Wen et al.[6] used silicone substrates prepared by mixing different proportions of the components B and C of Sylgard 184 elastomer (Dow Corning). The values of the elastic moduli, E, for Sylgard 184 mixtures with a range of B:C have been measured by several groups using different experimental techniques. These values are plotted as a function of B:C in Fig. 4-6A. There is a good agreement between the values of E obtained from the extension tests on cylindrical samples by Cesa et al.[7] (Fig. 4-6A, black triangles) and our measurements under shear using the specially built shear rheometer (Fig. 4-6A, green circles). In addition, there is a good agreement between the results obtained with the shear rheometer and with our microfluidic tests for B:C from 20:1 to 30:1 and from 65:1 to 75:1. On the other hand, in the range of B:C from 40:1 to 55:1, the microfluidic tests measured E as much as 1.5-times lower (or corresponding to B:C ratios ~5 points greater) than the tests with the rheometer and the tests on cylindrical samples. The value of E for B:C = 50:1 from Trappmann et al.[5] (Fig. 4-6A, blue squares) is ~1.5 times greater than the values measured with the cylindrical samples and with the shear rheometer and the rest of the values of E in the interval of B:C from 20:1 to 50:1 from Trappmann et al.[5] are 1.5-2 times greater than the values of E obtained from the measurements under extension and shear. These discrepancies can be due to

variability of properties between different batches of Sylgard 184. Indeed, there is a considerable variability in the values E measured at different times (and hence, for different samples and batches) by the same groups (Fig. 4-6A). It is worth noting, however, that the measurements using shearing of thin layers and extension of cylinders (or slabs) both rely on simple deformations and involve minimum assumptions about mechanical properties of the gels, and their results depend on the Poisson ratios of the gels (expected to be close to 0.5) only weakly. In contrast, the deformations produced by indenters (both flat and round) are of a relatively complex and sample thickness-dependent profiles, and the experimental readout may be more dependent on the Poisson ratio and on the details of interaction between the indenter and the surface of the material.

The data point for B:C = 100:1 from Trappmann et al.[5] (Fig. 4-6A, blue squares), with E = 0.1 kPa, does not appear to be inconsistent with the trends in the data obtained with the stretching of the cylindrical samples and with the shear rheometer and microfluidic technique (although an extrapolation of those two last sets of data to B:C = 100:1 would give a value of E an order of magnitude below 0.1 kPa). Nevertheless, we have never been able to make mixtures with B:C $\geq$ 80:1 to form solids. They always remained liquid even after multiple days of curing at an elevated temperature of 100°C (Fig. 4-6B). Rheological tests on a B:C = 100:1 mixture cured overnight at 80°C (Fig. 4-6D) indicated that it was a Newtonian liquid with a viscosity of 2000 Pas, which was ~400 greater than the viscosity of component B of Sylgard 184 (5.1 Pas according to the manufacturer). Thus, the addition of 1% component C lead to substantial polymerization (hence the increase in viscosity), but not curing. Rheological tests on a B:C = 85:1 mixture cured overnight at 80°C indicated that it was a viscoelastic liquid with a viscosity of 5500 Pas, some shear-thinning, and detectable elastic properties (detectable recoil after the

stress is dropped; Fig. 4-6C). Thus, as expected, the addition of a greater amount of component C (~1.17% vs. 1%) lead to increased polymerization (hence the increase in viscosity and detectable elasticity), but still did not produce a solid material (Fig. 4-6C). It is instructive to compare the plots in Fig. 4-6C and D, showing mechanical responses of liquids, with the plot in Fig. 4-4H, showing the mechanical response of the 0.5 kPa SoftSubstrates gel, which is a solid. Whereas in the two first cases constant shear stresses lead to constant shear rates, and the samples remain deformed after the stresses are relieved, in the last case, after a stress is applied, the deformation rapidly reaches a plateau and, after the stress is relieved, the sample regains the shape it had before the application of the stress.

It is our understanding that the elastic modulus for the material with B:C = 100:1 was measured in the test presented in Fig. S1d in Ref.[5], in which a layer of the material was indented with a 20 mm flat punch. The elastic modulus of 0.1 kPa was then calculated as a number proportional to the value of load force at time going to infinity. As far as we can judge from the plot in Fig.S1d in Ref.[5], the value of the load force is <0.1 g (~5% of the peak value of load in the test) at the largest time plotted (~270 sec) and continues decaying with time. Therefore, the fact that the measured load force is different from zero (which would be expected from a liquid in a steady state) may be explained by a combination of an insufficient time of observation and limited accuracy of the experimental system (zero drift etc.). Thus, in our view, the results of the test in Fig.S1d in Ref.[5] do not clearly demonstrate that the sample with B:C = 100:1 is a solid.

It also did not escape our attention, that when keratinocytes were plated on substrate with B:C = 100:1, the substrate had a visible pattern of wrinkles on a scale of several μm (top left panel in Fig.1C in Ref.[5]). This pattern is reminiscent of the pattern of wrinkles that was produced by cells plated on the surface of liquid silicone with a thin hard crust, which was formed by

flaming the silicone surface[8] (and apparently resulted from the buckling instability of the crust under the action of the traction forces of the cells). Therefore, we suspect that a similar thin hard crust might have been formed on the surface of the B:C = 100:1 material in Ref.[5], when it was treated with UV-light and reactive chemicals for the purpose of functionalization of the surface.

The above considerations suggest that the phenotypes of cells plated on the substrates with B:C = 100:1 in Ref.[5] may reflect the responses of the cells to the unknown rigidity of the hard crust rather than to the stated elastic modulus of the material (0.1 kPa). Therefore, the phenotypes of cells plated on the substrate with B:C = 100:1 cannot be reliably qualified as phenotypes of cells plated on a soft gel. We note that in Ref.[5], the data on cells plated on the substrate with B:C = 100:1 are the only data on cells plated on either soft ($E < 4$ kPa) or medium rigidity (E = 8-17 kPa) substrates. If the data on cells on the B:C = 100:1 substrate are disregarded, the only data remaining are on cells on hard substrates, with $E \geq 40$ kPa (which may also have hard crusts on their surfaces). For PAA gels in this range of E, the dependence of cell phenotypes on the substrate rigidity is usually found to be weak or insignificant (cf. Fig.1 and Fig.3 in Ref.[5]). Hence, the similarity of phenotypes of cells plated on the silicone substrates used by Trappmann et al.[5] does not imply that cells do not respond to rigidity of silicone gels or that cellular responses to rigidity of silicone gels are different from cellular responses to rigidity of PAA gels.

In their paper, Wen et al.[6] state “These results, in conjunction with cure ratio-independent stem cell spreading (Supplementary Fig.11B) and differentiation (Fig.4E), emphasize the shortcomings of PDMS as a model system to investigate stiffness-dependent behavior over a relevant cell-sensing range.” The phrase “these results” in the beginning of this sentence refers to the difficulty of functionalization of surfaces of silicone gels with reactive groups; we will

address this subject later. As for the results shown in Fig.4E and Supplementary Fig.11B in Ref.[6], they indicate that both MSC differentiation and ASC spreading are practically identical for cells plated on substrates obtained from mixing the B and C components of Sylgard 184 at 50:1, 75:1, and 100:1. We immediately note, however, that both 50:1 and 100:1 substrates were found to be more rigid than the PAA gel with E = 30 kPa (Fig.4D in Ref.[6]; the mechanical characterization for the 75:1 mixture was not presented). As argued above, for hard substrates, with E > 40 kPa, the dependence of cell phenotypes on the substrate rigidity is expected to be weak or insignificant. Therefore, the similarity of phenotypes of cells plated on the 50:1, 75:1, and 100:1 substrates (Fig.4e and Supplementary Fig.11B in Ref.[6]) is consistent with the mechanical properties of these substrates, as they are presented in Ref.[6].

The experimental data obtained by us[1,9] (Fig. 4-1 and Fig. 4-7A) other authors[7,10–12] (Fig. 4-7A) indicate that silicone gels can be made of soft and of medium rigidity. Here we presented results indicating that the rigidity of silicone gels affects the phenotypes of cells plated on them in the same way as the rigidity of PAA gels[5,6,13,14] and micropost arrays[15].

A salient feature of the plot in Fig. 4-6A is that, when converted to elastic moduli, E, the values of rigidity of the Sylgard 184 silicone gels with B:C = 50 and 100 measured by Wen et al.[6] (red squares; they are reported as substrate spring constants) are visibly incompatible with the values and trends of elastic moduli measured by the other groups. Specifically, for B:C = 50, E is 20-50 times greater than the values obtained in the other studies and, for B:C = 100, which did not form a solid gel in our tests, E is on the same order as measured in the other studies for B:C = 36 – 45. We cannot know the exact reasons for this discrepancy. However, an obvious consideration is that the measurement technique used by Wen et al.[6] relies upon the resistance of the substrate to the retraction of an AFM tip brought into contact with the surface of the

substrate. Hence, results of measurements with this technique may specifically depend on the properties of the surface of the substrate (or a thin layer at its very top) and thus may not be universally related to the elastic properties of the bulk of the substrate. The relation between the resistance force and the elastic modulus of the substrate may not be a simple proportionality and may be different for silicone and PAA gels. If this is the case, our conversion of the spring constants measured by Wen et al.[6] to elastic moduli is not legitimate and there is also no obvious way to perform such a conversion or unambiguously relate the results obtained by Wen et al.[6] for cells on silicone substrates to the existing literature, in which the substrates were characterized by elastic moduli of their bulk[1,7,9–12].

Fig.4E and Supplementary Fig.11B in Ref.[6] show similar MSC differentiation and ASC spreading on the B:C = 50:1 and 75:1 substrates. The measurements by different groups (Fig. 4-6A, all data except for red squares) suggest that these two substrates should be, respectively, of medium-to-high rigidity (13-40 kPa) and soft (<1 kPa) that would imply significant differences between spreading and differentiation for cells plated on these substrates. Notably, however, Wen et al.[6] also found similar spreading of ASC and differentiation of MSC on the substrates with B:C = 100:1, whereas we have not been able to make mixtures with B:C $\geq$ 80:1 to solidify. Therefore, an explanation of the results in Fig.4E and Supplementary Fig.11B in Ref.[6] could be that the 100:1 and 75:1 substrates (and possibly the 50:1 substrate) had hard crusts formed on their surfaces. The formation of the hard crusts would then also explain the high values of the substrate spring constants measured for these silicone substrates (Fig.4D in Ref.[6]).

Finally, we note that, when untreated, the surfaces of both PDMS (and other silicones) and PAA are chemically inert and do not spontaneously form covalent bonds with ECM proteins. Hence, whereas some ECM may bind to surfaces of both PDMS and PAA by passive absorption,

for strong and reliable binding of ECM, the gel surfaces need to be functionalized with some reactive groups. The chemical structures of PDMS and PAA are essentially different, however, such that the functionalization of surfaces or PDMS and PAA gels requires different reagents. So, as noted by Wen et al.[6], sulpho-SANPAH, a standard reagent for functionalization of PAA, cannot be expected to be efficient for PDMS. Strangely, Wen et al.[6] stated that "PDMS substrates do not support protein tethering" because there is an insufficient linking of the ECM to silicone gel surface. We do not see sufficient evidences supporting this statement. The surface chemistry of PDMS gels can be readily modified with a variety of silanes with reactive groups[9,16], and in this study we used silicone gels with surfaces functionalized with amino-reactive groups (Fig. 4-7). Therefore, in our view, ability to functionalize their chemically inert surfaces for ECM binding makes silicone gel substrates a versatile tool to study cellular rigidity sensing.

Figure 4-4: Measurements of the elastic moduli of the silicone gels.
Elastic moduli of the silicone gels used in the experiments on cells were tested by measuring the deformation of thin uniform layers of gels and calculating their shear strain, γ, under known shear stresses, τ, using a previously reported microfluidic technique[1] (A) – (C) and a specially built gel rheometer[2] (D) – (F).
(A), (B), and (C) Dependence of γ on τ for gels with nominal elastic moduli of 0.5, 16, and 64 kPa, respectively. The thicknesses of the gel layers are 37, 31, and 63 μm, respectively (special order from MuWells). All three dependencies are fitted by straight lines passing through the origin, and the elastic moduli of the gels are calculated from the fits as $E = (3\gamma/\tau)^{-1}$ at 0.61, 20, and 62 kPa for the 0.5, 16, and 64 kPa gels respectively.
(D), (E), and (F) Dependence of γ on τ for gels with nominal elastic moduli of 0.5, 16, and 64 kPa, respectively. The thicknesses of the gel layers are 1.40, 1.35, and 1.54 mm, respectively (special order from MuWells). All three dependencies are fitted by straight lines passing through the origin, and the elastic moduli of the gels are calculated from the fits as $E = (3\gamma/\tau)^{-1}$ at 0.40, 17, and 65 kPa for the 0.5, 16, and 64 kPa gels, respectively.
(G) Dependence of γ on τ for a silicone gel with a nominal elastic modulus of 2 kPa was measured for gel layers (all special orders from MuWells) with thicknesses of 18.2 μm (*blue circles*), 6.1 μm (*orange squares*), and 2.40 μm (*green triangles*) using a modified microfluidic technique with Helium as the working fluid. All three dependencies are fitted by straight lines passing through the origin, and the elastic moduli of the gel layers are calculated from the fits as $E = (3\gamma/\tau)^{-1}$ at 1.70, 1.78, and 1.65 kPa for the 18.2, 6.1, and 2.40 μm thick gel layers, respectively. A measurement with a shear rheometer on a 1.05 mm thick gel layer resulted in an elastic modulus of 1.90 kPa.
(H) – (J) Incremental shear strains, γ, of the 0.5, 16, and 64 kPa SoftSubstrates gels as functions of time under step-wise changes of shear stress, τ. The measurements were performed with the shear rheometer on 0.5, 16, and 64 kPa gels gel layers with respective thicknesses of 0.43, 2.55, and 2.52 mm (all special orders from MuWells; the actual values of *E* were measured at 0.44, 18, and 65 kPa, respectively). For the 0.5 kPa gel (H), the value of τ was increased from 0.42 to 20.6 Pa at 25 sec and reduced back to 0.42 Pa at 265 sec; for the 16 kPa gel (I), the value of τ was increased from 2.5 to 160 Pa at 10 sec and reduced back to 2.5 kPa at 70 sec; for the 64 kPa gel (J), the value of τ was increased from 201 to 487 Pa at 10 sec and reduced back to 201 Pa at 70 sec. The transition curves for γ after changes in τ were not well-fitted by single exponentials, which was not surprising, because a gel usually has a broad spectrum of relaxation times. Therefore, as representative relaxation times, we took times it took the transition to be 63% (1-e-1) complete. For the reductions in τ, the relaxation times were 3 sec for the 0.5 kPa gel and <1 sec for both 16 and 64 kPa gels. The temporal resolution of the measurement technique is on the order of 1 sec. Therefore, the relaxation times measured for the 16 and 64 kPa gels were experimentally indistinguishable from zero. For the increases in τ, the relaxation times were 5.5 sec for 0.5 kPa, 2.5 sec for 16 kPa, and 1.5 sec for 64 kPa. The rheometer operates in such a way, however, that it takes ~2 sec for τ to increase (a reduction in τ occurs faster). Therefore, the gel relaxation times obtained from the step-wise increases and decreases of τ are consistent, and when corrected for the instrumental delays and time resolution, the relaxation times of the 0.5, 16, and 64 kPa gels can be estimated at <4, <1, and <1 sec, respectively.

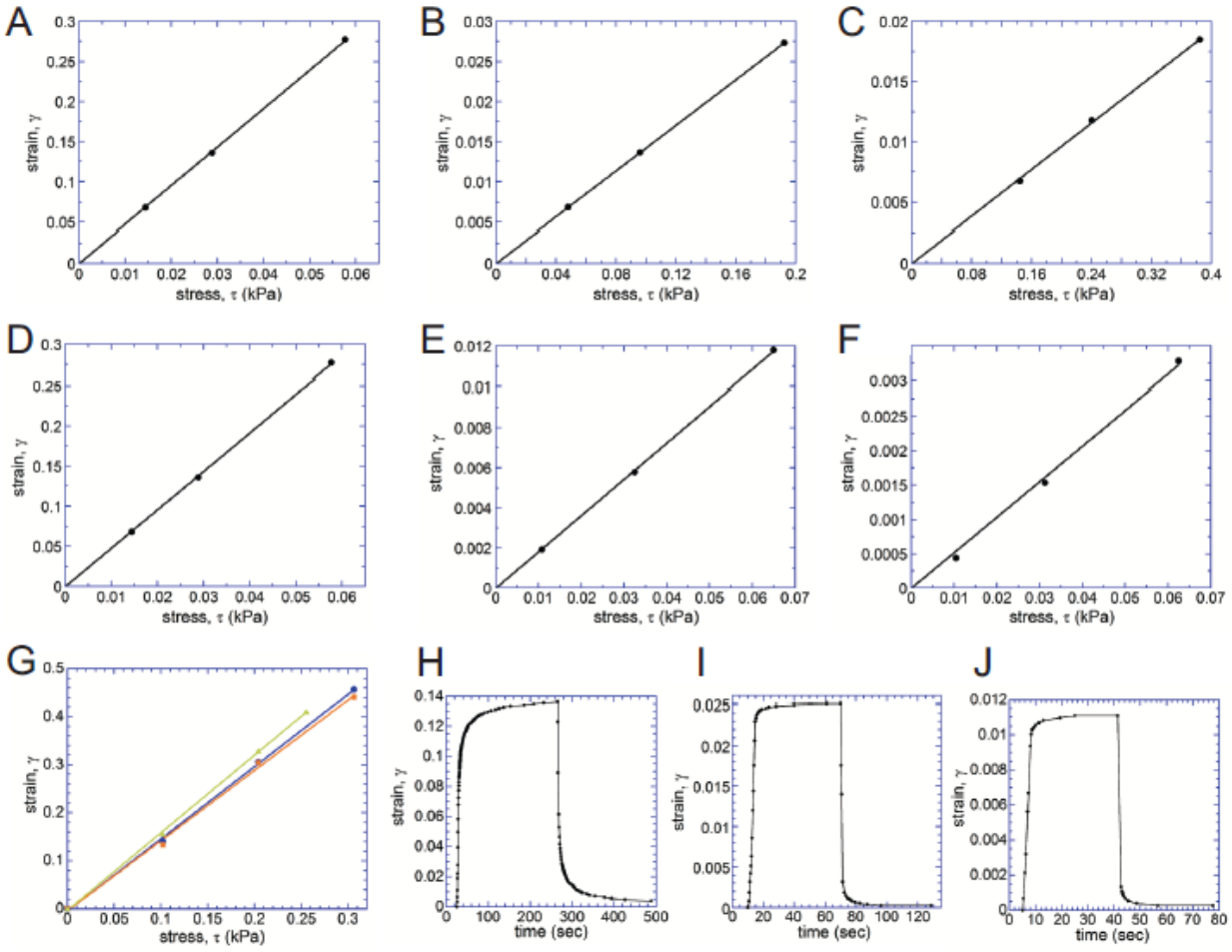
A
strain, γ
stress, τ (kPa)
B
strain, γ
stress, τ (kPa)
C
strain, γ
stress, τ (kPa)
D
strain, γ
stress, τ (kPa)
E
strain, γ
stress, τ (kPa)
F
strain, γ
stress, τ (kPa)
G
strain, γ
stress, τ (kPa)
H
strain, γ
time (sec)
I
strain, γ
time (sec)
J
strain, γ
time (sec)

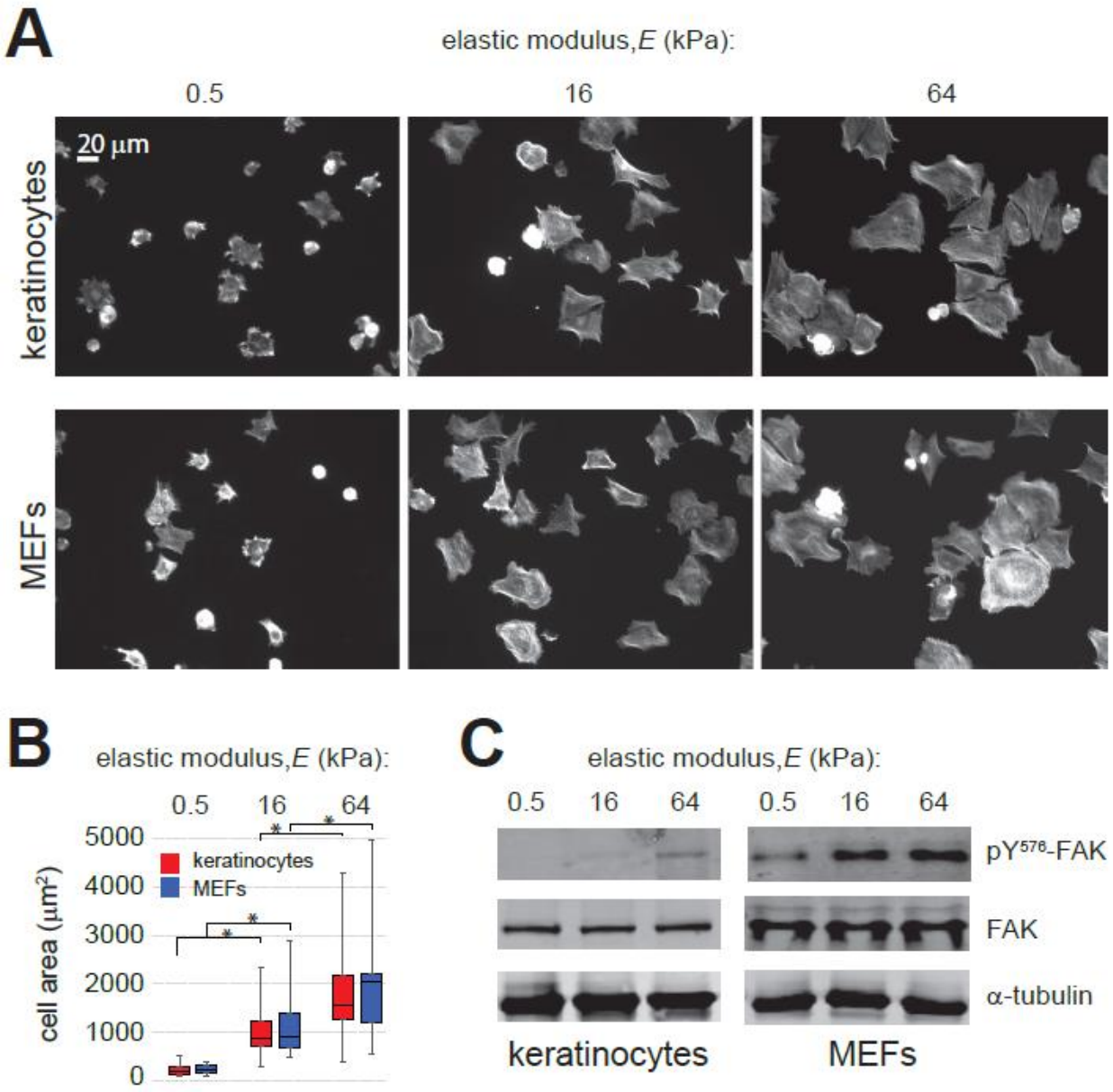

Figure 4-5: Spreading and signaling of cells on substrates of different rigidities.
(A) Representative fluorescence images of keratinocytes and fibroblasts on silicone substrates with elastic moduli of 0.5 16, and 64 kPa. The substrates were coated with fibronectin and cells were stained with phalloidin to fluorescently label F-actin.
(B) Spreading areas of keratinocytes (*red*) and fibroblasts (*blue*) on silicone substrates with different elastic moduli obtained from the analysis of the fluorescence images. Box corresponds to interquartile range of cell spreading areas; black line indicates median value; whiskers show minimal and maximal values. N=75 cells for each cell type on substrates of each elastic modulus. *- statistical significance with $p<0.01$.
(C) The levels of phosphorylation of FAK at Tyr-576 for keratinocytes and fibroblasts plated on substrates of different elastic moduli (*upper panels)*. *Middle panels* show the total amount of FAK, and *low panels* indicate the amount of α-tubulin, a gel loading control.

Figure 4-6: Mechanical properties of materials obtained from mixing different proportions of the base (B) and cross-linker (C) components of Sylgard 184 elastomer.
(A) Elastic moduli, *E*, of different mixtures of the B and C components of Sylgard 184 after curing, as measured by several groups using different techniques. *Black triangles* (and *black line*): measurements of axial stress of cylindrical samples as a function of the applied axial extension, from Cesa *et al.*[7] *Black diamonds:* measurements of axial stress of cylindrical samples as a function of the applied axial extension, from Schellenberg *et al.*[12]. *Open squares*: measurements of extension as a function of longitudinal stress applied to a slab, from Gutierrez *et al*.[1]. *Grey circles* (and *grey line*): measurements of shear strain of ~ 70 μm layer of gel as a function of hydrodynamic shear stress in a microfluidic setup, from Gutierrez *et al.*[1] *Green circles* (and connecting *green line*): measurements of shear strain as a function of shear stress with a specially built rheometer[2]. We performed the measurements over the course of two years on samples prepared from different batches of Sylgard 184. The samples were 1-2 mm thick and had lateral dimensions of 20x30 mm. *Blue squares* (and connecting *blue line*): measurements using indentation of gel layers, from Trappmann *et al*.[5]. *Red squares* (and connecting *red line*): values of *E* estimated based on the data from Fig. 4d in Wen *et al*.[6] by comparing the apparent stiffness of Sylgard silicone samples with that of polyacrylamide (PAA) gels of known elastic moduli (1 and 30 kPa). Wen *et al*.[6] quantified the stiffness as a substrate spring constant by measuring the resistance of the samples to the retraction of a probe of an atomic force microscope (AFM). For the two PAA gels at low speeds of the probe retraction, the ratio between the apparent substrate spring constant (in pN/mm) and *E* (in kPa) averaged at ~6.25. This average ratio was used to convert the apparent spring constants measured at low probe retraction speeds for silicone samples with B:C = 50:1 and 100:1, ~120 and ~10 pN/mm, respectively, into elastic moduli, *E* = 750 and 63 kPa, respectively.
(B) The base and curing agent components of silicone elastomer Sylgard 184 (Dow Corning) were mixed at ratios of B:C = 75:1, 85:1, and 100:1, in conical 50 ml tubes using an overhead stirrer. The silicone pre-polymer was spun down by centrifugation, and the test tubes were baked overnight in a forced convection oven at 80 °C. The test tubes were removed from the oven, allowed to cool to room temperature, turned upside down for 20 min and then photographed. *Blue arrow* points to the flat surface of solidified silicone gel, which was formed from the 75:1 mixture. *Red arrows* point to the surfaces of the silicone in the test tubes with the 85:1 and 100:1 mixtures. Uneven contours of the silicone surfaces in the last two test tubes show that both materials flow under gravity and are thus fluids rather than solids. We have tested different batches of Sylgard 184 elastomer multiple times, mixing its components at different proportions, baked the mixtures at temperatures up to 100 °C for multiple days, but have never been able to make mixtures with B:C $\geq$ 80:1 produce solid materials.

Figure 4-6: Mechanical properties of materials obtained from mixing different proportions of the base (B) and cross-linker (C) components of Sylgard 184 elastomer, continued:
C) Mechanical tests of the material obtained by mixing the components of Sylgard 184 at B:C = 85:1 and curing the mixture overnight in a forced convection oven at 80 °C. Using the shear rheoemeter, at time t = 0 a 184 μm thick layer of the material was subjected to a certain shear stress, at a time ~180 sec the shear stress was dropped to zero, and the shear strain of the layer was measured as a function of time. The values of the shear stress applied between 0 and 180 sec were 4.68 Pa (black dots), 9.16 Pa (orange dots), and 18.7 Pa (blue dots). The segments with the constant non-zero shear stress are well fitted by straight lines with slopes of $0.848 \cdot 10^{-3}$, $1.74 \cdot 10^{-3}$, $3.63 \cdot 10^{-3}$ s^{-1} for stresses of 4.68, 9.16, and 18.7 Pa, respectively. These straight segments, indicating constant shear rates at constant shear stresses, correspond to liquids with viscosities of 5510, 5260, and 5150 Pas, respectively. When the stresses are dropped to zero, the material experiences a minor recoil over ~10 sec, indicating elastic properties, and the deformation remains steady afterwards. Therefore, the overall mechanical response of material corresponds to a viscoelastic fluid with some shear-thinning of viscosity that is typical for polymeric liquids. We note that the viscosity of the material resulting from B:C = 85:1 is ~1000 times greater than of the base component of Sylgard 184 (5.1 Pas according to the manufacturer), suggesting that the addition of the curing agent has caused substantial polymerization, which still has not lead to solidification. (D) Mechanical tests of the material obtained by mixing the components of Sylgard 184 at B:C = 100:1 and curing the mixture overnight in a forced convection oven at 80 °C. Using the shear rheometer, at time t = 0 a 191 μm thick layer of the material was subjected to a certain shear stress, at a time ~180 sec the shear stress was dropped to zero, and the shear strain of the layer was measured as a function of time. The values of the shear stress applied between 0 and 180 sec were 1.75 Pa (black dots), 4.85 Pa (orange dots), and 9.5 Pa (blue dots). The segments with the non-zero shear stress are well fitted by straight lines with slopes of $0.871 \cdot 10^{-3}$, $2.43 \cdot 10^{-3}$, $4.73 \cdot 10^{-3}$ s^{-1} for stresses of 1.75, 4.85, and 9.5 Pa, respectively. These straight segments, indicating constant shear rates at constant shear stresses, correspond to liquids with viscosities of 2010, 2000, and 2000 Pas, respectively. After the stresses are dropped to zero, the shear strain remains constant (apart from a minor instrumental zero drift). Therefore, the overall mechanical response of the 100:1 mixture corresponds to a viscous Newtonian liquid (possible non-Newtonian properties are undetectable in our test) with viscosity ~400 times greater than the viscosity of the base component of Sylgard 184. We finally note that the plot in panels C and D, all representing liquids, are in a stark contrast with the plot in Fig. 4-4H, showing the results of a similar mechanical test performed on a soft solid gel with E = 0.44 kPa. In that last case, the deformation (shear strain) reaches a plateau within a short time after shear stress is increased and fully recoils after the shear stress is reduced to its previous value.

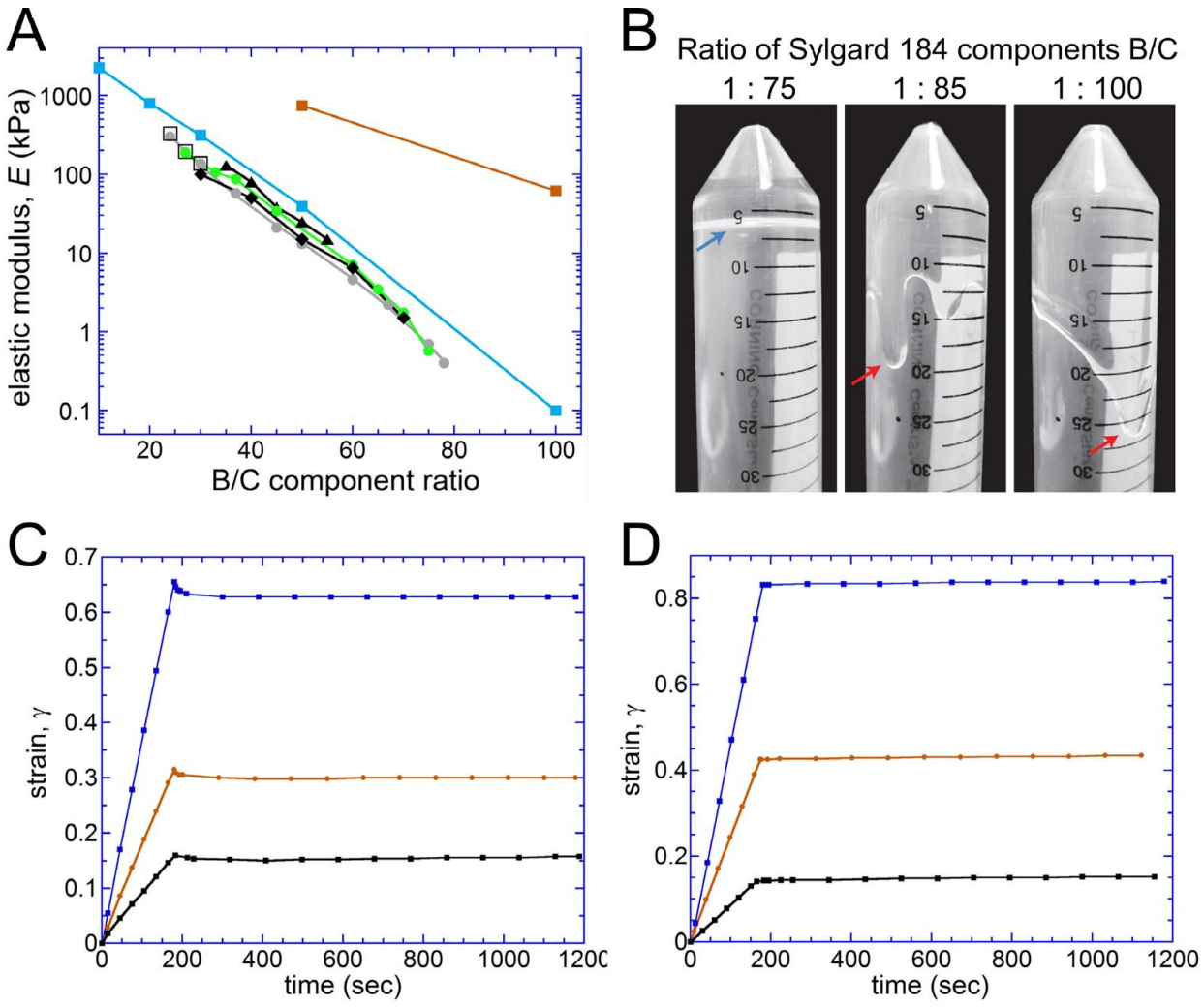
A
elastic modulus, E (kPa)
1000
100
10
1
0.1
20
40
60
80
100
B/C component ratio
B
Ratio of Sylgard 184 components B/C
1 : 75
1 : 85
1 : 100
C
strain, γ
0.7
0.6
0.5
0.4
0.3
0.2
0.1
0
0
200
400
600
800
1000
1200
time (sec)
D
strain, γ
0.8
0.6
0.4
0.2
0
0
200
400
600
800
1000
1200
time (sec)

Figure 4-7: Binding of functionalized beads to silicone gel substrates.
Fluorescence images of 40 nm beads (580nm excitation/605nm emission) on surfaces of silicone substrates with different elastic moduli after the substrates were incubated under bead suspensions for 30 min at room temperature (RT). The beads had amine groups on their surfaces. Two bead suspensions were used with the low-concentration suspension been 1/8 as concentrated as the high-concentration one. In a control experiment with a 64 kPa gel (bottom left), amine-reactive groups were hydrolyzed by incubation under 20 mM HEPES buffer (pH 8) for 30 min at RT before the high-concentration bead suspension was applied for 30 min at RT.

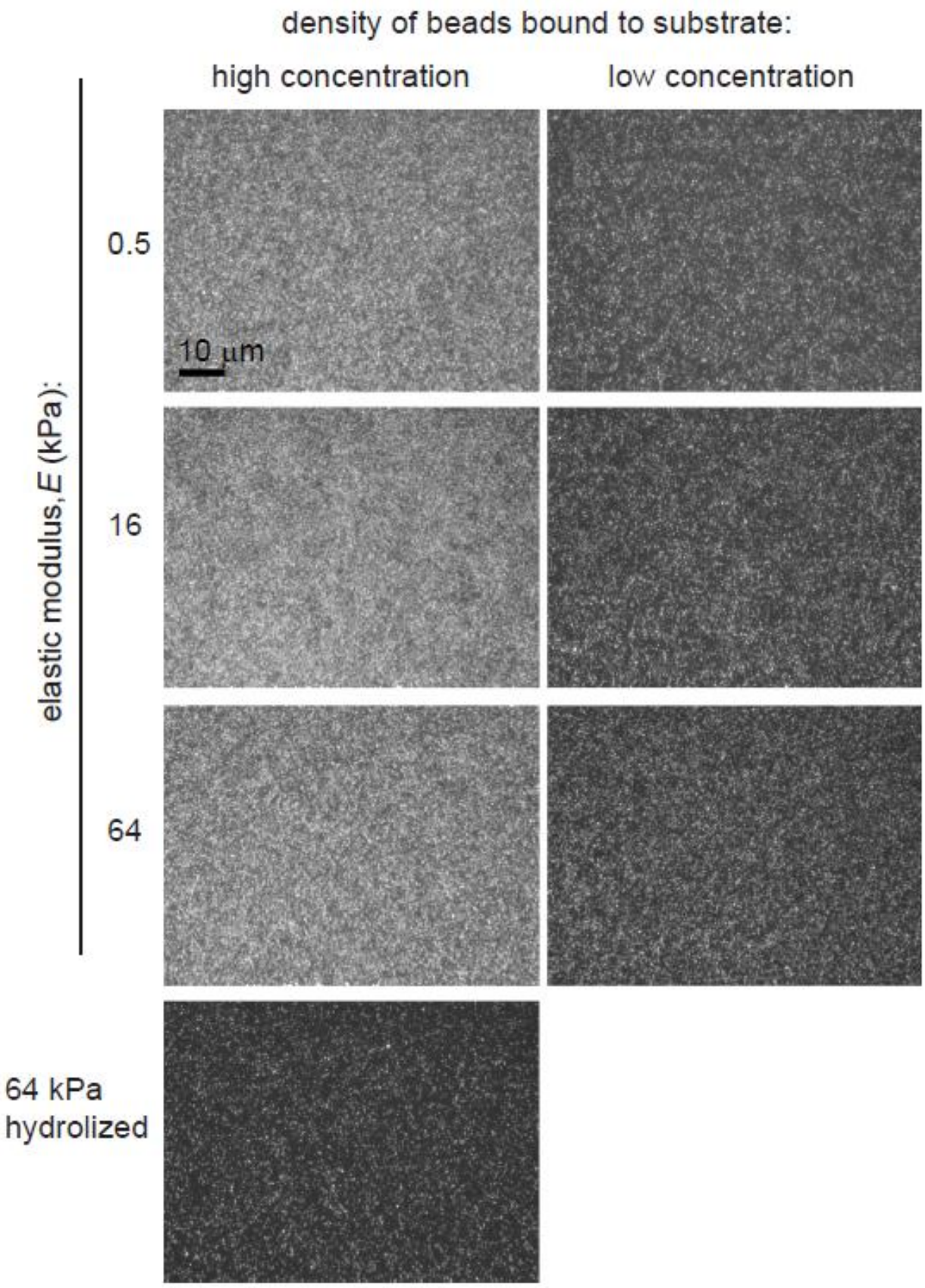
density of beads bound to substrate:
high concentration
low concentration
elastic modulus, E (kPa):
0.5
16
64
10 μm
64 kPa
hydrolized

Chapter 4.1, in full, is a reprint of the journal article “Rigidity of Silicone Substrates Controls Cell Spreading and Stem Cell Differentiation”, Scientific Reports, 2016. Vertelov, Grigory; Gutierrez, Edgar; Lee, Sin-Ae; Ronan, Edward; Groisman, Alex; Tkachenko, Eugene. The dissertation author is a co-author and a leading contributor to the substrate aspect of the experiment in this paper.

Chapter 4.2, in full, is a reprint of the supplementary material of the journal article “Rigidity of Silicone Substrates Controls Cell Spreading and Stem Cell Differentiation”, Scientific Reports, 2016. Vertelov, Grigory; Gutierrez, Edgar; Lee, Sin-Ae; Ronan, Edward; Groisman, Alex; Tkachenko, Eugene. The dissertation author is a co-author and a leading contributor to this work.

5. Mechanics Dictate Where and How Freshwater Planarians Fission

Abstract:

Asexual freshwater planarians reproduce by tearing themselves into two pieces by a process called binary fission. The resulting head and tail pieces regenerate within about a week, forming two new worms. Understanding this process of ripping oneself into two parts poses a challenging biomechanical problem. Because planarians stop "doing it" at the slightest disturbance, this remained a centuries-old puzzle. We focus on Dugesia japonica fission and show that it proceeds in three stages: a local constriction ("waist formation"), pulsation—which increases waist longitudinal stresses—and transverse rupture. We developed a linear mechanical model with a planarian represented by a thin shell. The model fully captures the pulsation dynamics leading to rupture and reproduces empirical time scales and stresses. It asserts that fission execution is a mechanical process. Furthermore, we show that the location of waist formation, and thus fission, is determined by physical constraints. Together, our results demonstrate that where and how a planarian rips itself apart during asexual reproduction can be fully explained through biomechanics.

Introduction:

Michael Faraday and his contemporaries were intrigued by the observation that asexual freshwater planarians, squishy worms a few millimeters in length, reproduced by tearing themselves into a head and tail offspring, in a process called binary fission[1]. How was it possible for these animals to generate the forces necessary to rip themselves using only their own musculature and substrate traction? The question has remained unanswered to this day, because

it is experimentally difficult to study the fission process in sufficient detail to figure out how it works. Planarian fission is fast, violent, and irregular. No induction mechanism has been identified, although decapitation has been shown to increase fission probability[2–4]. Furthermore, planarians are photophobic[5], fission occurs primarily in the dark[4,6], and even slight disturbances cause it to stop, complicating real-time imaging of the process. Finally, in the planarian species most commonly used in stem cell research, fission occurs on average approximately once per month per worm[7] and only lasts from a few minutes to tens of minutes (this study). All these factors make fission dynamics hard to study and rendered it a neglected area of planarian research[8,9], although fission and regeneration are intimately linked[2,3].

The most comprehensive study of fission that we have found in the literature is the 1922 thesis (in French) of Vandel on asexual reproduction of several European Dugesia species[10]. Vandel described fission as spontaneous and fast, varying in duration from seconds to minutes, and regulated but not triggered by environmental factors. He noted that the fission plane is highly variable along the head–tail axis. Furthermore, by observing two consecutive fissions of the same animal, the first occurring close to the head and the second almost at the center, Vandel concluded that it was "impossible to formulate rigorous conclusions. One must limit oneself to giving the general trends and looks of this phenomenon without trying to explain all the observed exceptions" [author translation][10]. Because where along the body axis a planarian divides affects the fitness and reproductive behaviors of its offspring[7,11–13], understanding how fission location is regulated is an important question to be answered. Regarding the division process, Vandel described fission as a mechanical process, whereby the anterior and posterior parts act independently, with the anterior part rhythmically pulsing and the posterior part largely adhering to the substrate.

Here we focus on the biomechanics of fission in the asexual planarian Dugesia japonica. Using time-lapse video recording, statistical analysis, and mathematical modeling, we show that Vandel was right in interpreting fission as a mechanical process, but wrong in declaring the fission location unpredictable. We dealt with the experimental challenges elaborated on above by decapitating specimens to increase fission frequency and recording events over the course of months to obtain data of the necessary quality for quantitative shape analysis. These imaging data were complemented by traction force experiments using special substrates, which were sufficiently soft and stable to allow for these kinds of long-term experiments.

The analysis of 22 fissions made it possible to identify three key stages shared among all events we observed in this species: a local constriction ("waist formation"), pulsation—which increases waist longitudinal stresses—and transverse rupture. As soft-bodied animals, planarians exhibit these body shape changes through the action of perpendicularly oriented, antagonistic muscle groups on weakly compressible internal fluids and tissues, which make up what is called a hydrostatic skeleton (see reviews in refs. 14 and 15). Waist formation is key to successful rupture, because it enhances the longitudinal stresses at a given longitudinal tension force exerted by the planarian's musculature by an order of magnitude.

We found fission to be distinctively different from the three known gaits of planarian locomotion, which are gliding, peristalsis, and scrunching[16]. Thus, fission poses a novel biomechanics scenario and the existing models that describe these planarian gaits are inadequate to describe fission dynamics.

Following D'Arcy W. Thompson's thesis that "in the representation of form and in the comparisons of kindred forms . . . we discern the magnitude and the direction of the forces which have sufficed to convert the one form into the other"[17], we used the analysis of planarian body

shapes to develop an enhanced readability thin-cylindrical-shell model, which fully captures pulsation dynamics leading to rupture and reproduces empirical time scales and stresses. Importantly, the model only uses experimental data and parameters from the literature as inputs. This implies that rupture is a purely mechanical process that can be fully accounted for by physical mechanisms without requiring any additional biological explanations.

Besides solving this centuries-old mystery about the biomechanics of planarian reproduction, this study highlights the power of a practical approach, combining quantitative image analysis and a simple physical model, for gaining insights into a complex biological phenomenon which is not accessible to controlled experimentation and perturbations.

Significance:

How planarians reproduce by ripping themselves into a head and a tail piece, which subsequently regenerate into two new worms, is a centuries-old biomechanics problem. Michael Faraday contemplated how this feat can be achieved in the 1800s, but it remained unanswered because it is experimentally difficult to observe planarians "doing it." We recorded Dugesia japonica planarians in the act and developed a physical model that captures pivotal steps of their reproduction dynamics. The model reproduces experimental time scales and rupture stresses without fit parameters. The key to rupture is a local reduction of the animal's cross-sectional area, which greatly amplifies the stresses exerted by the planarian's musculature and enables rupture at substrate stresses in the pascal range.

Results:

Months of continuous recording of decapitated D. japonica allowed us to capture a sufficient number of fission events occurring in open space for a quantitative study of fission dynamics. Decapitation promotes fission[2–4] without altering its dynamics (Movies S1 and S2) and was thus used as a means to increase the number of events. Qualitative analysis of these timelapse movies indicated that D. japonica fission occurs as a sequence of three distinct stages: waist formation, pulsation, and rupture (Fig. 5-1 and Movie S2). Fission relies on the animal's thin (10 μm) subepidermal muscle network[14], which consists of longitudinal (parallel to the head–tail axis), circular (perpendicular to the head–tail axis), and diagonal muscles (Fig. S1).

Given the muscles' anatomical orientation, the vertico-lateral narrowing which leads to the formation of a waist is mediated by local contractions of circular muscles. Narrowing causes the waist region to lose contact with the substrate, while the body mass is actively redistributed toward the head and tail, leading to the formation of broad regions of contact with the substrate (Fig. 5-1B).

Next, the pulsation stage starts, as the planarian lifts its head (whenever we use the term "head," we refer to the region anterior to the waist. The true head was amputated in our experiments as indicated in Fig. 5-1A and described in Materials and Methods) from the substrate (Fig. 5-1C), and "flesh waves," axially propagating lateral indentations of the worm head, are produced by contractions of circular muscle fibers. It appears that the generation of these waves is facilitated by the lack of contact (and, hence, of friction) between the lifted head and the substrate. As the planarian body is nearly incompressible (hydrostatic skeleton), these radial contractions produce longitudinal head extension and stresses in the waist. To return to its original shape the planarian then contracts its longitudinal muscles. Stresses in the waist are

largest during the relaxation phase (contraction) of the head. When the longitudinal stress in the waist exceeds a critical value, rupture occurs (Fig. 5-1D) and the worm flesh rips into head and tail pieces, concluding the fission. The two offspring regenerate into whole planarians in roughly a week.

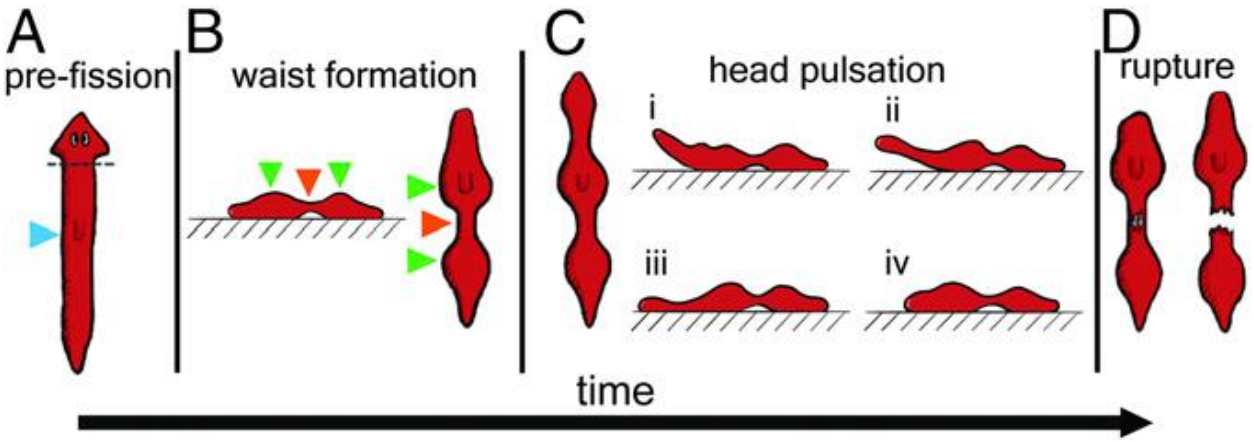

Figure 5-1: Cartoon of D. japonica fission.
Cartoon of D. japonica fission. (A) Unperturbed planarian before fission. The pharynx is marked by the blue arrowhead. To increase the fission rate (3), we amputate as indicated by the gray line. (B) Waist formation. Tissue movement causes local narrowing (orange arrowhead) and formation of wide contact regions at the head and tail (green arrowheads). The waist is not in contact with the surface. (C) The head lifts off the substrate during pulsation and then readheres and slides back against the surface. (D) Rupture.

As the cartoon (Fig. 5-1) illustrates, fission dynamics are fairly complex. We first discuss where the waist forms. Then, we show how body shape analysis allows construction of a simple physical model that explains how pulsation can lead to rupture and estimate the magnitude of the rupture stresses.

Location of Waist Formation

Vandel[10] observed that an individual planarian divided at different locations when followed through consecutive fissions, which led him to the conclusion that the fission plane cannot be predicted. Because he did not study D. japonica, we checked whether this observation

held equally true in this species. Indeed, as illustrated by the examples in Fig. 5-2A, the fission location varies and it is seemingly impossible to predict where an individual planarian fissions (note that the dynamics of these fission events were not recorded).

We then took advantage of a unique large-scale dataset on the birth and division sizes, growth curves, and time between fissions (reproductive waiting time, RWT) we had accumulated on D. japonica[18] and applied statistical analysis to assay whether those data would provide further insight. We found an asymmetric double-Gaussian distribution for the waist location based on imaging n = 1,335 specimens within 3 d after fission (Fig. 5-2B and Materials and Methods). Of note, the area of low fission probability between the peaks, as determined by manual inspection of a subpopulation of n = 40 specimens, coincides with the location of the pharynx, which is a powerful muscle used to ingest food[19]. Thus, planarians divide neither at a pole nor at the pharynx but have a nonzero probability of dividing anywhere else along the head–tail axis, with the majority of events happening posterior to the pharynx. This distribution of waist position also explains why planarian fission is generally reported in the literature as occurring posterior to the pharynx[20–22].

Whether a planarian divides pre- or postpharynx has a significant effect on its offspring, because it determines birth size and thus offspring survival and reproductive success[7]. We therefore binarized the data in Fig. 5-2B into pre- (%H < 0.56) versus postpharynx (%H ≥ 0.56) fissions and correlated it with other known quantities about the properties and history of these worms. While the following arguments hold true for all D. japonica, we only discuss individuals originating from a head offspring below, because prepharynx fissions are negligible for planarians that originate from tails (<<1%).

We found a strong correlation between a planarian's RWT and fission location (Fig. 5-2C), whereas the planarian's size at division had no effect (Fig. S2). Nearly all prepharynx fissions resulted from worms with short RWTs (<2 wk; Fig. 5-2C). Upon inspection of the physical characteristics of these planarians, we found that we can predict where (either pre- or postpharyngeally) an individual D. japonica will divide through quantification of its relative pharynx position (Fig. 5-2D). Fission occurs anterior to the pharynx when the pharynx is located relatively closer to the tail (Fig. 5-2D). This is frequently the case for animals with short RWTs (Fig. S2). A comparison of pharynx positions at birth and at division of pre- and postpharyngeal dividers shows that the former have not repositioned their pharynx sufficiently to allow for a postpharyngeal fission. Because repositioning takes time, this can explain why we primarily observe prepharynx divisions in rapid dividers.

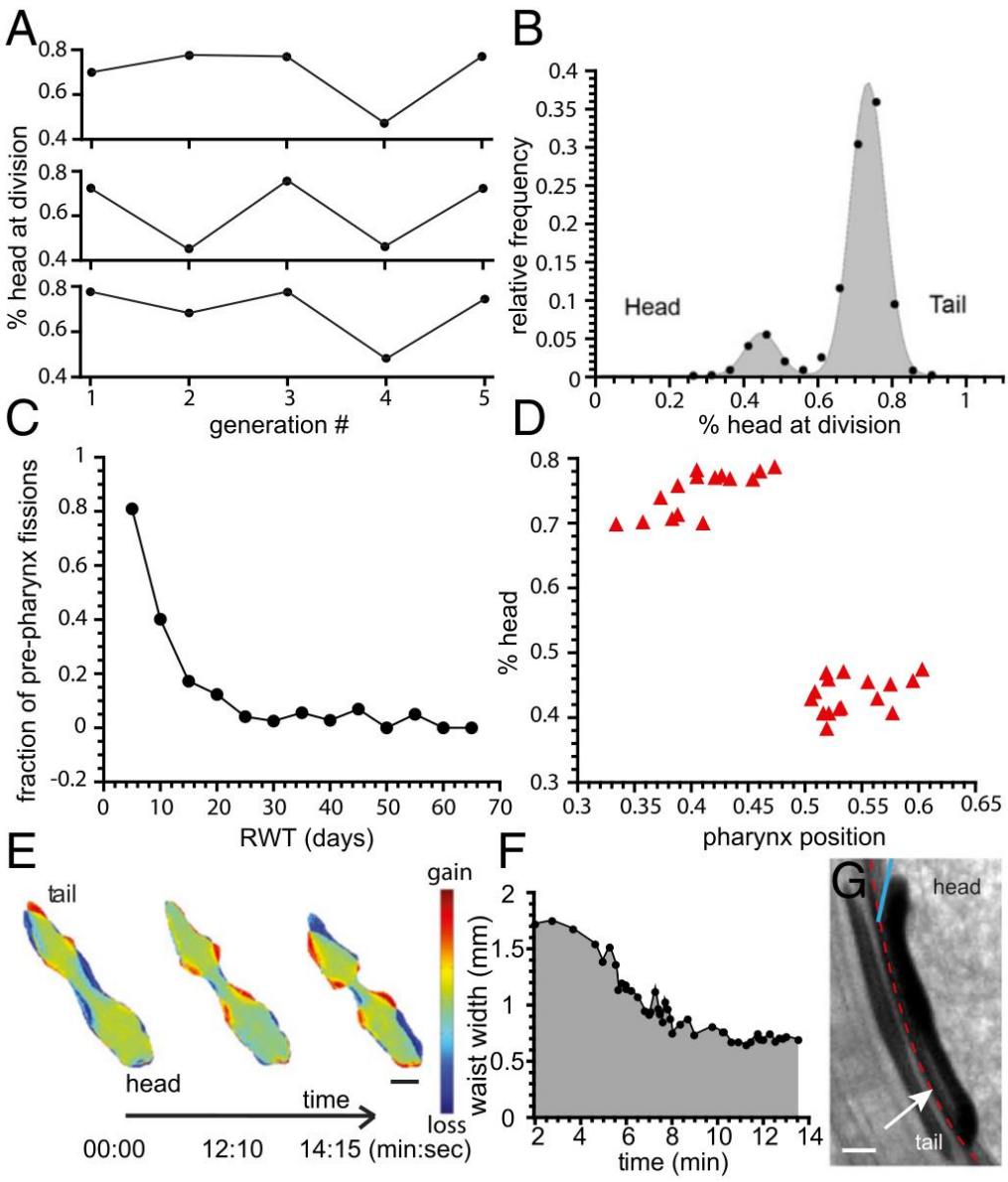

Figure 5-2: Waist formation.
(A) The waist position along the head–tail axis is not conserved across generations for a single planarian line. (B) Frequency of occurrence of waist position, expressed as percentage head at division (n = 1,335). (C) Quantification of the fraction of prepharynx fissions as a function of RWT. (D) Quantification of percentage head at division as a function of relative pharynx position shows that the latter predicts fission position. (E) Color-coded maps of worm footprint, showing a representative sequence of waist formation in an amputated planarian. Colors indicate the change in the mass per unit area, with green corresponding to no change, blue to loss,
and red to gain of mass. (Scale bar: 1 mm.) (F) The width of the waist region versus time in E. (G) Side view image of a planarian undergoing fission. The dashed red line outlines the Petri dish wall. The white arrow highlights a gap between the waist of the worm and the substrate. The blue line indicates the angle by which the planarian lifts its head before pulsation. (Scale bar: 1 mm.)

We can explain why pharynx position matters with biomechanical arguments. To pull itself apart, a planarian needs to form two sufficiently large contact regions (adhesion patches) with the substrate. If the pharynx is located close to the tail end, the posterior part of the animal is too small to accommodate the adhesion patches and fission occurs anterior to the pharynx (Fig. S2). Because the size of these patches scales with worm size (Fig. S2), absolute worm size does not matter.

To summarize, our statistical analysis shows that it is possible to predict whether a particular D. japonica planarian will fission pre- or postpharynx, solely through quantification of its relative pharynx position.

Mechanism of Waist Formation

Waist formation, which is a local narrowing in the vertical and lateral directions, is achieved by contractions of circular muscles. Peristaltic contractions move mass from the waist region toward the head and tail (Fig. 5-2 E and F, Fig. S3 A and B, and Movie S3). As a result of this mass redistribution, the area of contact with the substrate on either side of the waist increases, whereas the waist part of the worm body detaches from the substrate (Fig. 5-2G and Movie S4). Waistformation is critical for successful fission. It has the physiological benefit of preventing gut spillage during the subsequent rupture. Not less importantly, for a given longitudinal tension force, the reduction in the worm cross-section in the waist region leads to a proportional amplification of the longitudinal tensile stress. That said, the waist diameter is anatomically constrained and scales with the initial width of the worm (Fig. S4 and SI Text). This scaling indicates the existence of a mechanism preventing the formation of waists that are too narrow. Experimentally, we found that the ratio of cross-sections of the head, Ahead, and of

the waist, Awaist, is limited by ∼14, suggesting that the tensile stress at the waist can be amplified by a factor of up to ∼14, compared with the characteristic traction stress in the head (or the tail) (Fig. S4 and SI Text).

Pulsations

Once the waist is formed, pulsations begin, that is, the planarian executes multiple longitudinal extensions and contractions of the head and/or tail parts of its body (Fig. 5-3 A–C, Fig. S3 C and D, and Movies S5 and S6). On average, head pulses occur more frequently than tail pulses (89 head pulses versus 19 tail pulses total for n = 22 fissions), suggesting that head pulses are critical for generating tensile stresses causing the rupture in the waist region. Notably, head and tail pulses were asynchronous and we never observed a "tug-of-war" between them.

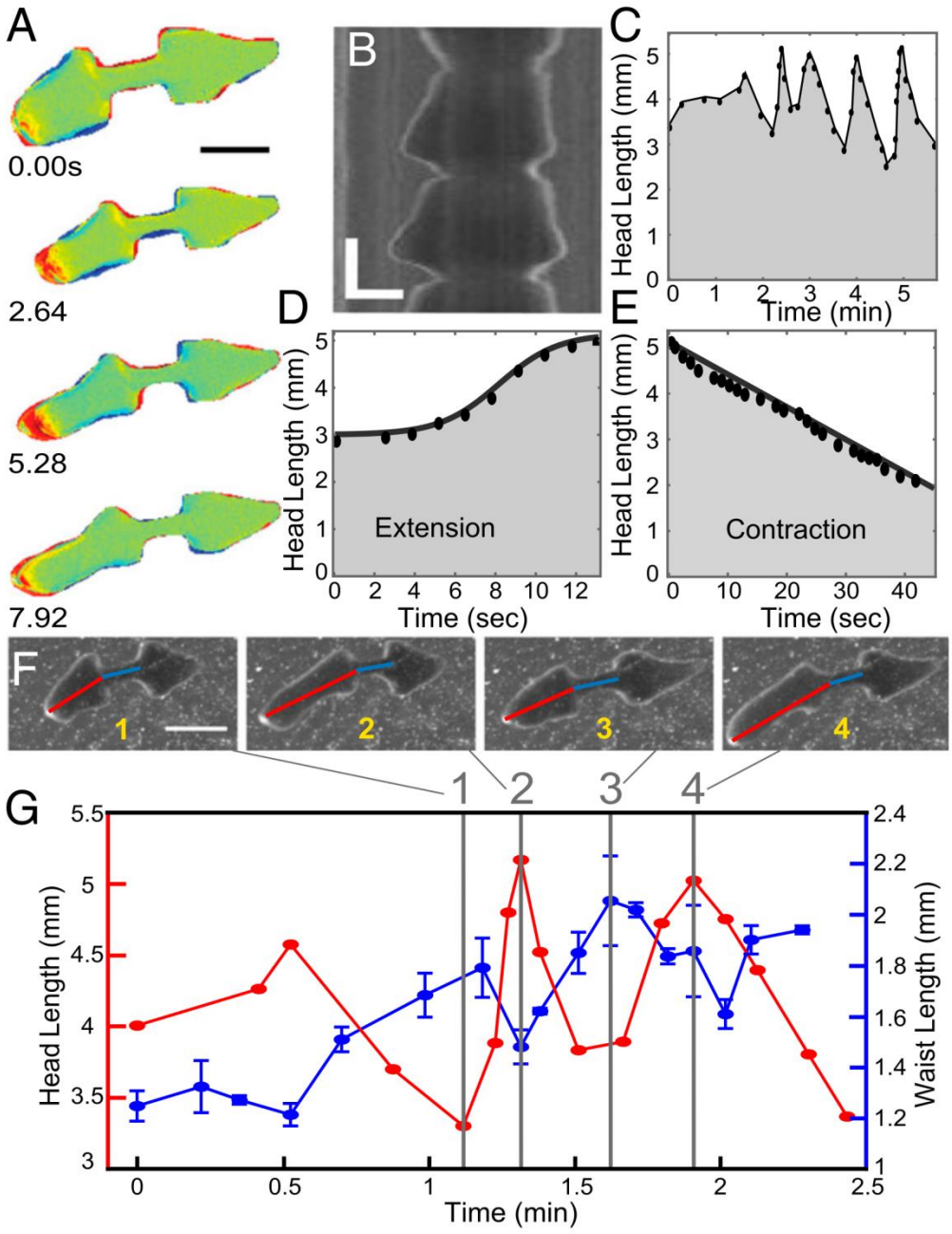

Figure 5-3: Pulsation.
(A) Representative sequence of head pulsation of an amputated planarian. Color coding is the same as in Fig. 5-2. (Scale bar: 3 mm.) (B) Kymograph showing multiple head pulses. (Vertical scale bar: 20 s; horizontal scale bar: 1 mm.) (C). Head length as a function of time during a series of head pulsations. (D) Head extension is logistic and fast, whereas (E) head contraction is linear and slow. (F and G) Head and waist lengths are anticorrelated. (F) Consecutive images of a planarian with its head and waist lengths shown by red and blue lines, respectively. (Scale bar: 3 mm.) (G) Time dependences of head length and waist length of the planarian from the images in F.

At the beginning of each head pulse, the anterior of the head detaches from the substrate (Fig. 5-2G, Fig. S5, and Movies S4 andS7). The detachment allows the head to break out of the mucus layer (Figs. S5 and S6 and SI Text), minimizing friction with the substrate during head extension. Circular muscle contractions then elongate the head (Fig. 5-3D and Fig. S3). This is a necessity of the planarian's hydrostatic skeleton: If a worm elongates, while both its width and height decrease, it can only be a result of contraction of the circular muscles. The head reattaches to the substrate and slowly contracts. Head contraction is achieved by shortening of the worm's longitudinal muscles and resisted by friction with the substrate (Fig. 5-3E). These different dynamics are clearly seen in Fig. 5-3 D and E), where head length during pulsation increases logistically (S shape in Fig. 5-3D) but decreases linearly with time. Importantly, head and waist dynamics are anticorrelated. As the head extends, the waist gets compressed and buckles (Movies S5 and S6). As the head contracts, the waist region gets stretched (Fig. 5-3 F and G).

The maintenance of proper adhesion with the substrate is crucial during this stage. We observed some animals slipping during pulsation (Fig. S6) and interpret this as resulting from weak adhesion with the substrate, leading to poor stress transmission to the waist. In accordance with this interpretation, animals that slip execute more pulsations before rupture. Interestingly, the number of pulses was weakly anticorrelated with a planarian's size, suggesting that the absolute size matters for successful fission (Fig. S6). In other situations where substrate adhesion is critical, we and others have shown that an increase in mucus secretion is key[16, 23]. To directly prove the link between a planarian's mucus secretion and adhesion, we treated planarians with Triton X-100, which increased mucus secretion (Fig. S6). Using a custom aspiration setup, we then quantified the aspiration force required to detach worms from their substrate. Triton X-100–exposed planarians required larger aspiration forces than control planarians (Fig. S6). Based on

these data, we postulate that substrate adhesion during fission is mediated through the increased presence of mucus.

Rupture

The ultimate and key step in fission is successful rupture (Fig. 5-4A). Rupture occurs when the stress in the waist, induced by contraction of the head, exceeds a critical threshold (Fig. S4E). In most cases (20/22 fissions; Materials and Methods and Movie S8), rupture is nucleated at the center of the waist region. We measured the stresses exerted on the substrate during fission using traction force measurements (Fig. 5-4B). To this end, we fabricated thick (~5 mm), soft (Young's modulus E = 1.2 kPa) silicone gel substrates with 30- to 45-μm-diameter beads imbedded in an ~70-μm-thick surface layer as the tracer particles (SI Materials and Methods). A map of displacements of the beads from their zerostress locations (when the substrate was not deformed by the worm) was generated and converted into a map of traction stresses using previously published algorithms[24] (SI Materials and Methods). The stresses were on the order of 100 Pa (Fig. 5-4B).

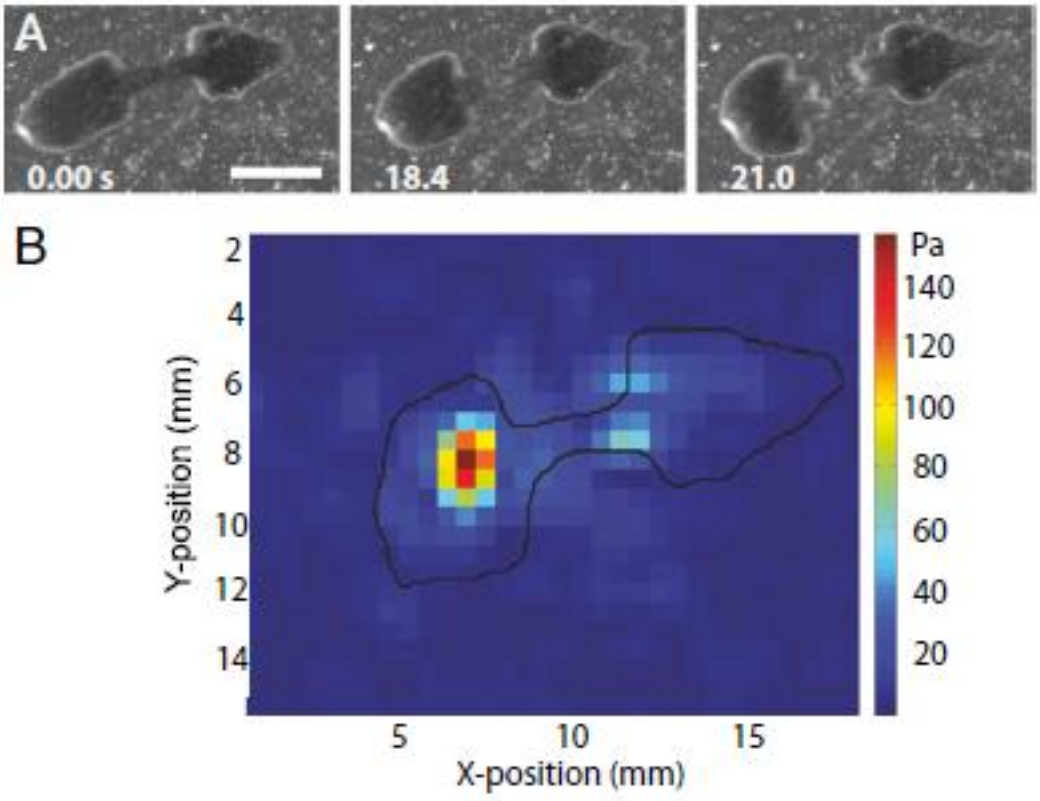

Figure 5-4: Rupture.
(A) Image sequence of a worm rupturing. (Scale bar: 2 mm.) (B) Color-codedmap of the substrate traction stresses produced by a D. japonica (contour in black) a short time before rupture.

Projection of the stresses on the axis of the worm (direction along the waist) was then integrated over the areas of the head and of the tail, providing the pair of opposing traction forces that stretch the waist. The stretching force before rupture was a few hundred micronewtons and, when divided by the cross-sectional area of the waist, it provided an estimate of ~2,000 Pa for the tensile stress in the waist immediately before rupture. Once rupture is completed, the two offspring move independently and regenerate into new full worms within about a week.

A comparison of the fission dynamics of events on soft polydimethylsiloxane gels versus plastic Petri dishes revealed no significant differences in terms of the number of pulses (Fig. S6), suggesting that the interaction with the mucus dominates substrate effects on fission.

It is evident from this quantitative analysis that fission dynamics have little in common with normal planarian locomotion via cilia-based gliding, which does not involve body shape changes[16]. There are some similarities between fission and the two muscle-based planarian gaits, peristalsis and scrunching[16,23], insofar as all involve body elongation–contraction cycles and require good contact with the substrate for successful execution. However, fission pulsation dynamics are different from those observed in peristalsis or scrunching, which either show no asymmetry or relatively longer elongation periods, respectively. Finally, waist formation is a unique feature of fission. Because of these differences, existing models for these gaits fail to reproduce the observed fission dynamics.

Therefore, we developed a linear mechanical model with the planarian head represented by a thin, cylindrical, elastic shell (corresponding to the thin musculature network) filled with a viscous liquid (corresponding to coarse-grained, squishy internal tissue). The same model could be applied to the tail part on the other side of the waist, but we focus on the head because tail pulsations do not occur in all fission events. Although the deformations during fission are large, this linear thin-shell model allows us to capture pulsation and rupture dynamics using only physical arguments and scaling estimates.

Physical Model

We treat the head as a uniform, long, thin, cylindrical, elastic shell of cross-sectional radius R, Young's modulus E, and shell thickness h which encloses material of density ρ (Fig. S1). Although planarians, being flatworms, have elliptical cross-sectional areas, the simplification to circular cross-sectional areas has a negligible effect on the results (SI Text). We assume that the head is connected to the waist by an impermeable junction, through which no

matter crosses on the time scale of pulsations (Fig. S1). This assumption is reasonable, as the data show no material transfer once the waist has been established (Movies S4 and S5). The long-thin approximation applies, since L_{head} ~4 mm while R_{head} ~ 1.2 mm.

A thin, cylindrical, elastic shell supports three modes of waves: longitudinal, flexural, and torsional. The last ones can be ignored as there is no indication that the planarian twists during pulsation. Longitudinal wave displacements on an elastic cylinder are predominantly axial while flexural (F)-waves support primarily radial (lateral) displacements. These two modes are linearly coupled at finite Poisson ratio (Eqs. S1–S3).

The experimentally observed flesh waves correspond to F-waves. They are initiated by contractions of circular muscles in the head part anterior to the substrate contact region, causing local changes in the radius. The head anterior is detached from the substrate during extension and therefore has no friction with it. The deformation propagates longitudinally at the group velocity of F-waves. As the wave progresses anteriorly the head extends forward due to volume conservation. Simultaneously, the wave propagates in the head posterior toward the waist region and because the head–waist connection is impermeable the waist region experiences a compression and buckles. Thus, qualitatively, the model predicts the observed anticorrelation of head and waist length during head extension. Furthermore, we can compare the F-wave group velocity with the observed flesh pulse speed (see SI Text for calculations). Using only experimentally measured values of the parameters, we calculate that the F-wave propagates at $v_{vg} = 1.4$ mm/s. This is in excellent agreement with the observed flesh pulse speed of $v_{ext} = 1.1 \pm 0.4$ mm/s (mean ± SE; n= 16). Our model thus properly captures the dynamics of head extension during pulsations.

Regarding the head contraction phase, the main difference to extension is that the head anterior is now in contact with the substrate and thus friction needs to be taken into account. Head contraction dynamics are determined by this competition between muscular relaxation and friction with the substrate as inertial forces can be neglected. The balance of these two forces defines a relaxation time scale (SI Text):

$$\tau_{relax} \cong \eta_{mucus} A_{contact} L_{head}^2 / V_{head} E h_{mucus} \qquad 5\text{-}1$$

All values in Eq. 5-1 were experimentally determined, with $h_{mucus} = 10$ μm the height of the mucus layer, $\eta_{mucus} = 65$ Pa · s the mucus viscosity, $A_{contact} = 8.7$ mm^2 the surface area of contact with the substrate, E= 500 Pa the elastic modulus of the shell, $V_{head} = 22$ mm^3 the head volume, and $L_{head} = 4$ mm the length of the head (Table S1). Using these values gives $\tau_{relax} \cong 82$ s, which is in reasonable agreement with the experimental value of the relaxation time $\tau = 44 \pm 20$ s (mean ± SE; n= 18).

Taken together, pulsation time scales are well captured by the linear model, both during elongation and contraction phases, although it is too simple to reproduce the trajectory of pulsations (logistic during elongation and linear during contraction). Head extension is quick, whereas head contraction is slow and thus allows for the buildup of stresses in the waist required for rupture. The model correctly predicts that head extension and waist extension are anticorrelated (Fig. S1), consistent with experimental observations (Fig. 5-3 F and G). During head extension, the waist appears shorter, because it bends vertically (Fig. 5-3 F and G and Movies S4 and S5), whereas during head contraction the waist is extended (Fig. 5-3 F and G) and thus under increased longitudinal stresses. Once these stresses exceed the tissue's yield, rupture occurs. We estimate this critical stress necessary for rupture (SI Text) using a linear

approach and experimentally determined parameters only (Table S1) and obtain $\sigma_{waist} \approx 3{,}000$ Pa, which is in reasonable agreement with our traction force measurements.

Magnitude of Rupture Stresses

The rupture stresses we found are in the kilopascal range, which is orders of magnitude lower than stresses previously reported for rupture of tissues in other animals[25, 26]. It is possible that biological processes preceding or accompanying waist formation weaken the waist and lower the required rupture stresses. The idea of a predefined "fission zone," with metabolic, cellular, or structural differences compared with the rest of the worm, was already suggested over 50 years ago by Child[27] and Tokin (reviewed in refs. 2 and 28). Hori and Kishida[3] performed structural analysis of the postpharyngeal region and observed "presumptive changes in preparation for fissioning" in some, but not all, of the samples. Because these samples were fixed planarians without a waist, it is impossible to tell if fission would have occurred in the studied region. Thus, experimental evidence demonstrating the existence of a fission zone is absent. Our data on the distribution of the waist location argue against a permanent fission zone but allow for the possibility that the animal locally prepares for fission before each event (e.g., via enzymatic digestion of extracellular matrix components by metalloproteinases, which have been shown to play a role in planarian tissue homeostasis and regeneration)[29, 30].

To test whether such weakening of the fission zone was necessary, we measured the stresses needed to rip a nondividing planarian apart by applying suction to both ends of a planarian using pipette tips connected to a peristaltic pump (Fig. 5-5A and Materials and Methods). In this experiment (Fig. 5-5B), a waist was not formed and the time to rupture was much shorter (seconds compared with minutes in fission), rendering biochemically induced

structural changes unlikely. However, this pulling experiment yielded stresses comparable to those obtained in our traction force measurements, with values ranging between 7.0 kPa and 13.1 kPa. Additionally, we quantified where the worms ruptured and contrasted these measurements with the fission data (Fig. 5-5C). As expected, pulled planarians could tear anywhere along the head–tail axis, including at locations which are "forbidden" zones in fission, such as the very anterior or posterior regions of the animal.

We also estimated the stresses required to crush a planarian by adding a small weight onto its trunk region (Fig. S5 and SI Text). Worms were crushed by a 5-g weight with a contact area of 8.9 mm^2, thus exerting a stress of $\sigma = F/A = 5.6$ kPa. The results of these both tests indicate that stresses of a few kilopascals are sufficient to rupture a planarian.

Together, these data show that rupture during fission can be achieved through the planarian's mechanical properties and the physical mechanisms of pulsations and does not require enzymatic weakening. The planarian's "trick" of progressive necking is key to successful fission. Once rupture is initiated at these relatively low stresses of a few kilopascals, the cross-sectional area of the waist decreases further and the internal stresses increase accordingly.We found that the nerve cords break last during fission (Fig. S7). Because their diameter is only 50 μm (Fig. S7), this implies stresses in the megapascal range, similar to what has been reported as the tensile strength limit for nerve tissues in other organisms[25, 31].

Discussion and Conclusions:

As an active, living biomaterial, D. japonica planarians are able to coordinate and execute their own dissection. Our results demonstrate how they can develop sufficiently large tensile stresses to tear themselves apart. Because D. japonica are soft and squishy[32]—with an elastic

modulus 1,000 times smaller than that of nematodes[16,33]—they are able to tear themselves apart using only substrate adhesion and their own musculature. The self-inflicted rupture is facilitated by the formation of a narrow waist, where tensile stresses are amplified due to reduced cross-sectional area. Friction with the substrate, the mucus rheology, and the planarian's elastic modulus are key parameters in determining the dynamics of the contraction phase and, ultimately, rupture. The planarian only needs to exert sufficiently large stresses to break the weakest structures. Once tearing is initiated, the waist cross-sectional area decreases further and tensile stresses are greatly amplified, resulting in stresses able to break stronger anatomical features such as the muscles or nerve cords. From a biomechanical standpoint one could argue that planarians fission because they are soft and thus can do it. However, that's only one part of the story. Planarians fission because they have stem cells which allow them to regenerate the missing structures after the act. Fission is the sole mode of reproduction of the asexual planarians studied here, which poses the question of how this species creates population diversity. Where a planarian divides affects the fitness and reproductive behaviors of its offspring[7,11–13]. Therefore, understanding how fission location is regulated is an important evolutionary question to be answered.

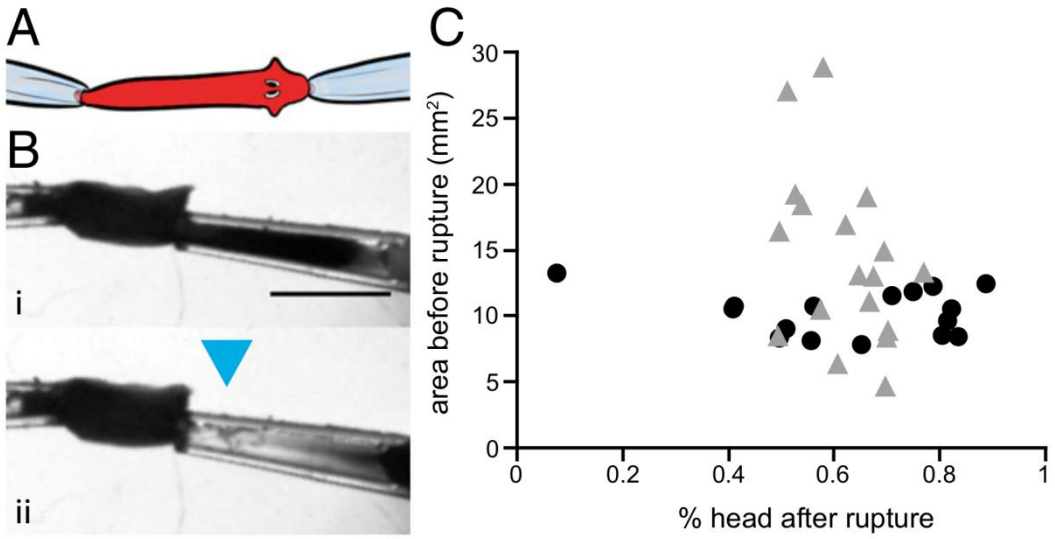

Figure 5-5: Magnitude of rupture stresses.
(A) Schematic of the planarian pulling experiment. (B) Representative image of a pulled planarian. (B, i) right before and (B, ii) right after rupture. (C) Distributions of rupture planes in fission (black circles, n = 22) and pulling (gray triangles, n = 16) experiments.

We showed that the waist and thus the fission location is determined through the relative position of the pharynx. Animals with short RWTs have less time to reposition their pharynx following the previous fission and thus mechanically cannot divide postpharyngeally, frequently resulting in large tails. What causes some animals to divide rapidly, whereas other comparably sized animals take a long time, remains unknown. However, now that we can predict where an individual will divide, we can start to dissect whether molecular differences exist between pre- and postpharynx dividers, which could provide insights into the mechanisms controlling RWT and, if existent, a fission trigger.

Finally, going beyond planarian reproduction, this study shows how one can gain insights into complex animal behaviors that are difficult to access experimentally, simply by "watching." Quantitative image analysis allows for the construction of simple physical models which can then be tested against the empirical data, potentially revealing new regulatory mechanisms.

Chapter 5, in full, is a reprint of the journal article “Mechanics Dictate Where and How Freshwater Planarians Fission”, PNAS, 2017. Malinowski, Paul T.; Cochet-Escartin, Olivier; Kaj. Kelson J.; Ronan, Edward; Groisman, Alexander; Diamond, Patrick H.; Collins, Eva-Maria S. The dissertation author is a co-author and a leading contributor to the substrate aspect of the experiment in this paper.

REFERENCES

Chapter 1

1. G.M. Whitesides, Nature **442**, 368 (2006).

2. L. Mazutis, J. Gilbert, W.L. Ung, D.A. Weitz, A.D. Griffiths, and J.A. Heyman, Nat. Protoc. **8**, 870 (2013).

3. D.N. Gosalia and S.L. Diamond, Proc Natl Acad Sci USA **100**, 8721 (2003).

4. D.R. Gossett, W.M. Weaver, A.J. Mach, S.C. Hur, H.T.K. Tse, W. Lee, H. Amini, and D. Di Carlo, Anal. Bioanal. Chem. **397**, 3249 (2010).

5. H. Bruus, Theoretical Microfluidics (Oxford University Press, New York, 2008).

Chapter 2

1. C.L.J. Marcinko, S.C. Painter, A.P. Martin, and J.T. Allen, Progress In Oceanography **109**, 117 (2013).

2. W.E. Esaias and H.C. Curl, Limnol. Oceanogr. **17**, 901 (1972).

3. H.H. White, J. Exp. Mar. Bio. Ecol. **36**, 217 (1979).

4. E. Buskey, L. Mills, and E. Swift, Limnol. Oceanogr. **28**, 575 (1983).

5. E.J. Buskey and E. Swift, Biol Bull **168**, 263 (1985).

6. A.F. Mesinger and J.F. Case, Mar. Biol. **112**, 207 (1992).

7. M.V. Abrahams and L.D. Townsend, Ecology **74**, 258 (1993).

8. K.J. Fleisher and J.F. Case, Biol Bull **189**, 263 (1995).

9. K.D. Cusick and E.A. Widder, BMS **90**, 797 (2014).

10. J. Morin, **33**, 787 (1983).

11. M.I. Latz, J. Plankton Res. **26**, 1529 (2004).

12. P. von Dassow, R.N. Bearon, and M.I. Latz, Limnol. Oceanogr. **50**, 607 (2005).

13. M.I. Lutz, J.F. Case, and R.L. Gran, Limnol. Oceanogr. **39**, 1424 (1994).

14. E.S. Hobson, Nature **210**, 326 (1966).

15. J. Rohr, M.I. Latz, S. Fallon, J.C. Nauen, and E. Hendricks, J. Exp. Biol. **201**, 1447 (1998).

16. J. Rohr, M. Hyman, S. Fallon, and M.I. Latz, Deep Sea Research Part I: Oceanographic Research Papers **49**, 2009 (2002).

17. S.K. Mallipattu, M.A. Haidekker, P. Von Dassow, M.I. Latz, and J.A. Frangos, J. Comp. Physiol. A, Neuroethol. Sens. Neural Behav. Physiol. **188**, 409 (2002).

18. A.K. Chen, M.I. Latz, P. Sobolewski, and J.A. Frangos, Am. J. Physiol. Regul. Integr. Comp. Physiol. **292**, R2020 (2007).

19. J.B. Lindström, N.T. Pierce, and M.I. Latz, Biol Bull **233**, 151 (2017).

20. P. von Dassow and M.I. Latz, J. Exp. Biol. **205**, 2971 (2002).

21. E.A. Widder and J.F. Case, (n.d.).

22. T. Nawata and T. Sibaoka, J. Comp. Physiol. **134**, 137 (1979).

23. C.H. Johnson, S. Inoué, A. Flint, and J.W. Hastings, J. Cell Biol. **100,** 1435 (1985).

24. J. Woodland Hastings and J.C. Dunlap, in Bioluminescence and Chemiluminescence Part B (Elsevier, 1986), pp. 307–327.

25. M. Fogel and J.W. Hastings, Arch. Biochem. Biophys. **142**, 310 (1971).

26. C.J. Walsh, Eur. J. Cell Biol. **86**, 85 (2007).

27. K. Heimann, P.L. Klerks, and K.H. Hasenstein, Botanica Marina **52**, (2009).

28. A.-S. Cussatlegras and P. Le Gal, J. Exp. Mar. Bio. Ecol. **310**, 227 (2004).

29. M.I. Latz and J. Rohr, Limnol. Oceanogr. **44**, 1423 (1999).

30. S. Blaser, F. Kurisu, H. Satoh, and T. Mino, Luminescence **17**, 370 (2002).

31. R. Eckert and T. Sibaoka, J. Gen. Physiol. **52**, 258 (1968).

32. B. Tesson and M.I. Latz, Biophys. J. **108**, 1341 (2015).

33. M.I. Latz, M. Bovard, V. VanDelinder, E. Segre, J. Rohr, and A. Groisman, J. Exp. Biol. **211**, 2865 (2008).

34. Kamykowski, Reed, and Kirkpatrick, (n.d.).

35. C. Coufort and A. Line, Chemical Engineering Research and Design **81**, 1206 (2003).

36. M.I. Latz, A.R. Juhl, A.M. Ahmed, S.E. Elghobashi, and J. Rohr, J. Exp. Biol. **207**, 1941 (2004).

37. E.M. Maldonado and M.I. Latz, Biol Bull **212**, 242 (2007).

38. A.S. Cussatlegras and P. Le Gal, Nonlinear Process. Geophys. **12**, 337 (2005).

39. A.-S. Cussatlegras and P. Le Gal, **343**, 74 (2007).

40. C. Simonnet and A. Groisman, Anal. Chem. **78**, 5653 (2006).

Chapter 3

1. S. Nemir and J.L. West, Ann. Biomed. Eng. **38**, 2 (2010).

2. G. Vertelov, E. Gutierrez, S.-A. Lee, E. Ronan, A. Groisman, and E. Tkachenko, Sci. Rep. **6**, 33411 (2016).

3. D.E. Ingber and J. Folkman, J. Cell Biol. **109**, 317 (1989).

4. G.C. Reilly and A.J. Engler, J. Biomech. **43**, 55 (2010).

5. A.J. Engler, S. Sen, H.L. Sweeney, and D.E. Discher, Cell **126**, 677 (2006).

6. B.C. Isenberg, P.A. Dimilla, M. Walker, S. Kim, and J.Y. Wong, Biophys. J. **97**, 1313 (2009).

7. B.J. Dubin-Thaler, J.M. Hofman, Y. Cai, H. Xenias, I. Spielman, A.V. Shneidman, L.A. David, H.-G. Döbereiner, C.H. Wiggins, and M.P. Sheetz, PLoS One **3**, e3735 (2008).

8. M.H. Zaman, L.M. Trapani, A.L. Sieminski, D. Mackellar, H. Gong, R.D. Kamm, A. Wells, D.A. Lauffenburger, and P. Matsudaira, Proc. Natl. Acad. Sci. USA **103**, 10889 (2006).

9. D. Krndija, H. Schmid, J.L. Eismann, U. Lother, G. Adler, F. Oswald, T. Seufferlein, and G. von Wichert, Oncogene **29**, 2724 (2010).

10. S. Munevar, Y. Wang, and M. Dembo, Biophys. J. **80**, 1744 (2001).

11. R.J. Pelham and Y. l Wang, Proc. Natl. Acad. Sci. USA **94**, 13661 (1997).

12. A.K. Harris, D. Stopak, and P. Wild, Nature **290**, 249 (1981).

13. K. Burton and D.L. Taylor, Nature **385**, 450 (1997).

14. N.Q. Balaban, U.S. Schwarz, D. Riveline, P. Goichberg, G. Tzur, I. Sabanay, D. Mahalu, S. Safran, A. Bershadsky, L. Addadi, and B. Geiger, Nat. Cell Biol. **3**, 466 (2001).

15. U.S. Schwarz, N.Q. Balaban, D. Riveline, A. Bershadsky, B. Geiger, and S.A. Safran, Biophys. J. **83**, 1380 (2002).

16. C.M. Cesa, N. Kirchgessner, D. Mayer, U.S. Schwarz, B. Hoffmann, and R. Merkel, Rev. Sci. Instrum. **78**, 034301 (2007).

17. Y. Iwadate and S. Yumura, BioTechniques **44**, 739 (2008).

18. F. Schneider, T. Fellner, J. Wilde, and U. Wallrabe, J. Micromech. Microeng. **18**, 065008 (2008).

19. E.K. Dimitriadis, F. Horkay, J. Maresca, B. Kachar, and R.S. Chadwick, Biophys. J. **82**, 2798 (2002).

20. A. Bot, I.A. van Amerongen, R.D. Groot, N.L. Hoekstra, and W.G.M. Agterof, Polymer Gels and Networks **4**, 189 (1996).

21. C.A. Reinhart-King, M. Dembo, and D.A. Hammer, Langmuir **19**, 1573 (2003).

22. J.G. Jacot, S. Dianis, J. Schnall, and J.Y. Wong, J. Biomed. Mater. Res. **A 79**, 485 (2006).

23. M.T. Frey, A. Engler, D.E. Discher, J. Lee, and Y. Wang, in Cell Mechanics (Elsevier, 2007), pp. 47–65.

24. E. Gutierrez and A. Groisman, PLoS One **6**, e25534 (2011).

25. T. Boudou, J. Ohayon, Y. Arntz, G. Finet, C. Picart, and P. Tracqui, J. Biomech. **39**, 1677 (2006).

26. T. Boudou, J. Ohayon, C. Picart, and P. Tracqui, Biorheology (2006).

27. A.P. Gunning, A.R. Kirby, M.J. Ridout, G.J. Brownsey, and V.J. Morris, Macromolecules **29**, 6791 (1996).

28. J. Domke and M. Radmacher, Langmuir **14**, 3320 (1998).

29. A.K. Denisin and B.L. Pruitt, ACS Appl. Mater. Interfaces **8**, 21893 (2016).

30. R.E. Mahaffy, C.K. Shih, F.C. MacKintosh, and J. Käs, Phys. Rev. Lett. **85**, 880 (2000).

31. D. Lee and S. Ryu, J Biomech Eng **139**, (2017).

32. V.I. Uricanu, M.H.G. Duits, R.M.F. Nelissen, M.L. Bennink, and J. Mellema, Langmuir **19**, 8182 (2003).

33. J.R. Tse and A.J. Engler, Curr. Protoc. Cell Biol. Chapter **10**, Unit 10.16 (2010).

34. S.R. Peyton and A.J. Putnam, J. Cell Physiol. **204**, 198 (2005).

35. M.Y. Kizilay and O. Okay, Macromolecules **36**, 6856 (2003).

36. A. Schellenberg, S. Joussen, K. Moser, N. Hampe, N. Hersch, H. Hemeda, J. Schnitker, B. Denecke, Q. Lin, N. Pallua, M. Zenke, R. Merkel, B. Hoffmann, and W. Wagner, Biomaterials **35**, 6351 (2014).

Chapter 4.1

1. A.J. Engler, S. Sen, H.L. Sweeney, and D.E. Discher, Cell **126**, 677 (2006).

2. D.A. Young, Y.S. Choi, A.J. Engler, and K.L. Christman, Biomaterials **34**, 8581 (2013).

3. J.H. Wen, L.G. Vincent, A. Fuhrmann, Y.S. Choi, K.C. Hribar, H. Taylor-Weiner, S. Chen, and A.J. Engler, Nat. Mater. **13**, 979 (2014).

4. B. Trappmann, J.E. Gautrot, J.T. Connelly, D.G.T. Strange, Y. Li, M.L. Oyen, M.A. Cohen Stuart, H. Boehm, B. Li, V. Vogel, J.P. Spatz, F.M. Watt, and W.T.S. Huck, Nat. Mater. **11**, 642 (2012).

5. J. Ou, C.L. Ren, and J. Pawliszyn, Anal. Chim. Acta **662**, 200 (2010).

6. J. Fu, Y.-K. Wang, M.T. Yang, R.A. Desai, X. Yu, Z. Liu, and C.S. Chen, Nat. Methods **7**, 733 (2010).

7. Y. Sun, L.G. Villa-Diaz, R.H.W. Lam, W. Chen, P.H. Krebsbach, and J. Fu, PLoS ONE **7**, e37178 (2012).

8. A. Schellenberg, S. Joussen, K. Moser, N. Hampe, N. Hersch, H. Hemeda, J. Schnitker, B. Denecke, Q. Lin, N. Pallua, M. Zenke, R. Merkel, B. Hoffmann, and W. Wagner, Biomaterials **35**, 6351 (2014).

9. E. Gutierrez and A. Groisman, PLoS ONE **6**, e25534 (2011).

10. E.A. Klein, L. Yin, D. Kothapalli, P. Castagnino, F.J. Byfield, T. Xu, I. Levental, E. Hawthorne, P.A. Janmey, and R.K. Assoian, Curr. Biol. **19**, 1511 (2009).

11. S.V. Plotnikov, A.M. Pasapera, B. Sabass, and C.M. Waterman, Cell **151**, 1513 (2012).

12. K.C. Russell, D.G. Phinney, M.R. Lacey, B.L. Barrilleaux, K.E. Meyertholen, and K.C. O'Connor, Stem Cells **28**, 788 (2010).

Chapter 4.2

1. E. Gutierrez and A. Groisman, PLoS ONE **6**, e25534 (2011).

2. Ronan and Groisman, in preparation.

3. S.J. Han, Y. Oak, A. Groisman, and G. Danuser, Nat. Methods **12**, 653 (2015).

4. K.C. Russell, D.G. Phinney, M.R. Lacey, B.L. Barrilleaux, K.E. Meyertholen, and K.C. O'Connor, Stem Cells **28**, 788 (2010).

5. B. Trappmann, J.E. Gautrot, J.T. Connelly, D.G.T. Strange, Y. Li, M.L. Oyen, M.A. Cohen Stuart, H. Boehm, B. Li, V. Vogel, J.P. Spatz, F.M. Watt, and W.T.S. Huck, Nat. Mater. **11**, 642 (2012).

6. J.H. Wen, L.G. Vincent, A. Fuhrmann, Y.S. Choi, K.C. Hribar, H. Taylor-Weiner, S. Chen, and A.J. Engler, Nat. Mater. **13**, 979 (2014).

7. C.M. Cesa, N. Kirchgessner, D. Mayer, U.S. Schwarz, B. Hoffmann, and R. Merkel, Rev. Sci. Instrum. **78**, 034301 (2007).

8. A.K. Harris, P. Wild, and D. Stopak, Science **208**, 177 (1980).

9. E. Gutierrez, E. Tkachenko, A. Besser, P. Sundd, K. Ley, G. Danuser, M.H. Ginsberg, and A. Groisman, PLoS ONE **6**, e23807 (2011).

10. M. Prager-Khoutorsky, A. Lichtenstein, R. Krishnan, K. Rajendran, A. Mayo, Z. Kam, B. Geiger, and A.D. Bershadsky, Nat. Cell Biol. **13**, 1457 (2011).

11. N.Q. Balaban, U.S. Schwarz, D. Riveline, P. Goichberg, G. Tzur, I. Sabanay, D. Mahalu, S. Safran, A. Bershadsky, L. Addadi, and B. Geiger, Nat. Cell Biol. **3**, 466 (2001).

12. A. Schellenberg, S. Joussen, K. Moser, N. Hampe, N. Hersch, H. Hemeda, J. Schnitker, B. Denecke, Q. Lin, N. Pallua, M. Zenke, R. Merkel, B. Hoffmann, and W. Wagner, Biomaterials **35**, 6351 (2014).

13. D.A. Young, Y.S. Choi, A.J. Engler, and K.L. Christman, Biomaterials **34**, 8581 (2013).

14. A.J. Engler, S. Sen, H.L. Sweeney, and D.E. Discher, Cell **126**, 677 (2006).

15. J. Fu, Y.-K. Wang, M.T. Yang, R.A. Desai, X. Yu, Z. Liu, and C.S. Chen, Nat. Methods **7**, 733 (2010).

16. S. Kuddannaya, Y.J. Chuah, M.H.A. Lee, N.V. Menon, Y. Kang, and Y. Zhang, ACS Appl. Mater. Interfaces **5**, 9777 (2013).

Chapter 5

1. A.W. Hirshfeld, The Electric Life of Michael Faraday (Walker Books, London, 2006).
2. H.V. Brøndsted, Biol. Rev. **30**, 65 (1955).
3. I. Hori and Y. Kishida, Hydrobiologia **383**, 131 (1998).
4. M. Morita and J.B. Best, J. Exp. Zool. **231**, 273 (1984).
5. T.R. Paskin, J. Jellies, J. Bacher, and W.S. Beane, PLoS ONE **9**, e114708 (2014).
6. K. Azuma, and T. Shinozawa, J. Exp. Biol. **201**, 1263 (1998).
7. J.A. Carter, C.H. Lind, M.P. Truong, and E.-M.S. Collins, J. Stat. Phys. **161**, 250 (2015).
8. M.R. Nentwig, Trans. Am. Microsc. Soc. **97**, 297 (1978).
9. I. Hori, and Y. Kishida, Belg. J. Zool. **131**, 117 (2001).
10. A. Vandel, Recherches expérimentales sur les modes de reproduction des planaires triclades paludicoles (Edition du Bulletin biologique de la France et de la Belgique, Paris, 1922)
11. J. Dunkel, J. Talbot, and E.-M. Schötz, Phys. Biol. **8**, 026003 (2011).
12. S. Quinodoz, M.A. Thomas, J. Dunkel, and E.-M. Schötz, J. Stat. Phys. **142**, 1324 (2011).
13. M.A. Thomas, S. Quinodoz, and E.-M. Schötz, J. Stat. Phys. **148**, 664 (2012).
14. F. Cebrià, Front. Cell Dev. Biol. **4**, 8 (2016).
15. W.M. Kier, J. Exp. Biol. **215**, 1247 (2012).
16. O. Cochet-Escartin, K.J. Mickolajczyk, and E.-M.S. Collins, Phys. Biol. **12**, 056010 (2015).
17. D.W. Thompson, On Growth and Form: The Complete Revised Edition (Dover Publications, Mineola, 1992).
18. X. Yang, K.J. Kaj, D.J. Schwab, and E.-M.S. Collins, Phys. Biol. **14**, 036003 (2017).
19. H. Orii, H. Ito, and K. Watanabe, Zool. Sci. **19**, 1123 (2002).
20. C.M. Child, Biological Bulletin **11**, 113 (1906).
21. R.W. Mead, J. Exp. Zool. **235**, 45 (1985).

22. I.M. Sheiman, Z.V. Sedel'nikov, M.F. Shkutin, and N.D. Kreschenko, Ontogenez **37**, 130 (2006).

23. A.M. Glazer, A.W. Wilkinson, C.B. Backer, S.W. Lapan, J.H. Gutzman, I.M. Cheeseman, and P.W. Reddien, Dev. Biol. **337**, 148 (2010).

24. R.W. Style, R. Boltyanskiy, G.K. German, C. Hyland, C.W. MacMinn, A.F. Mertz, L.A. Wilen, Y. Xu, and E.R. Dufresne, Soft Matter **10**, 4047 (2014).

25. M.K. Kwan, E.J. Wall, J. Massie, and S.R. Garfin, Acta Orthop. Scand. **63**, 267 (1992).

26. L.D. Muiznieks and F.W. Keeley, Biochim. Biophys. Acta **1832**, 866 (2013).

27. C.M. Child, J. Exp. Zool. **11**, 187 (1911).

28. E.B. Krichinskaya, Hydrobiologia **132**, 195 (1986).

29. M.E. Isolani, J.F. Abril, E. Saló, P. Deri, A.M. Bianucci, and R. Batistoni, PLoS ONE **8**, e55649 (2013).

30. T. Sawada, K. Oofusa, and K. Yoshizato, Wound Repair Regen. **7**, 458 (1999).

31. K.S. Topp and B.S. Boyd, Phys. Ther. **86**, 92 (2006).

32. J.P. Dexter, M.B. Tamme, C.H. Lind, and E.-M.S. Collins, Sci. Rep. **4**, 6388 (2014).

33. M. Backholm, W.S. Ryu, and K. Dalnoki-Veress, Proc Natl Acad Sci USA **110**, 4528 (2013).

34. J.B. Best, M. Abelein, E. Kreutzer, and A. Pigon, J. Comp. Physiol. Psychol. **89**, 923 (1975).

35. M.A. Thomas and E.-M. Schötz, J. Exp. Biol. **214**, 3518 (2011).

36. D. Hagstrom, O. Cochet-Escartin, S. Zhang, C. Khuu, and E.-M.S. Collins, Toxicol. Sci. **147**, 270 (2015).

37. R.S. King and P.A. Newmark, BMC Dev. Biol. **13**, 8 (2013).

38. E. Gutierrez and A. Groisman, PLoS ONE **6**, e25534 (2011).

39. K.G. Ross, K.C. Omuro, M.R. Taylor, R.K. Munday, A. Hubert, R.S. King, and R.M. Zayas, BMC Dev. Biol. **15**, 2 (2015).

40. R.J.A. Wilson, B.A. Skierczynski, J.K. Meyer, R. Skalak, and W.B. Kristan, J. Comp. Physiol. A **178**, (1996).

41. M.C. Junger and D. Feit, Sound, Structures, and Their Interaction (MIT Press, Cambridge, 1986).

42. W. Gilpin, S. Uppaluri, and C.P. Brangwynne, Biophys. J. **108**, 1887 (2015).